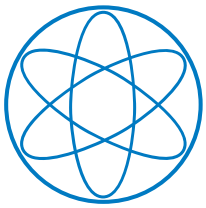

PHYSIK DEPARTMENT

SINGLE MOLECULE SPECTROSCOPY

ON HSP90

Christoph Ratzke

TECHNISCHE UNIVERSITÄT MÜNCHEN

Technische Universität München
E22a Biophysik

Single Molecule Spectroscopy on Hsp90

Christoph Ratzke

Vollständiger Abdruck der von der Fakultät für Physik der Technischen Universität München zur Erlangung des akademischen Grades eines

Doktors der Naturwissenschaften (Dr. rer. nat.)

genehmigten Dissertation.

Vorsitzender: Univ.-Prof. Dr. Martin Zacharias

Prüfer der Dissertation:

1. Univ.-Prof. Dr. Thorsten Hugel
2. Univ.-Prof. Dr. Matthias Rief

Die Dissertation wurde am 16.01.2013 bei der Technischen Universität München eingereicht und durch die Fakultät für Physik am 28.02.2013 angenommen.

Contents

Abstract

Hsp90 is a molecular chaperone which can be found in most organisms with high cellular concentrations. It is a dimer, consisting of two elongated monomers lying in parallel to each other. They contact each other via a N- and a C-terminal dimerization site. At the N-terminal end ATP can be bound and hydrolyzed with a very low ATPase rate, which is nevertheless essential for its function. Hsp90 was known to undergo large conformational changes and it was supposed that while the C-terminal dimerization site is permanently closed the N-terminal site closes upon ATP binding and reopens after its hydrolysis. Moreover small proteins - so called cochaperones - are known to bind to Hsp90 and modulate its function. To resolve the conformational dynamics and especially the mechanochemical cycle of Hsp90 from yeast and bacteria single molecule two, three and four color FRET were used in this work, which allowed to follow the conformational changes and the ATP turnover of Hsp90 in real time on single molecule level. Surprisingly and contrary to existing models Hsp90 shows rich conformational dynamics, also in the absence of ATP at both dimerization sites. Moreover it turned out that binding of nucleotides on the N-terminus influences the C-terminal dynamics; binding of ATP and even more ADP leads to a C-terminal opening. Furthermore the N-and C-terminal dynamics are anticorrelated. Three color single molecule FRET showed that surprisingly ATP can be bound in the open and closed state of Hsp90. The ATP binding and release rates are much faster than ATP hydrolysis. Thus Hsp90 shows N- and C-terminal dynamics and ATP binding with no preference to a certain state. Hsp90 thus does not have a successive conformational cycle, but it is thermally driven through a network of states. ATP hydrolysis is the only irreversible process that drives the reaction cycle slowly forward. Moreover the cochaperone Sba1 could be shown to shift this conformational network towards the ATP bound closed state. Surprisingly the bacterial Hsp90 (Htpg) has a strikingly different mechano-chemical cycle. For HtpG binding of ATP leads to closed stated via a mechanical ratchet mechanism. In contrast the C-terminal dimerization site is mostly closed. Thus the Hsp90 ma-

chinery developed from a nucleotide controlled mechanical ratchet mechanism to a mainly randomly fluctuating system. Due to those findings the picture of Hsp90 has to be massively revised. Moreover the resolved mechanochemical cycles of yHsp90 and HtpG will be the fundament for all further investigations of Hsp90 mechanistics and function.

Part I.

Introduction

1. Struggles in the life of a cell

Proteins are essential tools in the living cell. They convert energy, catalyse anabolic and catabolic reactions, transport cargo and regulate the cell and its metabolisms. Thus correct protein folding and function are crucial for the survival of the cell and the whole organism. Unfortunately organisms are exposed to a wide range of environmental stress like oxygen depletion, mechanical stress, toxic stress and especially heat, leading to unfolding, misfolding and aggregation of proteins. To protect the cell from those harmful or even lethal consequences of stress, a group of proteins is produced upon stress which keeps up the cell integrity. Proteins which are up-regulated during heat stress are called heat shock proteins [1]. Most of those heat shock proteins belong to the protein family of chaperones [2]. These proteins have the ability to temporarily interact with other mis- or unfolded proteins and stabilize them, stop their aggregation or support their refolding. Thus they protect the cell from heat death and keep the organism alive under heat shock. One of those chaperones is the heat shock protein 90 (Hsp90), which is investigated in this work.

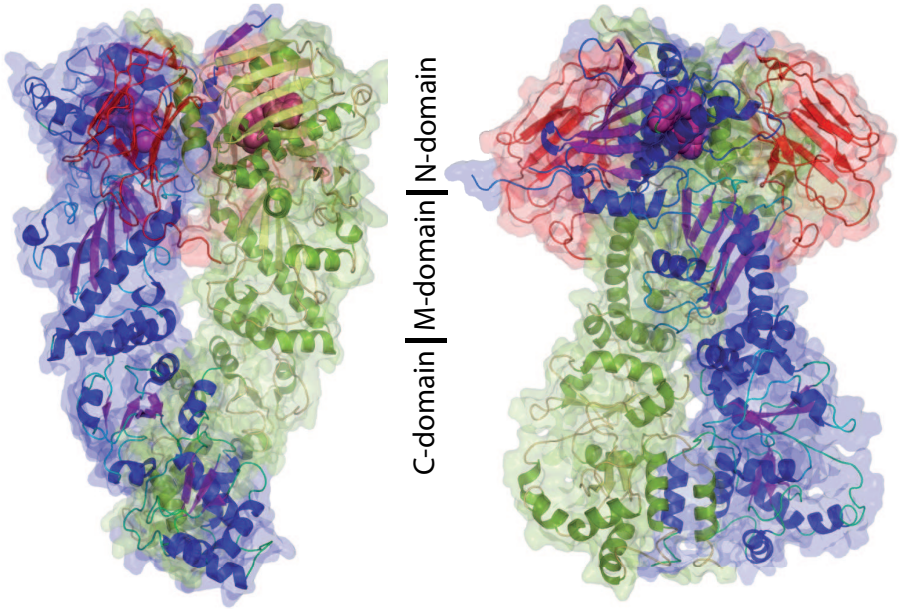

Figure 1.1.: Structure of Hsp90. The crystal structure of yHsp90 in complex with Sba1 and AMP-PNP (PDB entry: 2CGE, [3]) shown at 0° and 90° rotation. The two monomers are shown in blue and green. The two bound Sba1 are shown as red cartoon, the two bound AMP-PNPs are shown as violet spheres. PDB entry is 2CG9.

2. Hsp90

Contrary to other heat shock proteins Hsp90 is a very common protein in the cell also under physiological conditions (1-2 % of total cell mass) [4, 5] . Anyway under heat stress there is a massively increased expression. Hsp90 can be found in eukaryotic and prokayotic cells. Different cellular compartments have different subtypes, like Grp94 in the endoplasmatic reticulum [6] or TRAP1-in the mitochondrium [7]. Although this big variety exists, there is a pronounced homology between the different subtypes. In this work I will focus on the eukariotic yeast Hsp90 (yHsp90) and the bacterial Hsp90 (HtpG) from *Escherichia coli*.

2.1. The structure and mechanistics of Hsp90

Hsp90 is a dimer and consists of two elongated chain-like monomers which lie in parallel [3, 8]. The dimer is quite stable with a dissociation constant in the nanomolar region [9, 10, 11, 12, 13]. Each monomer consists of three domains, the N- , middle- and C-domain. The N-domain can bind and hydrolyze ATP, although with a very slow ATPase rate of around one ATP per 1-2min [14, 10]. The middle domain is supposed to interact with substrates [15, 16], whereas the C-terminal domain contains the dimerization site [8, 10, 17]. The ATP turnover plays an essential role in the function of the protein [18]. Thus a knock-out of the ATPase function is lethal at least for eukaryotes under heat stress [19, 20]. ATP is bound in the N-terminal domain with a weak affinity in the µM range [14, 21]. Moreover it is bound in a very special kinked way, which is typical for the small family of GHKL ATPases, which Hsp90 belongs to [3, 21, 22, 23, 24]. The adenine and the ribose of the ATP are buried inside the protein, whereas the phosphate groups point outwards. Anyway this special way of ATP binding makes it possible to develope very specific ATPase inhibitors for Hsp90 [25]. To hydrolyze the ATP Hsp90 has to be cross-activated by the other monomer by going into a N-terminally closed state [14], beside that also

interactions with the middle domain seem to be necessary for the cleavage of ATP [21, 12]. It could be shown that Hsp90 exists in a N-terminal V-like open and closed state [26, 27]. Since N-terminal closing is necessary for the ATP cleavage [14], the general picture up to now was, that ATP turnover drives the N-terminal opening and closing of Hsp90 (Fig. 2.1) [28, 26]. In this model the binding of ATP leads to N-terminal dimerization; contacts between the N- and middle domain lead to an even more compact dimer and ATP hydrolysis. After cleavage of the ATP the Hsp90 dimer re-opens. This model was supported by the 2006 obtained crystal structure of yHsp90 in the presence of the ATP analog AMP-PNP and the cochaperone Sba1 showing a closed structure of Hsp90 (Fig. 1.1) [3] . Anyway the conformational cycle was not directly observed and the role of the ATPase function remained enigmatic. Resolving the mechanochemial cycle of Hsp90 was one of the main goals of this work.

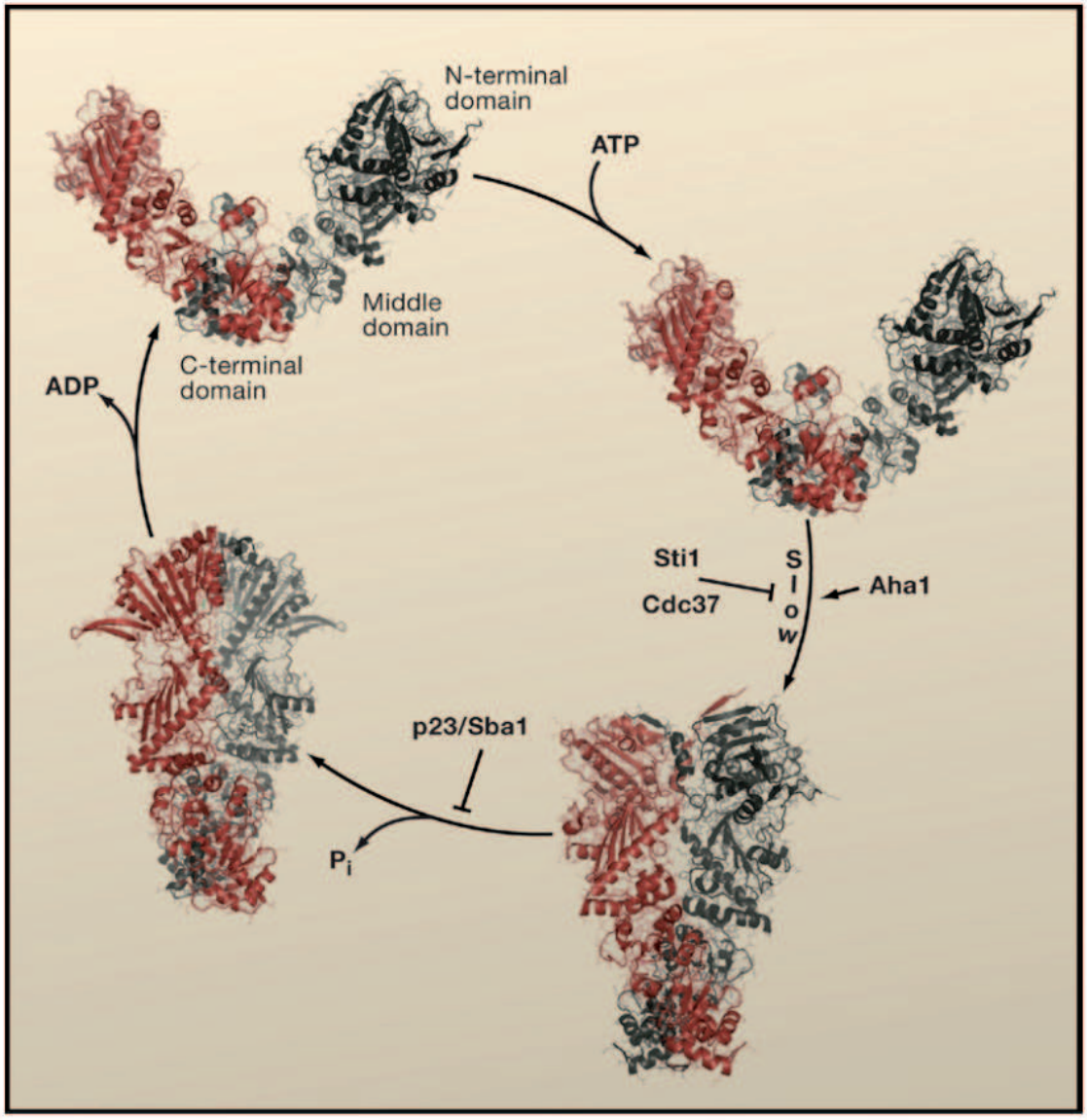

Figure 2.1.: Supposed Hsp90 cycle. This cycle or similar ideas can be found in a lot of puplications. Anyway this cycle was never directly measured. Figure taken from [29]

2.2. Hsp90 is influenced by posttranslational modifications and cochaperons

The function of Hsp90 is modified by a lot of factors. Thus it can be modified by posttranslational modifications like phosphorylation [30, 31], acetylation [32, 33] and

nitrosylation [34, 35]. Moreover in the cell Hsp90 does not work as isolated protein, but in cooperation with a number of small proteins, that can bind to multiple binding sites of Hsp90 [16]. Those so called cochaperones are able to modify the structure and function of Hsp90. Some examples are the cochaperone Sba1 [36], which is known to slow down the ATPase rate and enhances substrate release [37], Sti1, that connects Hsp90 and Hsp70 [38, 39] and Aha1 that massively accelerates the ATPase turnover [40] .The exact role and also the mechanistic of those cochaperones are only weakly understood. In this work also the influence of cochaperones on the function of Hsp90 has been investigated.

2.3. Hsp90 has multiple functions in the cell

Even though there is only little known about the mechanistics of Hsp90, its function - the chaperoning of substrates - is even less understood. The natural function of chaperones is to bind denatured and misfolded proteins to prevent them from aggregation and to support their refolding. Since this is normally a rather unspecific process, it is represented by a weak binding affinity. In contrast Hsp90 is known to bind rather strong to some proteins, which allowed the identification of a number of substrates [41]. Those substrates are often proteins involved in cell cycle regulation, cell proliferation and signal transduction (an actual list of substrates can be found at http://www.picard.ch/downloads/Hsp90interactors.pdf). Some substrates are known to bind in a native conformation under physiological conditions, which makes Hsp90 directly affect gene activation and signal transduction in the cell [42]. Since cell regulation shows massive malfunction in cancer cells Hsp90 became an interesting cancer drug target [43, 44, 25]. Thus Hsp90 obviously has a twofold chaperone function: Protecting proteins from denaturation and aggregation during heat shock, but also affecting proteins under physiological conditions.

3. How can the complex dynamics of Hsp90 be revealed?

Investigating enzymatic reactions with bulk methods has a long tradition and led to many insights into the dynamics of proteins. Although the observed physical parameter like UV/Vis or IR absorption, fluorescence or circular dichroism may vary the principle remains the same. A sample of protein is prepared in a cuvette where the added protein stays in a macroscopic equilibrium. The equilibrium is than disturbed mostly by addition of nucleotides or other binding partner less often by temperature or pressure changes and the relaxation into equilibrium is observed. With the help of stopped and continuous flow devices mixing the different compounds can be done very quickly (millisecond range) and thus a very high time resolution can be obtained. Anyway all these techniques have a common problem which hinders revealing detailed mechanistic information. They just lead to average values: Average concerning the underlying states as well as the kinetics. This is already true for rather simple systems (Fig. 3.1), but even more, when there is no additional information about the underlying mechanism and the system is complex, which is for biological systems in general the case. Another problem of bulk measurements is that it is not in general possible to derive causalities of coupled processes with bulk measurements. For example both a binding partner that induces a conformational change (power stroke) or a binding partner that stabilizes a specific state which is reached by thermal fluctuations (mechanical ratchet), will cause the same result in a bulk measurement. But knowledge of those causalities is exactly what is necessary to reconstruct the mechanistics of enzymes. Observing the kinetics of single molecules instead of an ensemble of molecules overcomes exactly those problems. One of the most powerful single molecule techniques is the single molecule Förster resonance energy transfer (FRET) microscopy [45]. It allows to directly follow the movement of single molecules in real time even under macroscopic equilibrium conditions and thus real rates for the observed transitions can be obtained and even complex kinetic

systems can be uncovered. Moreover single molecule multicolor FRET allows the observation of several processes at the same time and especially its causal relation. Therefore single molecule FRET offers an unique chance to reveal such complex mechanistics as expected for Hsp90.

In this work single molecule two, three and four color FRET was used to investigate the conformational dynamics and the mechanistics of Hsp90. Furthermore the interaction of Hsp90 with nucleotides and cochaperones was investigated. Moreover multicolor FRET made it possible to directly observe the coupling between different molecular processes and its causal order. Since this is not possible with any other technique new insights into the the dynamics of Hsp90 and protein function in general could be obtained, which leads to a massive revision of the picture of Hsp90.

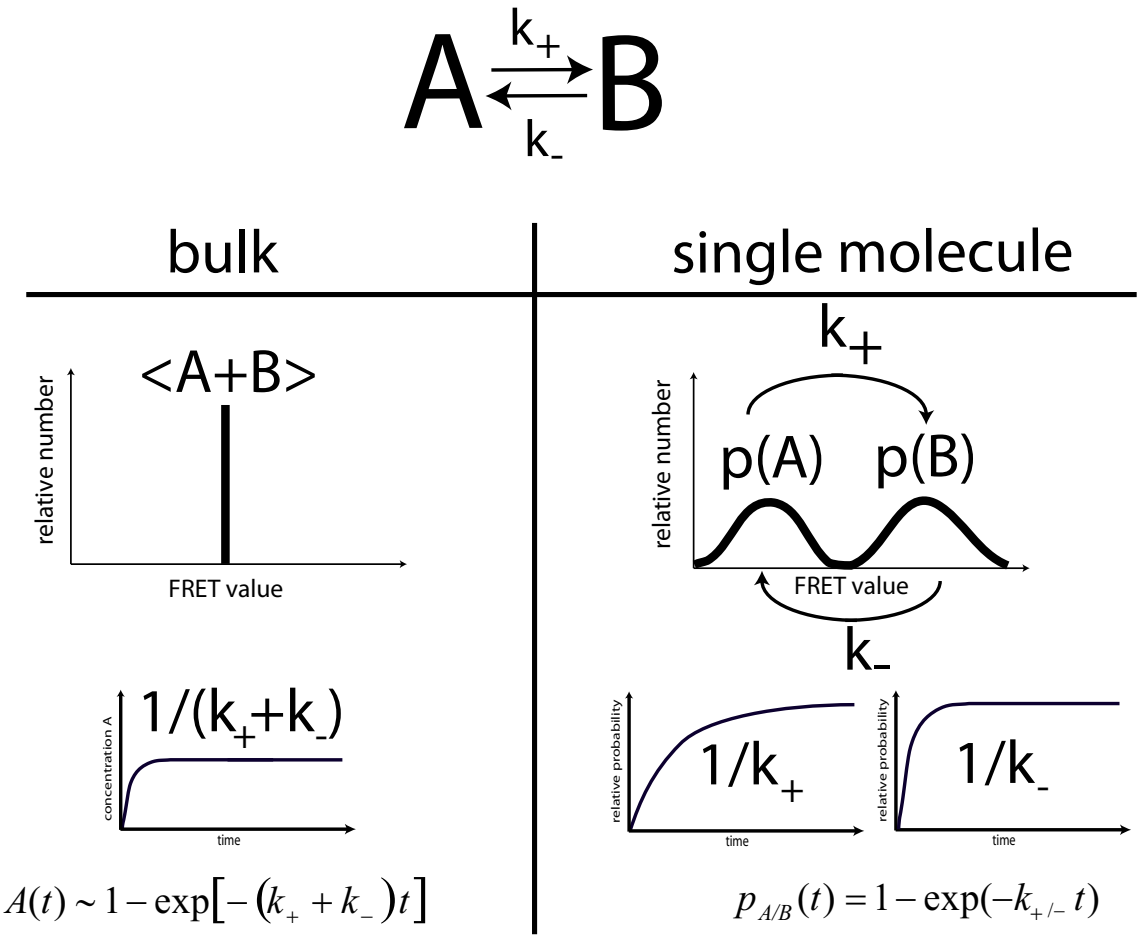

Figure 3.1.: Comparison of bulk and single molecule FRET measurements. For a simple two state model a bulk measurement will result in only one FRET value, which is equal to the average value of the two species' FRET signals. Thus the bulk measurement results in a FRET value of one non-existing state. In single molecule measurements a distribution of the FRET values will be obtained and the two states can be separated. Kinetic measurements in bulk are usually done by disturbing the equilibrium (e.g. adding of a binding partner); afterward the relaxation into the equilibrium is observed and the obtained kinetic fitted with exponential equations leading to "rate constants". Anyway already for the here shown very simple example a mixture of rates will be obtained in a bulk experiment - as can be found in every physical chemistry textbook [46]. Thus in the end bulk measurements can in general give no explicit answer about reaction kinetics. This is already true for the here shown very simple system, but usually biological systems are way more complex.

Part II.

Material and Methods

4. Molecular Biology, Protein Expression and Purification

4.1. Molecular biology

To keep the Hsp90 monomers in close proximity during the single-molecule experiments, I inserted a coiled-coil motif of the kinesin neck region of *Drosophila melanogaster* (DmKHC, [47]) to the C-terminus of yHsp90, for HtpG this was done by the group of Matthias Mayer, EMBL, Heidelberg. The coiled coil prevents the Hsp90 dimer from dissociation even at the very low concentrations. This construct shows the same ATPase activity, Sba1 binding, and N-terminal kinetics as the wild type [48]. In addition, such fused yHsp90 are viable in yeast [49, 50]. A similar construct with a N-terminal coiled coil was obtained from the lab of Dan Bolon, University of Massachusetts Medical School, Worcester, but this construct shows a significantly higher ATPase rate (Fig. A.1). Thus the measurements of the C-terminal dynamics were done without coiled-coil, but in vesicles instead (described below sec. 7.2.2)

Cysteine point mutations were created with the QuickChange Multi Site-Directed Mutagenesis Kit (Agilent Technologies) or Finnzymes Site directed mutagenesis kit (Finnzymes) respectively. Both were used as described by the supplier.

A summary of the in this work used mutants is given in Tab. 4.1.

Protein	Mutation
yHsp90	61 Cys , C-term coiled coil
	385 Cys, C-term coiled coil
	560 Cys
	Δ8, 560 Cys
	Δ24, 560 Cys
	N-term coiled coil, 560 Cys
HtpG	61 Cys, C-term coiled coil
	341 Cys, C-term coiled coil
	61 Cys, 341 Cys, C-term coiled coil
	521 Cys
Sba1	66 TAG

Table 4.1.: List of mutants used in this work.TAG is the amber stop codon and is used for insertion of artificial amino acids.Δ means N-terminal deletion. See sec. 5.2 for details.

4.2. Protein expression and purification

4.2.1. Expression of yHsp90 and HtpG

yHsp90 and HtpG mutants were all expressed either in BL21 codon + or BL21Star cells (both Life Technologies) in LB_0 medium or TB medium. All yHsp90 mutants were cloned into a pET28 vector with T7 expression system . The HtpG was cloned into a pBAD vector with an araBAD promotor. The bacterial cultures were grown to an OD_{600} of 0.5 in LB_0 or to OD_{600} of 2 in TB. The induction was done either with 1mM IPTG (T7 system) or 0.01% L-Arabinose (araBAD system). The expression was performed either at 37°C over 3-5h or over night at 30°C. The expression of the unnatural amino acid containing proteins is described below (sec. 4.2.2.1).

4.2.2. Expression of Hsp90 and cochaperone mutants containing unnatural amino acids (UAA)

Details about the incorporation of unnatural aminoacids are given below (sec. 5.2).

4.2.2.1. Expression of p23 66pAcF

To allow HisTag purification without having the HisTag on the final protein product, a construct was synthesized with Sba1 having a HisTag at the N-terminal end whereas between the Sba1 and the HisTag is a SUMO sequence which can be specifically cut off by the protease Senp. Since the Senp cuts directly at the end of the SUMO sequence no additional amino acids are left and Sba1 is obtained, that has exactly the same sequence as the wild type form. The Sba1 gene was cloned into a pET28 vector and a TAG amber stop codon was introduced by site directed mutagenesis as described above. The Sba1/pet28 vector was co-transformed with the pAcF pEVOL vector, which contains the artificial tRNA and the artificial aminacyl-tRNA-syntethase (aaRS) under araBAD promotor control. Thus the Sba1 and the aaRS expression can be induced independently. As expression cells BL21 Star was used. For the expression cells were grown to a OD of 3 at 37°C with high shaking speed (250 rpm, 2inch shaking orbit or 310 rpm, 1inch shaking orbit). Then they were cooled down to 30°C and after 1 h 10mM pAcF and 0.02% arabinose were added. After one additional hour 1mM IPTG was added to start Sba1 expression. The cells were incubated at least 18h .

4.2.3. Purification of yHsp90 and Sba1

The obtained cells were lysed by sonification (Branson W-250D, Emerson Industrial Automation) or a cell disruptor (40kpsi TS-series, Constant Systems Ltd.) in soni buffer (50mM sodiumphosphate, 200mM NaCl, pH 7.8) with 20mM imidazol. The cell lysate was centrifuged with 39800xg (Avanti J-E, Beckmann Coulter with a JA-17 rotor). The supernatant was applied to a NiNTA column (HisPrep FF 16/10, GE Lifesciences). The bound protein was eluted with soni buffer containing 500mM imidazol. The elution was dialyzed against buffer A (40mM hepes, 50mM NaCl, pH 7.5) and applied to a SepharoseQ HP (GE Lifesciences) column. After protein binding the protein was eluted with a gradient up to 70% buffer B (80mM hepes, 1M NaCl, pH 7.5). The protein containing fractions were pooled and applied to a Superdex 200 HiLoad 16/600 column.

4.2.4. Purification of HtpG

The HtpG constructs with the N- and M-domain cysteine mutations and a C-terminal coiled coil structure contained no HisTag, but a StrepTagII C-terminal of the coiled coil instead. Thus a StrepTag (IBA) column was used for the first purification step. In contrast the HtpG constructs with a cysteine at position 521 contained no coiled coil but a N-terminal HisTag. These constructs were purified as described for yHsp90 (sec. 4.2.3)

5. Protein labeling

5.1. Labeling of cysteines

yHsp90 and HtpG both do not contain natural cysteines thus introducing cysteines via site directed mutagenesis and labeling via maleimide chemistry allows specific covalent attachment of dyes. For the labeling process the protein was used at a concentration of around 50µM and 5-10mM tris(2-carboxyethyl)phosphine (TCEP) were added. After incubation for 1h at RT the TCEP was removed and buffer exchanged by washing the protein in a Viva Spin 500 concentrator (GE Lifesciences) with PBS, pH 6.7. The slightly lowered pH avoids unwanted reaction of the maleimide with amino groups. The protein was washed at least 3 times by removing >90% of the buffer volume by centrifugation at 10000rpm at a 5424 centrifuge with F-45-18-11 rotor (Eppendorf) and refilling it with PBS buffer. The remaining protein was concentrated to around 50µM and dye was added with 3-fold excess. After 2h of incubation at RT the non-bound dye was removed either by gel filtration with two gel spin columns (Illustra MicroSpin G-50, GE Lifesciences) according to suppliers protocol or by dialysis against 10mM hepes, 10mM KCl, pH 7.5 for two days (ZelluTrans/Roth Mini-Dialyzer MWCO 12000, Roth). The dialysis has the advantage that virtually no protein is lost. After the labeling homodimers were obtained with a degree of labeling of around 75-100%. To form heterodimer monomer exchange was done as described below (sec. 5.3). Since the HtpG mutants were pretty sensitive to aggregation, the two FRET dyes were added simultaneously both with 1.5-fold excess. The labeling process itself is probabilistic thus about 50% are heterodimers whereas the other 50% are homodimers. Anyway homodimers do not show a FRET signal and do not disturb the measurement.

5.2. Labeling of artificial amino acids

Contrary to yHsp90 and HtpG cochaperones have natural cysteines, which makes a labeling with maleimide chemistry impossible - at least without removing the natural cysteines. Furthermore with cysteine maleimide chemistry only one dye can be attached to one protein chain in a specific way. To overcome this limitations I used here the possibility to introduce unnatural amino acids (UAA) into proteins [51, 52, 53]. The unnatural amino acid bears a certain reactive group which allows specific labeling. In general those systems work as follows: For protein synthesis *in vivo* mRNA is produced from DNA and bound by the ribosome where tRNA bearing an amino acid temporarly binds the complementary region of the DNA. The amino acids are connected to form a polypeptide chain. Thus for the introduction of an unnatural amino acid a new tRNA is necessary that binds to a codon which is not coding a natural amino acid (TAG in this case) and the new tRNA must also not bind to natural codons (orthogonal tRNA). Furthermore the enzyme loading the amino acid to the tRNA (aminoacyl-tRNA-synthetase) must specifically load the artificial amino acid to the artificial tRNA without any cross reaction with natural tRNA or natural amino acids. Such a system was developed by the Schultz lab in the past and has already been used for protein labeling, although for small and good soluble proteins [54, 55, 56]. Indeed it turned out that these systems are pretty difficult to handle, especially for large proteins like Hsp90. Expression for Sba1 is described in sec. 4.2.2.1.

In this work an UAA system was used that allows incorporation of para- acetylphenylalanine (pAcF) (Fig. 5.1). Unfortunately optimal labeling conditions are very harmful for our proteins (low pH, high temperatures, high concentrations)[54, 55]. Therefore the labeling was done under moderate conditions resulting in a lowered degree of labeling (DOL).

5.2.1. Labeling of Sba1 66pAcF

The labeling of the inserted keto group was done with hydroxylamine derivated dyes [55]. Doing this there are two major problems. First the labeling conditions are potentially harmful for the protein and have to be optimized for every protein. Thus the protocol presented here is only valid for Sba1. Second the hydroxylamine is

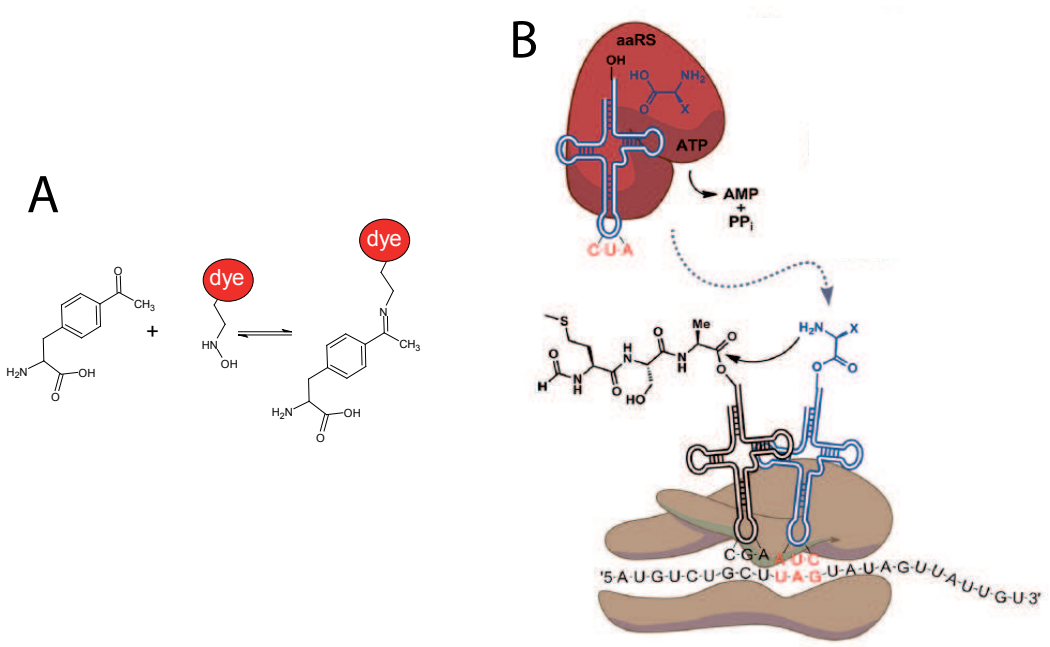

Figure 5.1.: (A) Hydroxylamine dyes react with p-acetylphenylalanine. (B) An artificial aminoacyl-tRNA-synthetase (red) loads the unnatural amino acid (blue with sidechain x) onto the orthogonal tRNA. This tRNA binds to the amber stop codon UAG and the unatural amino acid is incorporated into the polypeptide chain. (B) taken from [53]

unstable towards impurities or even oxygen, thus the whole labeling process should be carried out in very pure solutions and under exclusion of oxygen as far as possible. The Sba1 was transferred to the labeling buffer 50mM potassium acetate, 150mM KCl, pH 6 with a concentration of more than 200µM by washing it three times in a 10000MWCO vivaspin concentrator. The rotation velocity was only 10000rpm in the air cooled 5452 Eppendorf centrifuge to avoid heating the sample to much. Afterward TCEP was added with a final concentration of 2mM. A needle pointed through the cap and the protein solution taken to vacuum for 10min. During that time the dye was dissolved in degased water with a concentration of around 5-10mM. The dye stock solution was centrifuges at max speed for 2min; the supernatant was taken. 1mM dye and 10mM aniline were added to the protein solution and the volume adjusted to to have a protein concentration of around 200µM. The cup was put into a plastic bag filled with nitrogen. The sample was incubated 2d at 6°C. After that the sample was dialyzed against measurement buffer (40mM hepes, 150mM KCl, 10mM MgCl, pH 7.4) for 3 days. Anyway normally a pretty low DOL

of around 20% could be obtained.

5.3. Monomer exchange

To get heterodimers with two different labels and labeling positions the monomers were exchanged. For the proteins not bearing a terminal coiled coil that was easily done by mixing the monomers and incubating at 37°C for 15min . The exchange time at 30°C is around 850s for yHsp90 (Fig. 10.8) and 150s for HtpG (Fig. 12.4). Anyway for proteins bearing a zipper two homodimers were mixed at a concentration of 0,5µM each (monomer concentration) in measurement buffer and heated up to 47°C for 30min. In the case Atto488 was one of the used dyes 0,5mg/mL BSA had to be added since Atto488 is very sensitive to surface adhesion, which massively decreases the dyes photostability. After that time the sample was cooled down to RT for 15min and chilled on ice after that. The heterodimers were immediately aliquoted with 10µL each aliquot and shock-frozen in liquid nitrogen. For measurements an aliquot was thawed and used just once.

6. Bulk measurements

6.1. Measurement of the ATPase activity

To check whether the mutations are influencing the functionality of Hsp90 the ATPase activity was measured. The measurement was done via a NADH coupled enzymatic assay [18]. ADP produced during the ATP turnover of Hsp90 is rephosphorylated by pyruvatkinase (PK) with phosphoenolpyruvate (PEP). This reaction produces pyruvate which is reduced to lactate by lactatedehydrogenase (LDH) under the oxidation of NADH to NAD^+. Since NADH but not NAD^+ shows a strong absorbtion at 340nm the reaction can be followed in real time in an absorbtion spectrometer. For the measurement a fresh premix was mixed by adding 240µL PEP (100mM), 48µL NADH (50mM), 12µL PK(2000U/ml) and 44µL LDH (2750U/mL) to 8656 µL measurement buffer (all chemicals from Roche). For a measurement in a total volume of 80µL 60µL premix were used and ATP was added to a final concentration of 2mM. Hsp90 was added to a final concentration of 2µM, if not described otherwise. To check for background activity after the measurement 1µL of a 2mg/mL radicicol solution was added. Radicicol specifically inhibits the Hsp90 ATPase activity. All measurements were done in 40mM hepes, 150mM KCl, 10mM $MgCl_2$ pH 7.4 this buffer is called measurement buffer here.

6.2. Measurement of monomer exchange

The subunit exchange experiment was done in the measurement buffer (sec. 6.1) with Hsp90 560C or HtpG 521C, respectively. All measurements were done at 30 °C —just as the single-molecule measurements. First the Atto550-labeled homodimers were diluted to a concentration of 200nM for yHsp90 and 250nM for HtpG and incubated at 30 °C for about 15 min. Then the Atto647N labeled homodimers were

added also at a concentration of 200 nM. The fluorescence has been observed over time in a FP-6500 fluorometer (Jasco) exciting the Atto550 at 530 nm and detecting the Atto550 at 580 nm and the Atto647N at 675 nm. If measurements were done with nucleotides the nucleotides were added before the preincubation. To compare the measured data with the rates obtained from the single molecule experiments the monomer exchange process has been simulated based upon the rates obtained from the single molecule data. The simulation is described below (sec. 6.4.1).

6.3. Stopped flow measurements of ATP binding

The Hsp90 61C C-terminal coiled coil construct was labeled with Atto550, and the ATP was labeled with Atto 647N at the γ-phosphate (obtained from Atto Tec). The excitation was at 550nm, whereas the emission was detected from 625 to 775nm. Both binding partners were preincubated in the stopped-flow syringes to avoid temperature effects. Mixing of the two components, both with a concentration of 500nM, led to a FRET signal and therefore an increase of the acceptor emission intensity in time. The fluorescence vs. time signal is shown in Fig. 11.7. To compare the stopped-flow data with the rates obtained from the single-molecule measurements, a computer simulation of the stopped-flow process using the rates from the single-molecule measurements was done (sec. 6.4.2). The rates for opening and closing with and without ATP bound are taken from [48] and are around 1/5 s.

6.4. Simulation of protein kinetics

6.4.1. Simulation of monomer exchange

The process of subunit exchange has been simulated by iteratively solving the underlying differential equations for the rate constants and concentrations. The concentration of a state i at the time t+Δ t is given by

$$C_i\left(t+\Delta t\right) = C_i(t)+[k_{i-1,i}\cdot C_{i-1}(t) + k_{i+1,i}\cdot C_{i+1}(t) - k_{i,i+1}\cdot C_i(t) - k_{i,i-1}\cdot C_i(t)]\cdot\Delta t \tag{6.1}$$

where $k_{i,j}$ is the rate constant of the process depopulating state i and populating state j. The scheme depicted in Fig. C.6 describing the subunit exchange can therefore be represented by a set of coupled differential equations. We have seven states: homodimer with closed N-terminus or closed C-terminus or both, heterodimer with N-terminus closed or C-terminus closed or both, and finally a monomeric state. In an exchange experiment two species of homodimers are added and the formation of heterodimers is observed (sec. 5.3). Accordingly, we start the simulation with the four states without heterodimers: a monomeric, a N-terminal dimerized, a C-terminal dimerized, and a C- and N-terminal dimerized state. The equilibrium concentrations for these states are given by the N- and C-terminal dimerization kinetics. To calculate an upper limit for the exchange kinetics, we took the slowest rate constants measured for the N-terminus [48] and the C-terminus Fig. A.3 in the absence of nucleotide, namely, 1/10 s^{-1}. Finally, we assume that the probability to form a heterodimer upon association of a dimer is 50%.

6.4.2. Simulation of the stopped flow ATP binding measurements

Simulation of the ATP binding to Hsp90 from single molecule data was done as follows: The concentration of free ATP is equal to the unbound Hsp90 since ATP and Hsp90 were mixed at equal concentrations and only one ATP binding site of Hsp90 can be occupied by ATP. The rates of the ATP binding and unbinding of the open and closed conformations were taken from Fig. 11.4. The time development of the ATP unbound (u) and bound (b), open (o) and closed (c) Hsp90 monomer concentration (C) can be described with the following equation:

$$C_{uo}(t+\Delta t) = C_{uo}(t) + \left\{ -k_{5+}\frac{1}{2}C_{uo}(t)\left(C_{uo}(t)+C_{uc}(t)\right) + k_{5-}C_{bo}(t) - k_{6+}C_{uo}(t) + k_{6-}C_{uc}(t) \right\}\Delta t \quad (6.2)$$

$$C_{uc}(t+\Delta t) = C_{uc}(t) + \left\{ -k_{7+}\frac{1}{2}C_{uc}(t)\left(C_{uo}(t)+C_{uc}(t)\right) + k_{7-}C_{bc}(t) + k_{6+}C_{uo}(t) - k_{6-}C_{uc}(t) \right\}\Delta t \quad (6.3)$$

$$C_{bo}(t+\Delta t) = C_{bo}(t) + \left\{ k_{5+}\frac{1}{2}C_{uo}(t)\left(C_{uo}(t)+C_{uc}(t)\right) - k_{5-}C_{bo}(t) - k_{6+}C_{bo}(t) + k_{6-}C_{bc}(t) \right\}\Delta t \quad (6.4)$$

$$C_{bc}(t+\Delta t) = C_{bc}(t) + \left\{ k_{7+}\frac{1}{2}C_{uc}(t)\left(C_{uo}(t)+C_{uc}(t)\right) - k_{7-}C_{bc}(t) + k_{6+}C_{bo}(t) - k_{6-}C_{bc}(t) \right\}\Delta t \quad (6.5)$$

The rate constants (k) are the inverse of the mean dwell times (τ), which were taken from Tab. B.2. The starting concentration of Hsp90 and ATP were chosen to be 500 nM like in the stopped-flow experiment. Under this condition, the concentration of free ATP is equal to $C_{uo}(t) + C_{uc}(t)$. Because the ATP concentration in the single-molecule measurement was 200 nM, whereas in the stopped-flow measurement it was 500 nM, the binding rate had to be divided by 200 nM and multiplied with 500 nM (second-order reaction). Because the opening and closing rates for Hsp90 are approximately the same, the starting concentration of the open and closed Hsp90 states without ATP were set equal (250 nM each). The time step Δt was set to 2 ms like in the stopped-flow measurement. The overall concentration of Hsp90 with ATP bound—which is plotted in Fig. 11.7B —finally is

$$C_b^{o/c}(t) = C_{bo}(t) + C_{bc}(t) \quad (6.6)$$

6.5. Fluorescence anisotropy measurements

Measuring the fluorescence anisotropy allows to estimate the rotational diffusion and thus the rotational freedom of a dye. This is important for FRET measurements since the FRET efficiency is also depending on the relative orientation of the interacting dyes. Anyway in the Förster theory the dyes are assumed to have no relative favored orientation . To check this the rotational diffusion of the single dyes is measured by fluorescence anisotropy. Fluorescence anisotropy measurements are simple bulk fluorescence measurements, but with polarization filters in both the emission and excitation pathways. Thus only dyes are excited which lie parallel to the polarization of the excitation beam. After the excitation it takes several nanoseconds until the fluorescence photon is emitted. Since the dye rotates during that time the emitted light is less linearly polarized. This process of losing linear polarization is called anisotropy decay. The emission polarization filter changes between positions parallel and perpendicular to the polarization of the incoming beam and the

fluorescence is measured for both positions. The anisotropy value is obtained as:

$$a = \frac{I_{\shortparallel} - G\, I_{\perp}}{I_{\shortparallel} + 2\, G\, I_{\perp}} \tag{6.7}$$

with $I_{\|}$and $I_{\perp}$ as the emission intensities with polarization parallel and perpendicular to the excitation polarization and G a correction factor, which corrects the different detection efficiencies for the different polarizations.

The value ranges from 0 to 0.4 where 0 means a freely rotating dye and 0.4 a completely fixed dye (the mathematical possible value of 1 is not achieved because of the random rotational orientation of the dyes in solution). Since upon attachment of a dye one degree of freedom gets lost a attached dye is regarded as rotating freely when it has an anisotropy value of 0.2 or less [57].

7. Surface passivation and protein fixation

Since the measured protein has to stay in the evanescent field of the TIRF setup (for technical details see sec. 8.1) and thus near the surface during the measurement, the sample has do be fixed to the surface of the measurement chamber. Anyway unspecific contacts and binding that might influence the dynamics or even destroy the protein have to be excluded. To achieve both the glass surface of the measurement chamber were passivated with polyethyleneglycol (PEG) that carries to a small extent biotin. Streptavidin binds with a K_d of 10^{-15}M to this biotin. Since streptavidin is a tetramer it offers binding sites on which other biotinylated compounds can be bound. In detail surface fixation was either done directly by biotinylated protein (sec. 7.2.1) or by biotinylated vesicles with encapsulated protein (sec. 7.2.2).

7.1. PEGylation of the measurement chambers

7.1.1. Cleaning of the microscopy quartz slides

Prior to surface passivation the quartz slides had be rigorously cleaned. After every cleaning step the quartz slides were rinsed 5 times with ultrapure water. The detailed procedure is as follows: The used measurement chambers were immersed in 2% Hellmanex (Hellma) and sonicated for 15min. After that the cover slips and the Tegaderm spacers could be easily removed. The quartz slides were again sonicated with 2% Hellmanex for 15min. To remove fatty remnants from the surface the quartz slides were put into ethanol and rubbed with a cloth. After another round of sonicating in Hellmanex for 15min and water also for 15min, the quartz slides were incubated in Piranha (H_2SO_4/H_2O_2= 3/1, vol/vol) for at least 3h at 60°C. After that the slides were again sonicated with Hellmanex and water, both 15min

followed by another incubation for 3h at 60°C in RCA ($H_2O/H_2O_2/NH_3$= 5/1/1, vol/vol/vol) . Finally the slides were sonicated in 2% Hellmanex and stored in Hellmanex until surface passivation.

7.1.2. PEGylation of the quartz slides

The whole procedure was done in the cooling room at 6°C because it turned out that elevated temperatures especially more than 25°C drastically disturb the surface passivation. Quartz slides stored in 2% Hellmanex (Hellma Analytics) were sonicated in fresh 2% Hellmanex for 15min, rinsed 5 times with water, sonicated in water for 15min and again rinsed 5 times with water. The cleaned slides were removed from the water, the excess water was allowed to drop off and the quartz slides were put into acetone (p.a., Sigma Aldrich) for 10min. After that the quartz slides were placed in 200mL acetone with 1mL Vectabond. After 5-10min the slides were removed the excess acetone allowed to drop off and swayed in at least 500mL water. The slides covered with Vectabond were placed on petri dishes filled with water. On the vectabond/glass surface 70µL of PEG-NHS solution (3mg Bioin PEG NHS, 80mg Metoxy-PEG-NHS dissolved in 600µL 100mM $NaHCO_3$, all polyethylenglycols obtained from Rapp Polymere) were dropped on the surface. The liquid layer was covered with a cleaned (sonicated in Hellmanex and water) cover slip. Wet clothes were placed around the petri dish with the slides on top and covered with a styrofoam box to prevent the slides from light and drying out. The slides were incubated over night. The next day the cover slips were removed and the slides swayed in at least 500mL water. The passivated slides were dried with nitrogen and stored in staining chars protected form light with aluminum foil.

7.2. Protein fixation

Proteins were fixed to the surface either directly by covalently binding biotin to the protein or encapsulating the protein into vesicles and fixing those vesicles onto the surface. Immobilizing proteins in vesicles has the advantage that the proteins can still diffuse freely at high local concentrations (up to µM). Anyway since only vesicles are chosen for the data evaluation that contain one molecule of each differently labeled species, the exact concentration inside the vesicles is defined by the size

of the vesicles, which is varying. Thus the effective concentration is varying. Is the protein directly fixed to the surface the concentration of the freely floating molecules is constant for every fixed molecule. Overall vesicles are very helpful when intermolecular interactions are studied but direct fixation allows a more precise estimation of kinetics. Another problem using vesicles is that if ATP is used at low concentrations (< µM) already the cleavage of few ATP molecules changes the concentrations of ATP and ADP inside the vesicle extremely. Both types of surface fixations where used in this study and are described below.

7.2.1. Surface fixation via biotinylation

Attachment of biotin to the protein was done by amino reactive NHS-biotin. Since a protein contains several amino groups the biotinylation is not completely regioselective. Therefore there is the risk that amino groups are modified that play a crucial role in the catalytic activity of Hsp90. To avoid this, biotinylation was done at low pH that favors the reaction of the N-terminal amino group, in the presence of AMP-PNP that leads to the closed state of Hsp90 and with moderate concentration of NHS-biotin. In detail the acceptor labeled protein was diluted with an equal amount of measurement buffer pH 4.2. Afterward 125-fold excess of AMP-PNP was added and incubated for 30min at RT. An the protein concentration equimolar amount of NHS-biotin was added to the protein solution and the solution was incubated at RT for 60min. To remove non bound biotin, the protein was washed three times with a vivaspin column. Spinning was done only at 10000rpm to avoid heating of the sample. The biotinylated acceptor dye bearing protein was exchanged with the donor bearing protein as described above (sec. 5.3).

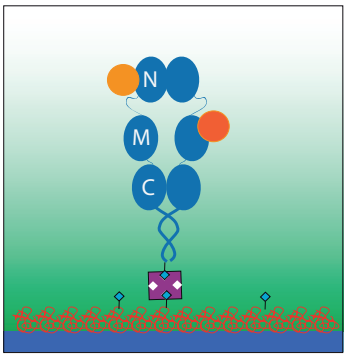

Figure 7.1.: Fixation of Hsp90 with a coiled coil via NHS-biotinylation. The biotin binds to the surface via biotin neutravidin binding.

7.2.2. Surface fixation by vesicle encapsulation

7.2.2.1. Preparation of lipid stock

The lipids were bought as chloroform solution of 1,2-dipentadecanoyl-sn-glycero-3-phosphocholine with 1% (mol : mol) 1,2-dipalmitoyl-sn-glycero-3-phosphoethanolamine-N-(cap biotinyl) (both from Avanti Polar Lipids). The needed amount of lipids were transferred into a glass vial with a hamilton syringe. The chloroform was removed in vacuum. After that hepes buffer was added to obtain a concentration of 10mg/mL. The immersion was frozen in liquid nitrogen and thawed at 42°C afterward, followed by sonicating the solution for 15min. This procedure was repeated 4 times. The obtained solution was diluted to a concentration of 4mg/mL and aliquoted and frozen at -20°C.

7.2.2.2. Protein encapsulation

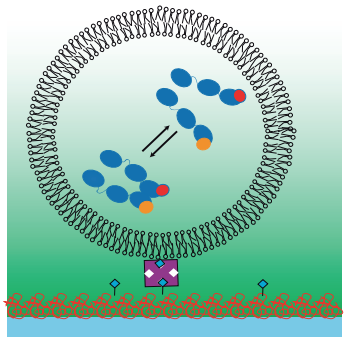

Figure 7.2.: Hsp90 captured in a vesicle. The vesicle if fixed to the surface via biotin neutravidin binding. The Hsp90 is fixed on the surface, but can at the same time diffuse freely at a high local concentration.

The homodimers of yHsp90 or HtpG were diluted in hepes buffer to a concentration of 200nM each monomer (that corresponds to less than one monomer in each vesicle in average). To reach full subunit exchange the protein solution were incubated at 37°C; yHsp90 15min and HtpG 25min. Encapsulation itself was done by an extruder: A device in which a buffer-lipid-emulsion can be pressed through a membrane with very small pore size (200nM in this case). Pressing the lipid mixture several times through this membrane leads to the formation of unilammellar vesicle with a pretty narrow size distribution around the pore size. Since the lipid membranes are disrupted and reform during this process, the proteins in the solution are partially encapsulated in the vesicles. The lipid protein mixture

was pressed 31 times through the extruder. Afterward the obtained vesicle solution was diluted to concentrations of several pM (protein monomer concentration). To remove aggregates the diluted solutions are spun down in a cooled centrifuge at 14000rpm 15min, the supernatant is used for the measurement. For measurements in the presence of high ATP concentrations (2mM), ATP was added to the protein/lipid solution as well as to the buffer surrounding the vesicles during the measurement.

8. Single molecule setup TIRF and measurements

8.1. Four-color single molecule TIRF setup

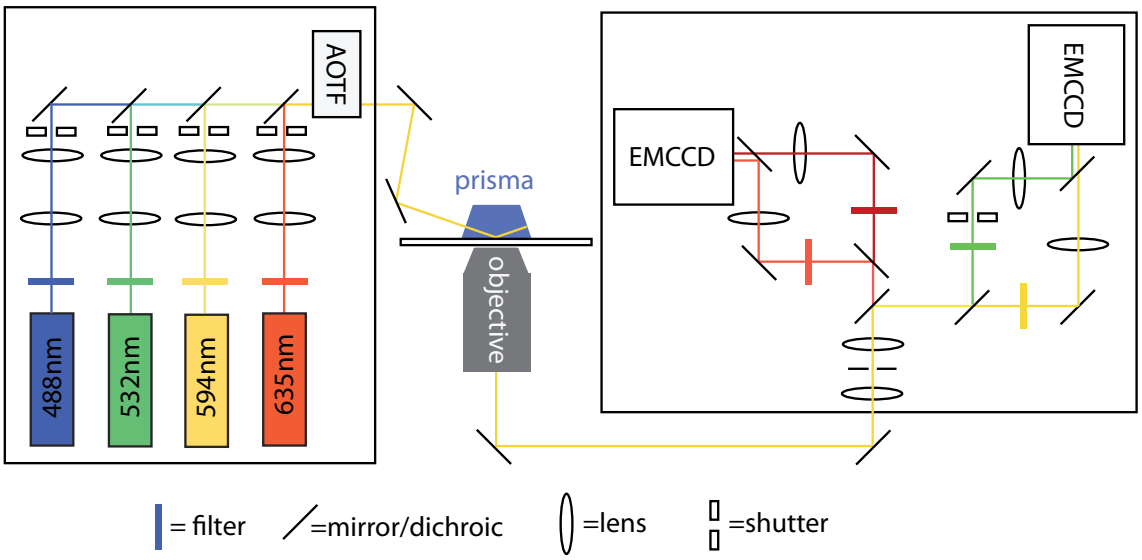

Figure 8.1.: Scheme of the four color single molecule FRET setup. The function is described in the text.

During this work the setup was expanded two times from a two over three to a four color FRET setup. Here I want to describe only the latest - the four color - setup.

Four excitation lasers are used with wavelengths at 473nm (Cobolt Blues, Cobolt), 532nm (Compass 215M, Coherent), 594nm (Cobolt Mambo, Cobolt) and 635nm (Lasiris, Stocker Yale). The laser light of the 473nm, 532nm and 594nm lasers is first passing through clean up filters (all filters in this setup from AHF Analysetechnik) to remove unwanted sidepeaks. Afterward the laserbeams are lead through a kepler

telescope with 50mm followed by 100mm focus width to increase the laser beam diameter and to correct divergence of the laser beam. The second lens is slightly rotated to achieve an elongated beam profile in the measurement chamber which results in better illumination of the sample. The four laser beams are overlaid with dichroic mirrors and brought onto an acusto-optical tunable filter (AOTF, AOTFnC-VIS-Tn, AA Opto-Electronic), which allows intensity control and fast pulsing of the lasers. Behind the AOTF the laserbeams are brought onto the measurement chamber via a prism. The beam is totally reflected on the measurement chamber producing an evanenscent field in the measurement chamber. Beyond the measurement chamber an Apo TIRF 60x, 1.49 N.A., oil objective (Nikon) is collecting the fluorescence light. The fluorescence light is lead into the detection pathway. In this part of the setup only biconvex quartz glass bestform lenses (Qioptiq) are used to avoid auto fluorescence of the glass and spheric abberations from the lenses. The whole detection pathway is also built in 2inch diameter optics. First the emitted light goes through a Kepler telescope with 100mm lenses. In the middle of the telescope a rectangular area is cut out of the detection beam with half the size of the camera chip. The slit here works as a kind of pinhole too and limits the Z-direction of the detected light and decreases background. After that the light is separated via dichroic mirrors and filtered. In every light channel there is a separate 200mm lens that focuses the fluorescence light onto the camera. Those lenses are placed on translational stages which allow to focus every channel independently. This construction is crucial to overcome the problem that different colors have different focal distances and thus can not be focused on the camera chip with one shared lens. Because of limited space for the four color detection two cameras (Andor iXon, Andor) were used with two color channels on each camera. There is a lateral offset between the two channels on each camera. Thus the same area of the measurement chamber is displayed twice, but for two different colors (Fig. 8.2). To block scattered laser light of the green laser which would go directly into the green detection channel a shutter is installed in that detection pathway. This shutter is closed when the green laser is switched on. The measurement chamber was placed in a styrofoam box with additional peltier elements (QC-127-1.4-8.5MD, Conrad) and a temperature control (Peltier-Controller 12 V QuickCool QC-PC-C01C, Conrad) to carry out measurements at stable temperatures. A scheme of the whole setup is shown in Fig. 8.1.

8.1.1. Software control of the setup

For measurements with this setup two cameras, mechanical shutters for each laser, the shutter in the detection pathway and the AOTF have to be controlled precisely and simultaneously, but sometimes with different pulse patterns. Since this was not able with the used AndorIQ software (Andor, Belfast, UK) - contrary to suppliers information - I added a PCIexpress card with an external clock (PCIe-6535, National Instruments) to the control computer and wrote a control software in LabView (LabView11, National Instruments). This program in combination with the PCIe card allows to generate all types of trigger patterns at multiple channels with ns accuracy. Thus all necessary devices could be directly controlled with the LabView software.

8.1.2. Data analysis and theory

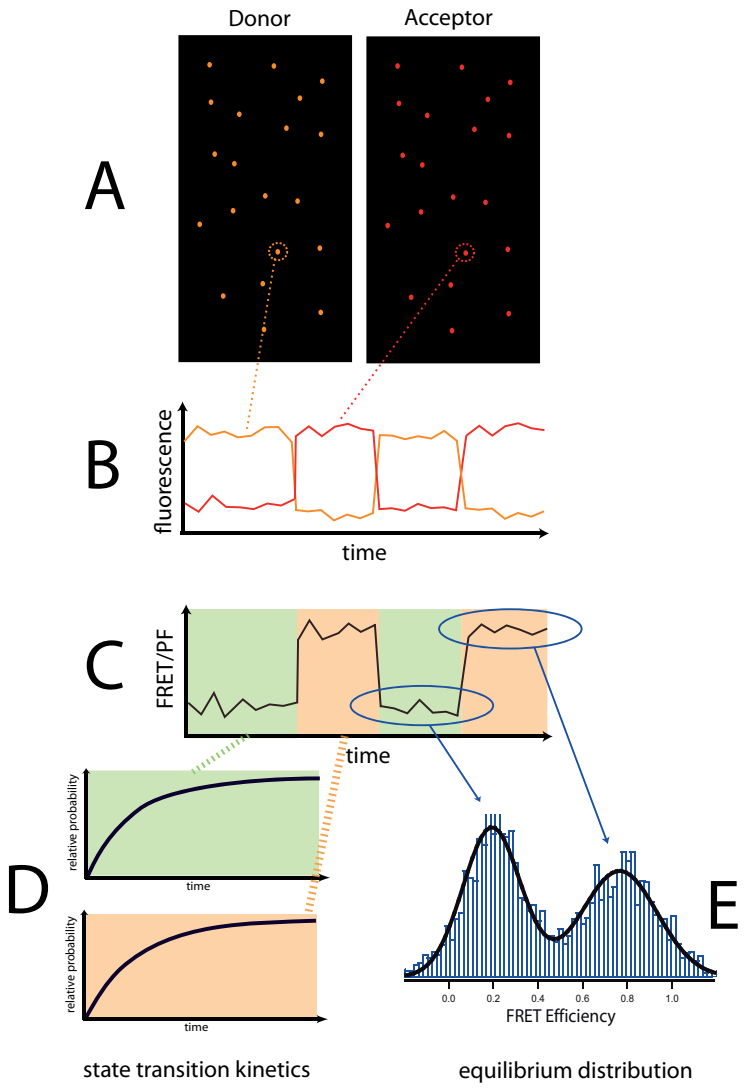

Figure 8.2.: Scheme of FRET analysis shown for two colors. (A) The obtained movies show several single molecules attached to the surface over time for donor and acceptor dye separately. (B) From these movies the intensities over time for single dye pairs are extracted. (C) Those fluorescence signals are converted into FRET efficiency curves according to formula 8.17.(E) Histograming those FRET curves allows to estimate the equilibrium FRET distributions of the observed states. (D) Histograms of the dwell times allow to estimate transition rates for every transition separately.

The obtained movies were cut according to the single detection channels (Fig. 8.2 A). For the data analysis the brightest spots in the acceptor channels were searched by

a threshold criterion. Its intensity was plotted versus time together with the intensity of this spot in the other detection channels. Thus an intensity versus time plot for all detection colors was obtained. In these curves I searched for anti-correlated intensity changes typical for FRET (Fig. 8.2) B. Those curves were selected and analyzed. First the background signal - the signal after complete dye bleaching - was subtracted . Then the FRET efficiencies/partial fluorescence intensities were calculated according to sec. 8.1.2.1 (Fig. 8.2 C).All obtained FRET/partial fluorescence values were plotted in histograms (Fig. 8.2) E. From this histograms it could already be seen how many states with different FRET efficiencies exist and how strong this states are populated. To obtain the transition rates between the different states two approaches were used: For two color FRET the minimum between the obtained peaks in the FRET histograms was used as threshold. Every time this threshold was crossed by the FRET signal this was counted as transition and thus dwell times for the single states could be obtained. Anyway this procedure is not straightforward for multicolor FRET data since here exist at least two partial fluorescence signals, the corresponding histograms become multidimensional. In this case Hidden-Markov analysis was used. Moreover Hidden-Markov is much less noise sensitive than a threshold criterion. Hidden-Markov analysis is described below (sec. 8.1.2.3).

8.1.2.1. Calculation and correction of FRET efficiencies

The FRET efficiency is defined - analog to a quantum efficiency - by the amount of photons transferred to the acceptor divided by all photons absorbed by the donor.

$$E_{FRET} = \frac{k_{FRET}}{k_{FRET} + k_{rad} + k_{non-rad}} \tag{8.1}$$

k_{FRET} is the FRET rate, whereas $k_{rad} + k_{non-rad}$ are the radiative and non-radiative decay rates of the donor.

The emission intensity of a dye is than given as the quantum efficiency Q_i times the up-taken photons per time N_i.

$$I_i = Q_i N_i \tag{8.2}$$

Since the acceptor can only take up photons by FRET (cross excitation is neglected here and correction for it is shown below) the number of photons taken up by the acceptor in time is just given by

$$N_A = \frac{k_{FRET}}{k_{non-rad} + k_{rad} + k_{FRET}} N_D^{exc} \tag{8.3}$$

where N_D^{exc} is the number of photons in time taken up by the donor via absorbtion. Since this number is equal to

$$N_D^{exc} = \frac{I_D}{Q_D} + \frac{I_A}{Q_A} \tag{8.4}$$

the FRET efficiency becomes

$$E_{FRET} = \frac{\frac{I_A}{Q_A}}{\frac{I_D}{Q_D} + \frac{I_A}{Q_A}} \tag{8.5}$$

by combining the equations 8.2, 8.3 and 8.4.

Taking also into account that the emitted intensity I_{em} can not directly be measured, but the measured intensity I_{meas} is biased by the detection efficiency of the setup ϵ

$$I_i^{meas} = \varepsilon_i I_i \tag{8.6}$$

one obtains with 8.5

$$E_{FRET} = \frac{I_A^{meas}}{I_A^{meas} + \frac{\epsilon_A Q_A}{\epsilon_D Q_D} I_D^{meas}} = \frac{I_A^{meas}}{I_A^{meas} + \gamma I_D^{meas}} \tag{8.7}$$

γ becomes a correction factor for the detector efficiency and the quantum efficiency

of the used dyes.

$$\gamma = \frac{\varepsilon_A Q_A}{\varepsilon_D Q_D} \tag{8.8}$$

Within one measurement series the excitation intensity is constant. Thus equation 8.4 with equation 8.6 for two different FRET values and correspondingly different I_D^{meas} and I_A^{meas} can be rewritten as:

$$\frac{I_D^{meas}}{\varepsilon_D Q_D} + \frac{I_A^{meas}}{\varepsilon_A Q_A} = \frac{I_D^{meas'}}{\varepsilon_D Q_D} + \frac{I_A^{mea'}}{\varepsilon_A Q_A} = N_D^{exc} = const. \tag{8.9}$$

with equation 8.8 the γ factor can be thus written as

$$\gamma = \frac{\varepsilon_A Q_A}{\varepsilon_D Q_D} = \frac{I_A^{meas'} - I_A^{meas}}{I_D^{meas} - I_D^{meas'}} \tag{8.10}$$

Thus the γ factors can be estimated with every two different measured FRET values at the same laser intensity. Anyway since the quantum efficiency might be also depending on the chemical environment the γ factor is normally estimated with the same sample used also for the measurement.

Anyway in a real measurement the emission spectra of the dyes overlap and the emission light of the two dyes can never be perfectly separated (moreover dichroic mirrors and filters are never perfect) - this effect is called crosstalk. Moreover since also the absorption spectra of dyes are not a delta function the laser that excites the donor can also to some extent excite the acceptor - this effect is called cross excitation. Both effects crosstalk and cross excitation change the measured intensity compared to the really emitted intensity of the dyes and thus have to be eventually corrected. The crosstalk and cross excitation are both also influencing the γ factor. Thus directly estimating the γ factor from measured intensities might lead to wrong results. In the following is shown how data can be corrected concerning crosstalk and cross excitation.

The crosstalk is corrected with the β factor, which is given as the amount of measured

light in the acceptor channel in the presence of donor only upon donor excitation.

$$\beta = \frac{I_A^{meas}}{I_D^{meas}}\Bigg|_{Donor-Excitation}^{onlyDonor} \tag{8.11}$$

The cross excitation is corrected by the δ factor which gives the amount of absorbed photons of the acceptor compared to the photons absorbed by the donor at the same laser intensity, but no interaction between acceptor and donor.

$$\delta = \frac{I_A^{meas}}{I_D^{meas}}\Bigg|_{Donor-Excitation}^{DonorandAcceptor} \tag{8.12}$$

Since the measured intensity is given as

$$I_i^{meas} = \frac{\varepsilon_i Q_i \mathcal{E}_i^{excitationWL} I^{excitation}}{N_A} \tag{8.13}$$

with $\mathcal{E}_i^{escitationWL}$ as the absorption coefficient at the excitation wavelength, $N_A$as the Avogadro constant and $I^{excitation}$as the excitation intensity.

combining equations 8.12, 8.13 and 8.10 one obtains for the δ factor

$$\delta = \gamma \frac{\mathcal{E}_A^{donorWL}}{\mathcal{E}_D^{donorWL}} \tag{8.14}$$

To minimize cross excitation effects the γ factors is obtained by using the change in FRET efficiency to zero upon acceptor bleaching. After the acceptor bleaching the intensity of the acceptor is zero and everything that is measured in the acceptor channel is caused by crosstalk and allows estimation of the β factor according to Equation 8.11 . How to obtain the γ factor is shown in Equation 8.10 with I' as the intensities before and I as the intensities after bleaching. The intensity of the

acceptor is given as

$$I_A^{'} = I_A^{meas'} - \beta I_D^{meas'} - \delta \left(I_D^{meas'} + \frac{I_A^{meas'} - \beta I_D^{meas'}}{\gamma} \right) \tag{8.15}$$

the acceptor intensity is zero after bleaching.

$$\gamma = \frac{I_A^{meas'} \mathcal{E}_D - \beta I_D^{meas'} \mathcal{E}_D - \mathcal{E}_A I_A^{meas'} + \mathcal{E}_A \beta I_D^{meas'}}{\mathcal{E}_D I_D^{meas} - \mathcal{E}_D I_D^{meas'} + \mathcal{E}_A I_D^{meas'}} \tag{8.16}$$

and the corrected FRET efficiency can be obtained as.

$$E_{FRET} = \frac{I_A^{meas} - \beta I_D^{meas} - \delta \left(I_D^{meas} + \frac{I_A^{meas} - \beta I_D^{meas}}{\gamma} \right)}{I_A^{meas} - \beta I_D^{meas} - \delta \left(I_D^{meas} + \frac{I_A^{meas} - \beta I_D^{meas}}{\gamma} \right) + \gamma I_D^{meas}} \tag{8.17}$$

In practice the crosstalk and cross excitation are very small in the case of two color FRET measurement. Thus these correction factors were ignored for the here shown two color measurements. Anyway the more colors one uses the more overlap of the excitation and emission spectra exists and the more important this corrections get. For the three color measurements also the crosstalk was taken in to account.

Anyway for multicolor measurements also another problems arises. The FRET efficiency can not directly be obtained from the measured intensities. Lets assume we have three interacting dyes D, A1, A2 with increasing absorbtion and emission wavelengths. Lets assume that only Donor D is excited and all energy is transferred to dye A2. In this case we don't know if all energy is transferred form D via A1 to A2 or directly form D to A2. But concerning the FRET efficiencies in the first case the FRET efficiency between D and A1 is 1 whereas in the second it is 0 - a big difference. Since the distance between the dyes is not depending on its relative emission intensities but on its FRET rates one has to calculate the FRET rates from the the measured intensities. The exact mathematical procedure is shown in the Appendix B , anyway the results are shown also here:

$$k_{FRET}^{d\to a1} = -\frac{PF_1 k_{rad}^{d}(k_{rad}^{a1}\tau_d E_{ALEX}^{FRET} - k_{rad}^{a1}\tau_d - E_{ALEX}^{FRET}Q_{a1}^{nf})}{Q_{a1}^{nf}k_{rad}^{a1}\tau_d(PF_2E_{ALEX}^{FRET} - PF_2 + PF_1E_{ALEX}^{FRET} - PF_1 - E_{ALEX}^{FRET} + 1)} \tag{8.18}$$

$$k_{FRET}^{d\to a2} = -\frac{\left(PF_2 k_{rad}^{a1}\tau_d E_{ALEX}^{FRET} - PF_2 k_{rad}^{a1}\tau_d + PF_1 E_{ALEX}^{FRET}Q_{a1}^{nf}\right)k_{rad}^{d}}{Q_{a2}^{nf}k_{rad}^{a1}\tau_d(PF_2E_{ALEX}^{FRET} - PF_2 + PF_1E_{ALEX}^{FRET} - PF_1 - E_{ALEX}^{FRET} + 1)} \tag{8.19}$$

and

$$k_{FRET}^{a1\to a2} = \frac{E_{ALEX}^{FRET}}{(E_{ALEX}^{FRET} - 1)\tau_d} \tag{8.20}$$

where k_{FRET} are the FRET rates between the dyes, k_{rad} are the radiative depopulation rates of the dyes, τ are the overall lifetimes , Q^{nf} are the quantum efficiencies and $PF_{1/2/3}$ are the partial fluorescence intensities and E_{ALEX}^{FRET} is the FRET efficiency upon excitation of A1.

8.1.2.2. Distance estimation from FRET efficiency

From the obtained FRET rates/efficiencies the distances between the dyes can be estimated. According to Förster theory [58], that describes the FRET process as a coupling of dipoles - the FRET rate is depending on the inverse distance to the power of six.

$$k_{FRET} = \frac{1}{\tau_D}\left(\frac{R_0}{d}\right)^6 \tag{8.21}$$

with $k_{FRET\ is}$the FRET rate, $\tau_D$the fluorescence lifetime of the donor in absence of FRET and R_0 the so called Förster distance. Hereby the FRET rate and efficiency are coupled according to 8.1 with

$$k_{FRET} = \frac{1}{\tau_D}\frac{E_{FRET}}{1 - E_{FRET}} \tag{8.22}$$

The Förster distance is given as:

$$R_0^6 = \frac{9\,Q_0\,(ln10)\,\kappa^2}{128\,\pi^5\,n^4\,N_A} \int f_D(\lambda)\epsilon_A(\lambda)\lambda^4 d\lambda \tag{8.23}$$

with Q_0 as the quantum yield in the absence of FRET, κ^2 the dipole orientation factor, N_A the Avogadro constant, n the refractive index of the medium, $f_D(\lambda)$ the fluorescence intensity normalized to an area of one and $\epsilon(\lambda)$ the absorption both as a function of the wavelength λ.

Thus the Förster distance is in principle a material constant of the dye. Anyway it has to taken into account that dye properties like spectra, lifetimes and rotational diffusion times can change upon attachment of dyes to proteins. Therefore distance estimations from FRET should be more taken as rough estimates. A detailed estimation of the Förster distance for C-terminal dynamics is given in sec. A.1. Anyway in all other cases the Förster distances for the free dyes given by the supplier (Atto-Tec) was used. To check whether the dye can rotate freely, anisotropy measurements have been done for all used dye-protein combinations as described in sec. 6.5

8.1.2.3. Hidden-Markov analysis

To obtained the kinetics from the observed single molecule trajectories for the multi-color FRET measurements Hidden-Markov-modeling (HMM) was used. In general Hidden-Markov modeling allows to reconstruct the sequence of states underlying a scattered signal. HMM can be applied to multidimensional data like multi-color FRET data. In detail the Viterbi algorithm was used to reconstruct the underlying sequence of states: The data consist of a sequence of observed values O which are caused by an underlying sequence of states s. The Viterbi algorithm searches the sequence of states S* that gives the maximum probability P to produces a sequence of observables O with a given model λ.

$$P(O, S^* \mid \lambda) = \underset{s}{max} P(O, S \mid \lambda) \tag{8.24}$$

To achieve this a the parameter δ is defined as a parameter for the maximal probability to produces a sequence of observables O_1,O_2,... with a certain sequence of

states s_1,s_2,... with the last state i .

$$\delta_t(i) = \max_{s_1,s_2,...,s_{t-1}} P(O_1, O_2, ..., O_t, s_1, s_2, s..., s_{t-1}, s_t = i \mid \lambda) \tag{8.25}$$

Thus the $\delta_t(i)$ are only locally maximized for the state i. To get a completely optimized sequence of states $\delta_t(i)$ has to be calculated iteratively for the whole sequence of observables. The $\delta_1(i)$ of the first time step is given as

$$\delta_1(i) := \pi_i b_i(O_1) \tag{8.26}$$

, with π_i as the equilibrium probability to find state i (start probability) and b_i the probability to observe the O_1 in the presence of state i (emission probability), which is given by the emission function 8.33.

For the following time steps the $\delta_{t+1}(j)$ at time step t+1 are derived from the $\delta_t(i)$ of the former time step:

$$\delta_{t+1}(j) := \max_i \{\delta_t(i) a_{ij}\} b_j(O_{t+1}) \tag{8.27}$$

, where a_{ij} is the transitions probability from state i to j.

For the last step the $\delta_T(i)$ is chosen in such a way that the $\delta_T(i)$ - which corresponds to the production probability - becomes maximized and thus represents the optimal sequence of states S*:

$$P^*(O \mid \lambda) = P(O, S^* \mid \lambda) = \max_i \delta_T(i) \tag{8.28}$$

We have now the optimal production probability P* but we want to have the optimal sequence of states S*. This is extracted by calculating for every iteration step of $\delta_t(i)$ in parallel a value $\psi_t(i)$ representing the most likely state transitions for every

time step. For the first time step this is,

$$\psi_1(i) := 0 \tag{8.29}$$

since there is now transition to backwards in time from this time step.

The remaining $\psi_t(i)$ are calculated iteratively :

$$\psi_{t+1}(j) := \underset{i}{argmax} \{\delta_t(i)\, a_{ij}\} \tag{8.30}$$

After the last iteration step the optimal sequence of states S* =(s_1*,s_2*,...,s_T*) can be reconstructed in reverse direction (s_T*, ..., s_2*, s_1*) as

$$s_T^* = \underset{i}{argmax}\, \delta_T(i) \tag{8.31}$$

and for all the other time steps:

$$s_t^* = \psi_{t+1}(s_{t+1}^*) \tag{8.32}$$

The Viterbi algorithm needs input values for the mean and deviation of the emission function and guesses for the transition rates. Fortunately the values for the emission function can be directly achieved from the measurements. Plotting the multi-color FRET data as described above the mean of the obtained peaks and the deviation can be directly obtained by fitting the peaks with the emission function in this case a simple Gaussian:

$$p\,(x,y) = \frac{1}{\sqrt{2\pi\sigma_x^2}} \exp\left(-\frac{(x-x_0)^2}{4\sigma_x^2}\right) + \frac{1}{\sqrt{2\pi\sigma_y^2}} \exp\left(-\frac{(y-y_0)^2}{4\sigma_y^2}\right) \tag{8.33}$$

The x_0 and σ values for the different states were estimated from the 2D histograms.

A guess for the transition rates can be obtained just by looking on which time scale the transitions can be observed. It has to be pointed out here, that there is no straight forward correlation between quality of the guesses and results of the HMM. For good data even bad guesses can produce a good outcome, whereas for bad data even good guesses might produce artificial results. The transition probabilities were optimized until the reconstructed FRET traces matched the measured data. This was double-checked by eye for every curve.

8.2. Single molecule measurements

8.2.1. Measurements of C-terminal dynamics

The Hsp90 was labeled at position 560C as described above. The encapsulation was done as described above. If measurements were done with nucleotides, the nucleotides were added both to the protein mixture prior to extruding and into the measurement buffer surrounding the vesicles in the measurement chamber. Time resolution was 1Hz (100ms integration, 900ms dark time).

8.2.2. Three color FRET measurements of N-terminal dynamics and ATP binding

For the three color FRET measurements the yHsp90/HtpG was directly biotinylated and fixed to the surface with neutravidin as described in sec. 7.2.1. The Hsp90 dimers were diluted in hepes buffer with 0.5mg/mL BSA to concentrations ranging from 50pM to 500pM. After incubating the measurement chamber with 0.5mg/mL neutravidin for 5-10min the non-bound neutravidin was flushed out with hepes buffer followed by hepes Buffer with 0.5mg/mL BSA. Hsp90 was flushed in with increasing concentration. When the right density on the surface was reached, the remaining Hsp90 was flushed out with hepes buffer. Finally 0,2µM $\gamma ATP Atto647N$ or $\beta ADP Atto647N$ was flushed into the chamber. The measurements were done with 200ms integration time and frames of 220ms and 1000ms for ATP and an integration time of 40ms and a frame time of 44ms for ADP.

8.2.3. HtpG measurements

The N-terminal dynamics of HtpG were studied by fixing C-terminal coiled coil, biotinylated HtpG via neutravidin to the measurement chamber (sec. 7.2.1). The sample was illuminated 200ms every second in the case of inter-domain measurements and 200ms with a 20ms delay time in the case of intramonomer measurements. For the measurements of HtpG's C-terminal dynamics the labeled protein was encapsulated in vesicles as described above for yHsp90. The C-terminal dynamics was recorded with 200ms camera illumination and 20ms delay with green laser excitation (532nm).

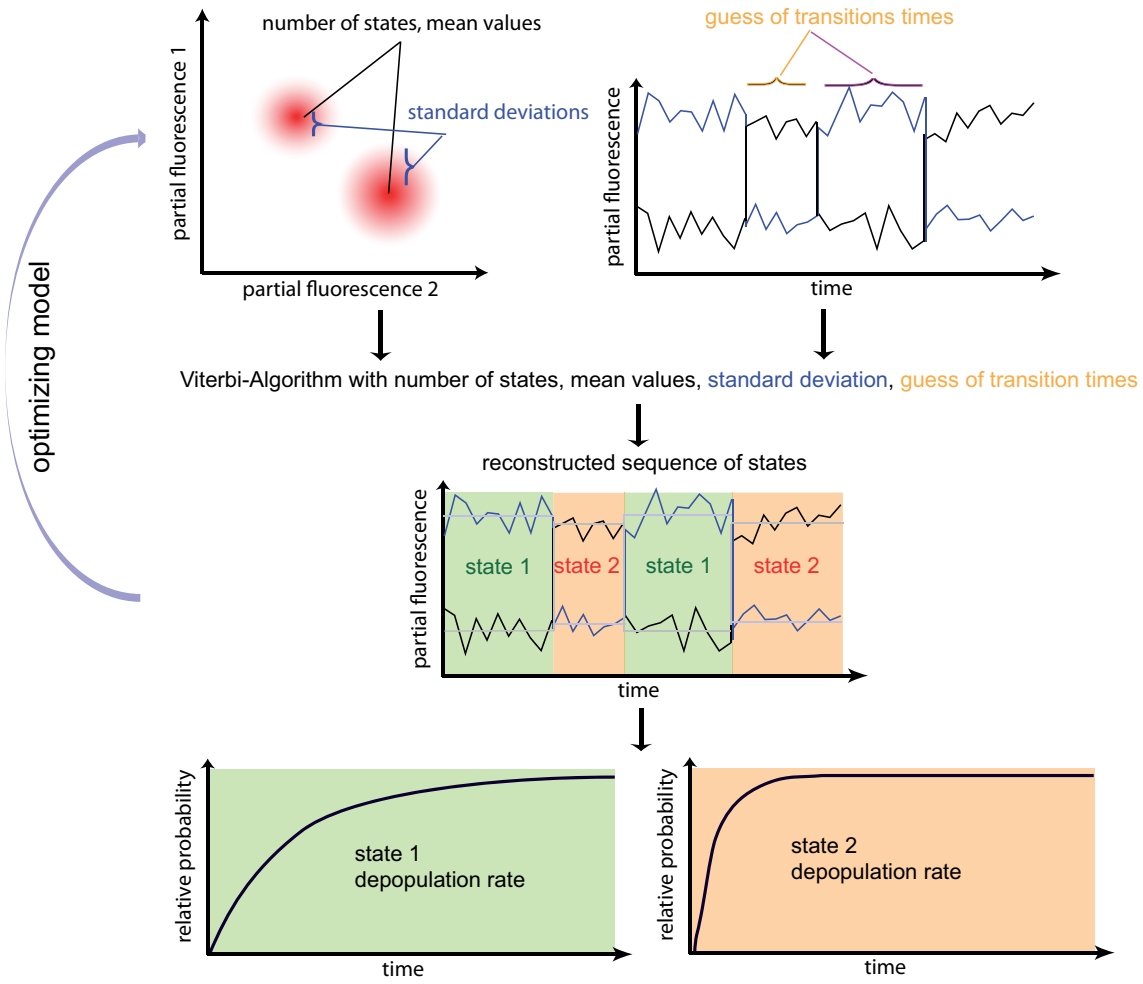

Figure 8.3.: Extracting transition rates with Hidden-Markov analysis. From the (multidimensional) FRET histograms the number of states and its mean FRET values as well as the standard deviations are obtained. From the single molecule time traces the timescale of the transitions can be estimated. These values are used by the Viterbi algorithm, which is calculating the most likely sequence of states leading to the measured curve. Checking how good the reconstructed curves fits to the measured curves allows optimization of the model parameters either manually - as done here - or by a learning algorithm like the Baum-Welch algorithm. From the obtained reconstructed sequence of states the transition rates can be obtained from histograms of the dwell times for every states. Thus even complex kinetics with a lot of states can be resolved with this approach, with essentially no assumption about the underlying model.

Part III.

Results and Discussion

9. N- and C-terminal dynamics of yHsp90

9.1. N-terminal conformational dynamics are only weakly coupled to ATP turnover

The work on the N-terminal dynamics of yHsp90 was mainly done by my precessor Moritz Mickler [48]. Anyway to give a complete picture I present a short overview here. As pointed out in the introduction yHsp90 was supposed to switch between a N-terminal open and closed state driven by ATP turnover. The common models proposed a binding of ATP in the open state followed by succesive closure, ATP cleavage and re-opening. This process was never shown directly and was mainly derived from combining data from different GHKL ATPases and the fact that the nucleotide analogue AMP-PNP leads to a permantely closed state. To check this hypothesis of ATP induced closing the relative movement of the two monomers in the Hsp90 dimer was observed by means of smFRET. Indeed the supposed open and closing movement could be found, but surprisingly this movement also exists in the absence of nucleotides. The addition of ATP and ADP slightly changed the dynamics, but nucleotides are not essential for N-terminal movement of yHsp90. Thus the N-terminal movements of yHsp90 are only weakly coupled to ATP turnover. We will come back to this later and understand in more detail how nucleotide binding and conformational changes are correlated in yHsp90.

10. C-terminal dynamics of yHsp90

Main parts of this chapter are puplished in [59]

10.1. Single molecule FRET allows to measure the C-terminal dimerization site separately

After finding surprisingly rich N-terminal dynamics, which are not strictly coupled to ATP turnover, the question arises, if there is also dynamics at the C-terminal dimerization site. This dimerization site was up to now regarded as permanently closed, because of Hsp90's low K_d of around 60nM. Anyway in bulk measurements it is very difficult to observe single binding sites, when there are several binding sites within the molecule. The measurement of dissociation or association kinetics in bulk are always an average over all existing dimerization sites. In contrast single molecule FRET allows to specifically extract the kinetics of one binding site and in the case of Hsp90 to observe the C-terminal binding site separated from N-terminal kinetics.

To directly monitor the dynamics of the C-terminal domain, a variant of yeast Hsp90 was created in which a cysteine was implemented at position 560 in the C-terminal domain (560C). The single cysteine in one monomer was labeled with the donor fluorophore Atto550, and in the second monomer with the acceptor fluorophore Atto647N. The dimers were then caged in lipid vesicles that were immobilized onto a solid substrate similar to the experiments by Cisse et al. [60] and Rhoades et al. [61] and as described in sec. 7.2.2. Functionality of the investigated constructs was tested by an ATPase assay (Fig. A.1). Also Sba1 binding experiments where suitable (Fig. A.1). The C-terminal interaction was measured by single-molecule fluorescence resonance energy transfer (smFRET) at 30°C in a two color TIRF microscope analogue to the system described above (sec. 8.1).

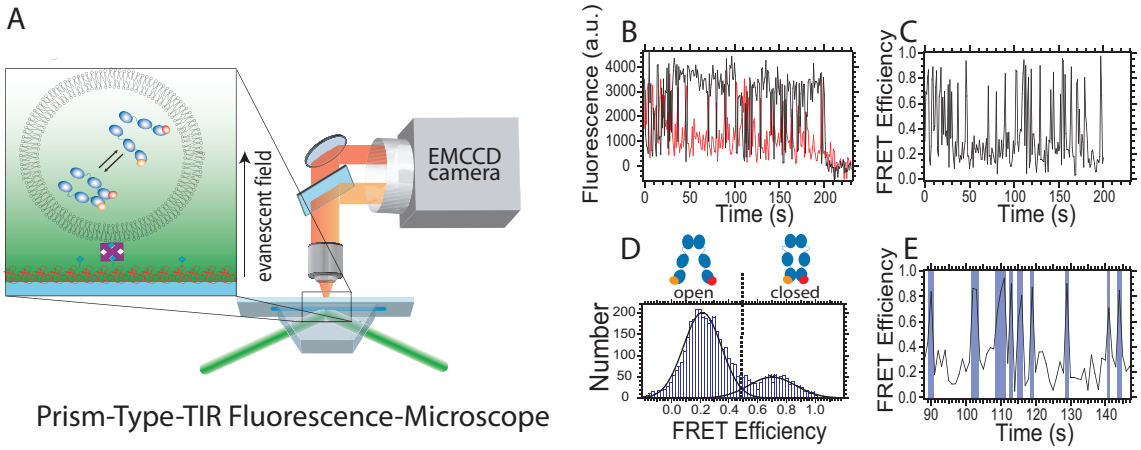

Figure 10.1.: Experimental setup. The Hsp90 molecules (size 5–10 nm) were caged in lipid vesicles with a diameter of about 200 nm (not to scale). The vesicles were immobilized via biotinylated lipids onto a solid substrate in a microfluidic chamber and mounted in a prism-type TIR microscope. Single-molecule fluorescence from the donor and acceptor were detected simultaneously by an electron multiplying charge coupled device camera (A). Matching time traces were overlaid (B) and FRET efficiencies determined (C). The cumulated histogram of all FRET efficiencies shows two states that are clearly separated by a threshold (D), which allow us to determine the rate constants from a separation of the time trace into open and closed states (E). For details see also sec. 8.1

C-terminal open-close dynamics on the time scale of seconds could be observed. This is in contrast to current models of Hsp90 that assume the C-terminus to be closed on time scales of 100 s [62, 41]. Several bulk experiments [63, 28] and the single-molecule experiments [48] show that the N-terminal domain is very stably dimerized in the presence of AMP-PNP (Fig. 10.2A). Surprisingly, even under these conditions the C-terminus shows opening and closing dynamics (Fig. 10.2B) clearly demonstrating that a N-terminal closed state does not result in a C-terminal closed state. In contrast, addition of the cochaperone Sti1 keeps the C termini mainly closed (Fig. A.2B).

The FRET efficiencies allow to estimate the distances between the fluorophores in the C-terminally open and closed state. The anisotropy values (sec. 6.5) were 0.23 for the donor and 0.18 for the acceptor dye, and the distance values should therefore only be taken as a rough estimate. The obtained distances are in all cases around 6.4 nm for the open and 4.3 nm for the closed state. The length of the linker between the cysteine and the fluorophore is 0.8 nm in both cases. These distances are in

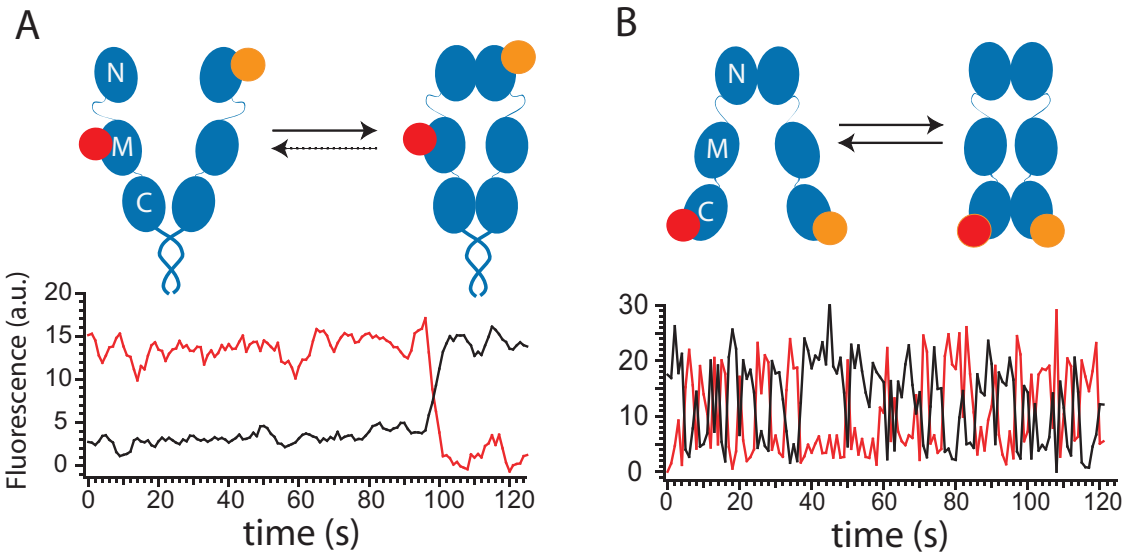

Figure 10.2.: Comparison of N- and C-terminal dynamics of Hsp90. Exemplary fluorescence time trace of the N-terminal (A) [48] and C-terminal (B) dimerization kinetics of Hsp90 with 2mM AMPPNP. (Top) Schematics of the various conformations. To investigate the N-terminal kinetics, a coiled coil motive was introduced at the C-terminus to allow for longer observation times; this did not change the dynamics [48]. (Bottom) Fluorescence signal of the donor (black trace) and the acceptor (red trace). The N-terminus stays closed (high acceptor signal) on the time scale of the experiment in A until the acceptor bleaches after around 100 s, while there is kinetics at the timescale of seconds at the C-terminus.

very good agreement with the crystal structure where the distance between the two cysteines is around 3.5 nm (in the closed state without linker). For determination of the Förster distance see sec. A.1. As the vesicle size is 200 nm, complete dissociation of the dimer (N- and C-terminal open) would result in a FRET efficiency of zero and can therefore be excluded on the time scale of the experiment (Fig. A.2A).

10.2. Nucleotides influence the C-terminal dynamics

After observing surprisingly fast dynamics in the C-terminal domain, the question arises whether this dimerization is regulated. Because Hsp90 function critically depends on ATP binding and hydrolysis, the described experiment was repeated under different nucleotide conditions. First, I used the natural nucleotides ATP and ADP and compared the results to the situation without nucleotide. I compiled the FRET efficiencies into histograms like the one depicted in Fig. 10.3 and described in

sec. 8.1.2. The area underneath the two peaks in these FRET histograms corresponds to the occupancy of the two states: Low FRET indicates that the C-terminus is in an open state, and high FRET indicates that the C-terminus is in a closed state. As can be seen in Fig. 10.3, without nucleotide the C-terminal domains are about 43% open and 57% closed. In the presence of ATP, this distribution is almost reversed, and with ADP the equilibrium is even more shifted to the open state. These observations are contrary to the situation at the N-terminal domain, where no strong influence of ATP or ADP on the dimerization equilibrium was found [48, 28].

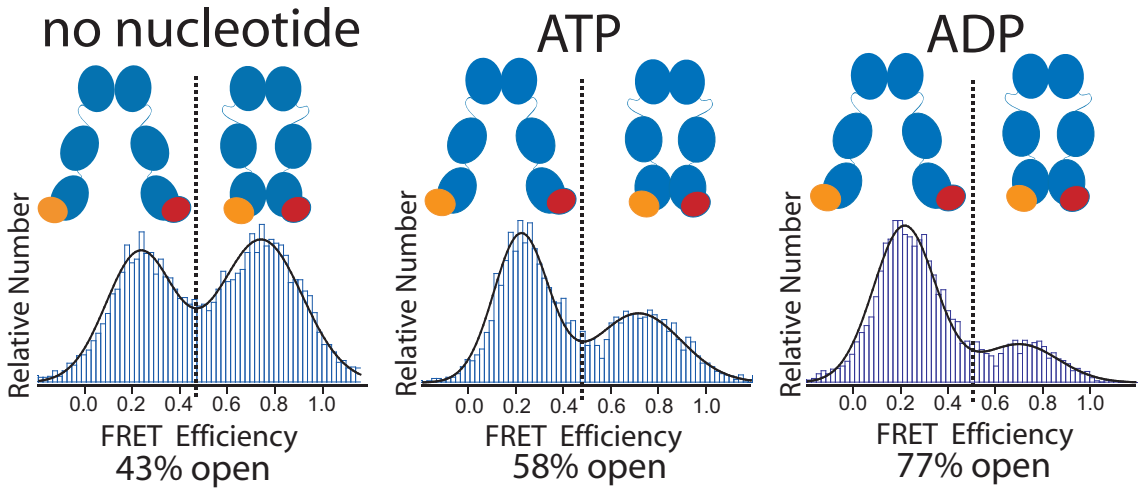

Figure 10.3.: Effect of nucleotide on the C-terminal dimerization. Relative amount of observed FRET efficiencies between donor (orange) and acceptor molecule (red) at the C-terminal domain for different nucleotide conditions. High FRET values correspond to the C-terminal closed state, and low FRET values to the C-terminal open state. The equilibrium distribution of the open and closed states was determined by a Gaussian fit. The effects of ATP analogues are shown in Fig. 10.5.

What causes these shifts in equilibrium? To answer that question I determined the dwell-time distributions of the dimerization kinetics. The FRET efficiency at the minimum between the two peaks in the FRET efficiency histograms - shown in Fig. 10.3 (dotted line) - defines the separation between open and closed states. Now each time trace is separated into parts with open and closed states (Fig. 10.1E), and the dwell times in these states are determined [48]. The distributions of these dwell times give quantitative kinetic information. Fig. 10.4 shows such integrated dwell-time distributions in the absence (green) and in the presence of ATP (black).

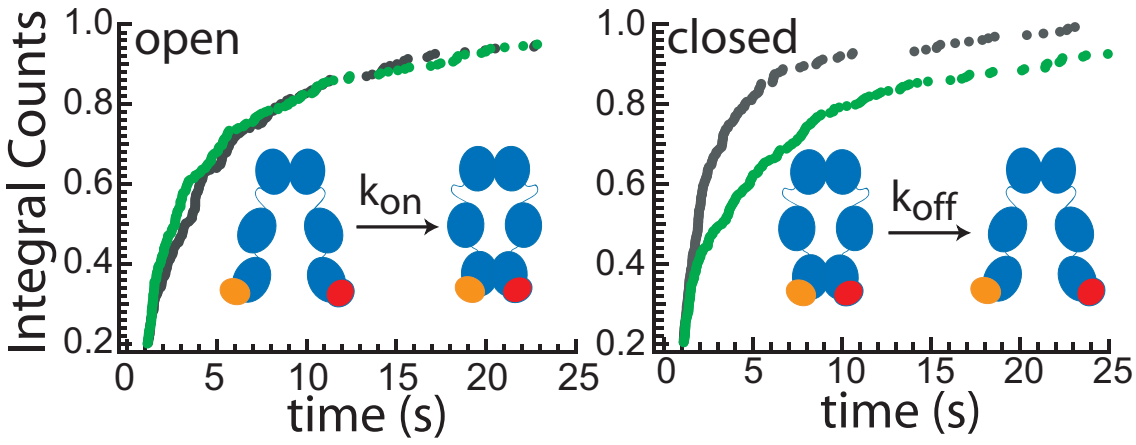

Figure 10.4.: Effect of nucleotide on C-terminal dynamics. Integrated dwell-time distributions in the open (Left) and closed (Right) states are shown in the presence of ATP (black) and in the absence of nucleotide (green). In all cases double exponential fits are necessary. The rate constants and amplitudes are listed in Fig. A.3.

Whereas the on-rate constants of the C-terminal dimerization (determined from the time in the open state) are about the same (Fig. 10.4 Left), the off-rate constants increase in the presence of ATP by more than a factor of 2 (Fig. 10.4 Right). Thus, the shift to the more open conformation is mainly caused by the destabilization of the C-terminally dimerized complex upon ATP binding and cannot be explained by a potential N-terminal induced spatial proximity (which would affect the on-rate constants). To investigate the effects of nucleotides in more detail, I used the ATP analogues ATP-γS and AMP-PNP (Fig. 10.5). ATP-γS is slowly hydrolized by Hsp90 about a factor of 7 slower than ATP [28], and AMP-PNP is not hydrolized at all on the time scale of the experiments. In the presence of ATP-γS, the obtained dwell times for the closed state are similar to those for ATP, which suggests that the hydrolysis of the nucleotide does not lead to C-terminal destabilization. This is further underlined by the at least one order of magnitude different time scales for the dimerization and hydrolysis kinetics. AMP-PNP is known to force Hsp90 into a permanently N-terminally closed state [48]; however, this is not the case for the C-terminal domains. In the presence of AMP-PNP, Hsp90 still shows C-terminal dynamics with about an equal population of the open and closed states (Fig. 10.5) similar to the situation without nucleotide, but with slightly different open and closed times. This observation shows that the C-terminal opening and closing takes place even when the N-terminal domain is fixed in the closed state.

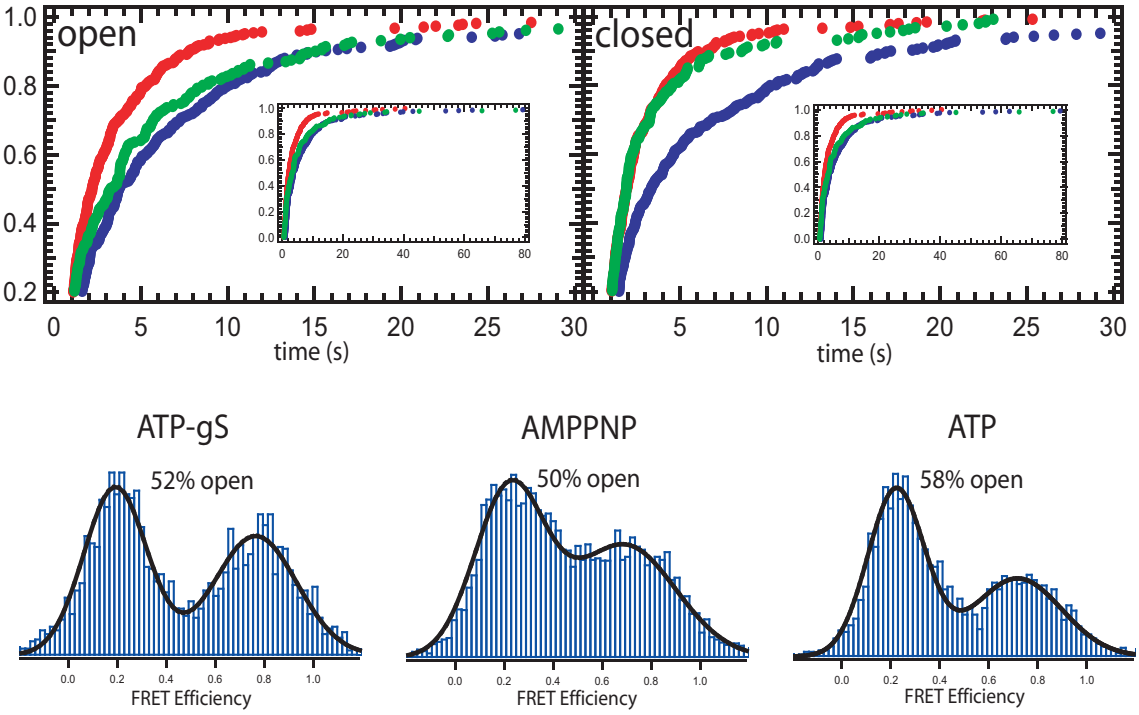

Figure 10.5.: Effect of hydrolysis on C-terminal dimerization. FRET efficiency histograms (Lower) and integrated dwell-time distributions (Upper) in the open and closed states are shown for ATP (green), ATP-γS (red), and AMP-PNP (blue). As the overlap between the two peaks for AMP-PNP is large, the separation of the open and closed states is not always unambiguous, and the open and close times for AMP-PNP should be seen only as rough estimates. The relation between the dissociation constantK_d and the relative amount of closed state α is given in the following: $K_d = \frac{[O]}{[C]}$, $\alpha = \frac{[O]}{[O]+[C]}$ [O] being the number of open molecules and [C] the number of closed molecules in equilibrium. Together these two equations give $\alpha = \frac{K_d}{K_d+1}$. Changing k_{off} and therefore K_d by a factor of 2 results in a population change from 43% to 59%. This is very close to the values I determined experimentally.

10.3. Effect of N-Terminal mutations on C-Terminal open and closed states

To address the structural basis of the observed effects, I created several N-terminal Hsp90 mutants and investigated their effects on C-terminal dimerization. I chose two mutants with deletions of either 8 (Δ8) or 24 (Δ24) amino acids at the very N-terminal end. These mutants have been characterized in the past [64, 62] . Δ8 shows

a higher ATPase rate than the wild-type protein, whereas Δ24 has no ATPase activity, because those amino acids engaged in the cross stimulation of the N-terminal domains have been removed [64]. In the third mutant, a coiled coil motif had been fused to the N-terminal end of Hsp90 to keep the N-terminal ends in close proximity (henceforth called Coil-NMC). This leads to a four times faster ATPase rate compared to the wildtype protein (Fig. A.1). The obtained FRET histograms for these mutants are shown in Fig. A.4. As can be seen in Fig. 10.6, the equilibrium of the C-terminal dimerization is shifted toward a more open state for the deletion mutants compared to the wild-type Hsp90.

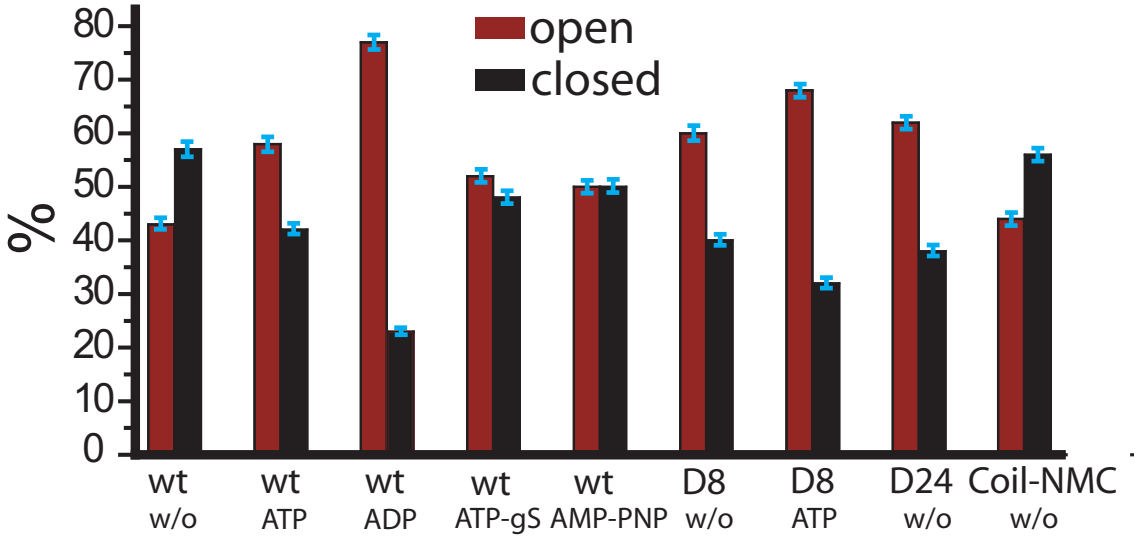

Figure 10.6.: Effect of N-terminal mutation on C-terminal dimerization. Relative amount of observed C-terminal FRET efficiencies (%) determined from the single-molecule experiments for the different nucleotide conditions and N-terminal mutations. The equilibrium distributions are shown in Fig. 10.3, Fig. 10.5 and Fig. A.4. Assuming a confidence interval corresponding to one standard deviation, the uncertainty of all values is less than 5% of their value, i.e., usually around 2.5% for the relative amount of observed FRET efficiencies.

To further understand this shift toward a more C-terminal open state, I determined the kinetics of the Δ8 and Δ24 Hsp90 deletion mutants as well as the Coil-NMC. The Δ8 and Δ24 mutants show a similar occurrence of open and closed states (Fig. 10.6) and kinetics (Fig. 10.7, red and blue) in the absence of ATP. This means that already the deletion of the first 8 amino acids destabilizes the C-terminal interaction; the deletion of 16 more amino acids does not have an additional effect in the nucleotide-free state. These two mutants have faster off-rate constants (shorter dwell times of

the closed state) than the wild type (Fig. 10.7, green), whereas the on-rate constants (equal to one over the dwell times of the open state) are quite similar to the wild type.

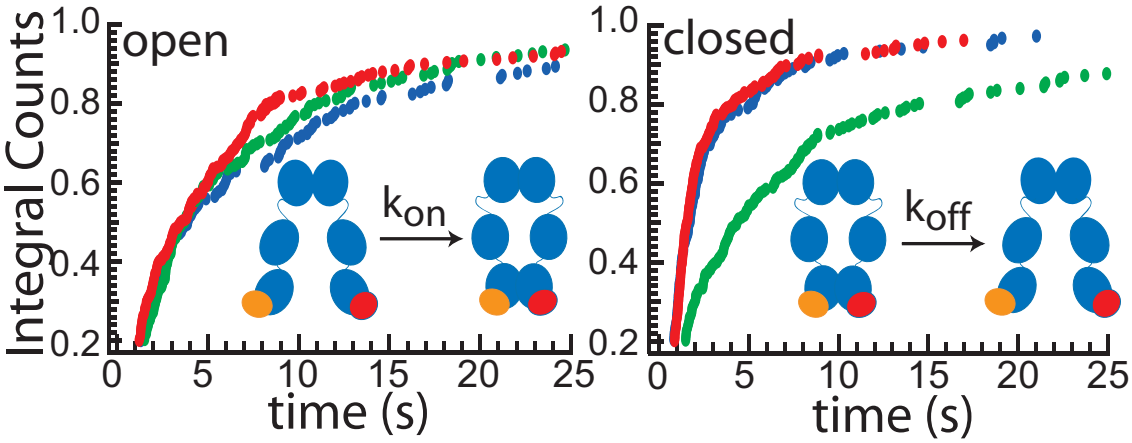

Figure 10.7.: Effect of N-terminal mutations on C-terminal dynamics. Integrated dwell-time distributions in the open (Left) and closed (Right) states are shown for the Δ8 (red), for the Δ24 (blue), and the wild-type Hsp90 (green) in the absence of ATP. Further kinetic data and fit values are shown in Fig. A.3.

It is also interesting to note that both the occurrence and the kinetics of these two mutants in the absence of nucleotides are quite similar to the wild-type protein in the presence of ATP (Fig. 10.6, Fig. A.4, Fig. 10.5). N-terminal dimerization should keep the C-terminal domains in closer proximity and therefore cause an increase in k_{on} if only geometric effects play a role. To investigate this, I compared the k_{on} values of the Δ24 mutant (which is thought to show less stable N-terminal dimerization), the wild type without ATP (which can be closed and open), and the Δ8 mutant in the presence of ATP (which is permanently closed at the N-terminal domains) (Fig. A.4). The k_{on} values are the same within the experimental uncertainty. This shows that the proximity of the N-terminal domains has little influence on C-terminal kinetics, in contrast to the nucleotide state, which has a strong effect. I tested if the N-terminal deletion and ATP binding cause the same (structural) effect at the C-terminal domain or if the observed effects are additive. Fig. 10.6 shows that both the presence of ATP and the Δ8 mutation cause a larger population of the C-terminally dissociated state, suggesting a common mechanism. On the other hand, there is still an additional effect of ATP on the Δ8 mutant, because the population is even more shifted to the C-terminally open state.

10.4. N- and C-terminal dynamics are anticorrelated

Finally, I investigated how the above-described C-terminal kinetics can explain bulk monomer exchange experiments. The bulk monomer exchange rates of yeast Hsp90 were determined in a spectrofluorimeter with the same fluorescently labeled constructs used for the single-molecule experiments and result in around one exchange per 1,000 s in the nucleotide-free state (Fig. 10.8; for a detailed description of the experiment see sec. 6.2, sec. 6.4.1 and Fig. A.5). In addition, I estimated the monomer exchange rates by kinetic simulations under the assumption that N- and C-terminal dimerization are independent, .i.e. not coordinated (Fig. A.5 shows the underlying reaction pathway). The data for the N-terminal dimerization kinetics are taken from Mickler et al. [48] and for the C-terminal dimerization kinetics from above. For determining an upper (slow) limit for the monomer exchange time from single-molecule experiments, I took the slowest rate constants, which are around 0.1 per second for both C-terminal and N-terminal opening and closing. The equilibrium constants depicted by the green and red arrows in Fig. 10.8B should be identical for uncoordinated C- and N-terminal dynamics, which makes the simulation straightforward (see sec. 6.4.1). The results for the simulation of such a scenario are depicted in Fig. 10.8A (blue and violet trace). They are clearly at least an order of magnitude faster than the bulk experimental results (green and red trace). Therefore, the rate constants for C-terminal opening are not independent from the N-terminal dimerization. The molecules stay mainly in the dimeric states; i.e. they perform many C- or N-terminal open-close cycles before dissociation (assuming two dimerization domains). In other words, the observed exchange rate constant cannot be explained by an independent movement of the N- and C-terminal ends, but necessitates cooperativity between N- and C-terminal open and closed states.

Even more, the N-terminal dimerization has to have some anticorrelation with the C-terminal dimerization, which then slows down the dissociation of the Hsp90 dimer. Middle-domain contact as a reason for the slow subunit can be excluded because middle and N-terminal domains show the same kinetics, thus moving as one (Fig. A.6).The single-molecule FRET system presented here allowed us to dissect the C-terminal open-close kinetics of Hsp90. Of particular interest is the coordination of this C-terminal kinetics with the N-terminal kinetics and particularly with nucleotide binding at the N-terminal domain. I observed a strong influence of ATP

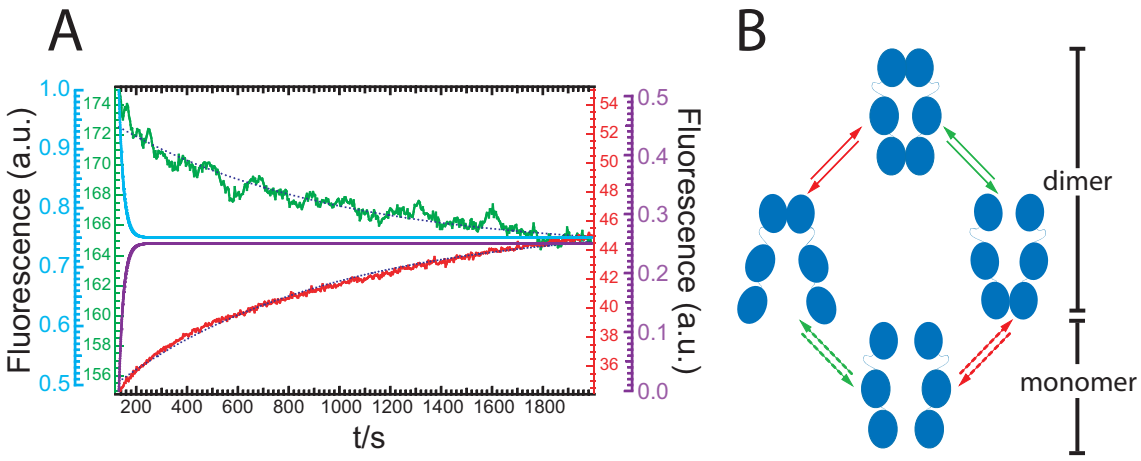

Figure 10.8.: Subunit exchange experiment. (A) After mixing of differently labeled Hsp90 homodimers in a spectrofluorimeter subunit exchange leads to an increasing FRET signal; the donor signal (green) decreases whereas the acceptor signal (red) increases in time. Blue dotted lines show global fit for both curves with $\tau = 850$ s. The violet and blue lines show the outcome of the simulation of the subunit exchange assuming no correlation between the N- and C-terminal dimerization, which results in $\tau = 18$ s. (B) Model for the N- and C-terminal opening and closing. The molecule stays mainly in the dimeric states—see main text for details. The reaction scheme for the bulk measurements and the exchange simulation are shown in Fig. A.5. .Because the concentration of the monomers does not change during the exchange process, the exchange rate should not be concentration dependent. To check this the experiment has been carried out as described at concentrations of 50 nM, 200 nM, 500 nM, and 1000 nM with Δ8Hsp90 560C .The obtained decay times for a single exponential fit were 509 s for 50 nM, 773 s for 200 nM, 476 s for 500 nM, and 585 s for 1,000 nM. The uncertainties of this bulk experiment are quite large (around 50%), but they are consistent with no pronounced concentration dependence as expected for such a reaction system.

and ADP on the C-terminal dimerization equilibrium and dynamics. The binding of ATP and ADP leads to a destabilization of the C-terminal closed state. Thus, during the ATP hydrolysis cycle, Hsp90 is successively shifted to a more C-terminally open conformation, and these three states can be aligned in a reaction cycle (Fig. 10.9) in which binding and hydrolysis of ATP facilitates the opening of the C-terminal domains. Because the C-terminal region is far away from the nucleotide binding pocket, the observed effects can be explained only by a long distance communication through the whole protein. This is in line with molecular dynamic simulations [65] where correlated changes between residues in the N- and C-terminal domains after binding of ATP or ADP were found. Experimentally, Retzlaff et al. recently

showed that point mutations at position 597 in the C-terminal domain have a pronounced effect on ATP hydrolysis [35] , i.e. a communication in exactly the opposite direction from the C- to the N-terminal domain. Similar observations were made for C-terminal deletion mutants [66]. In addition, hydrogen exchange experiments demonstrated ATP-induced conformational changes throughout the N- and middle domains in yeast Hsp90 [67] and the bacterial homologue HtpG [63]. Such a coordination between the N- and C-terminal domains is surprising because of the presence of a long flexible linker between the middle and the N-terminal domain. This linker seems to play an important role in the regulation of Hsp90 dynamics and function [68, 69]. The N-terminal deletion mutations give further insight into structural changes that cause the signaling from the N- to the C-terminal domains. The first 8 amino acids are known to intrinsically inhibit the ATPase activity of Hsp90 by an interaction with the ATPase lid of the nucleotide binding pocket [64, 62]. Their deletion should therefore abolish this inhibition and the loss of intrinsic inhibition would then be connected to the C-terminal effects observed (Fig. A.7). This notion is supported by the fact that ATP has a smaller effect on the Δ8 Hsp90 mutant than on the wild-type C-terminal dimerization equilibrium. In fact, the C-terminal dimerization equilibrium of the wild-type protein in the presence of ATP and the N-terminal deletion mutants Δ8 and Δ24 in the absence of nucleotide are almost the same (Fig. 10.6). On the other hand, there is still a detectable effect of ATP on the Δ8 mutant (Fig. 10.6). This is consistent with ATP binding and the deletion of the N-terminal 8 amino acids having a common (but not identical) impact on the C-terminal opening and closing. As both ATP and the Δ8 deletion shift Hsp90 toward the N-terminally closed state, the question arises whether keeping the N-terminal domains in close proximity results in a shift of the C-terminal dimerization equilibrium to the open state. The results obtained for the Coil-NMC construct tell us that this is not the case. Although the N-terminal domains are in close proximity in this construct, there is no effect on the C-terminal dimerization equilibrium compared to the wild-type protein without nucleotide (Fig. 10.6). Therefore, structural changes induced by ATP binding or deletion of the N-terminal segment are necessary to shift this equilibrium. There are a couple of reasons why previous methods have not revealed a C-terminal opening and closing: (i) In bulk experiments synchronization is required to follow such a movement; this has recently been applied to the N-terminal movement [28], but so far not to the C-terminal movement. (ii) In bulk experiments the dissociation is difficult to distinguish from opening, and separation of C- and

N-terminal opening is very involved (and with the published data not possible); the same holds true for published electron microscopy data. Surprisingly, the monomer exchange rates of Hsp90 are much slower than expected in the case of independent C- and N-terminal dynamics (Fig. 10.8). Thus, there must be some coordination between these two processes, which manifests in an anticorrelated opening and closing of the N- and C-terminal domains. The presence of both N-terminal and C-terminal open dimers might allow for a reinterpretation of several ensemble studies, where only N-terminally open and closed conformations were used to fit the experimental data.

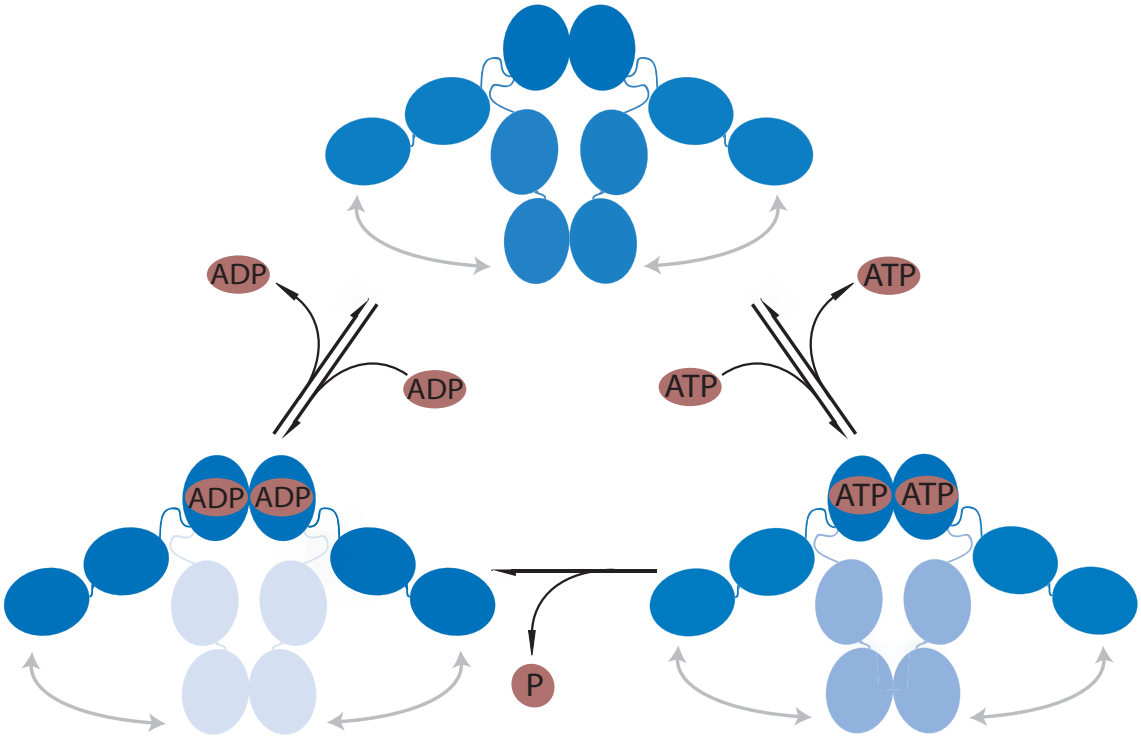

Figure 10.9.: Model for the nucleotide dependent C-terminal association and dissociation. N-terminal domains are shown as closed here. Dark blue represents high occupancy of the state, and medium and light blue represent a lower occupancy of the respective state. When ATP or ADP is bound, the equilibrium between the C-terminal open and closed states is shifted toward the open state. Additional schemes for the N-terminal mutants are shown in Fig. A.7.

11. Mechano-chemical cycle of yHsp90

Main parts of this chapter are published in [70].

11.1. Three color FRET allows the simultaneous observation of ATP binding and conformational changes

Two color FRET has revealed dynamics on the timescale of seconds on both the N- and C-terminal ends of Hsp90. The N-terminal movements are only weakly coupled to ATP turnover, whereas the C-terminal dynamics are clearly affected by nucleotide binding. Anyway the exact role of ATP in the mechanistics remains enigmatic. To get more insights into the role of ATP the simultaneous observation of ATP binding and release and conformational changes is necessary. This can be achieved by three color FRET measurements. Moreover those measurements allow to reveal the causal relation between ATP turnover and conformational changes, thus the mechanochemical cycle of yHsp90 can be observed directly.

11.2. yHsp90 binds ATP in the N-terminal open and closed state

The yHsp90 dimers were immobilized in a microfluidic chamber of a three color FRET setup as depicted in Fig. 11.1 which is analog to the one described (sec. 8.1). The N-terminal open close dynamics is detected by FRET between Atto488 and

Atto550 dyes. In addition, ATP binding was detected by FRET between the previous dyes and an Atto647N dye attached to the gamma phosphate group of the ATP via a hexane linker (Acceptor 2). The Atto647N-labeled nucleotide can be bound and hydrolyzed both with wild-type affinity and velocity by Hsp90 and does not bind to a secondary binding site (Fig. B.1, Fig. B.2). Corrected fluorescence signals are depicted in Fig. 11.1B and C, Upper. The partial fluorescence (PF) intensities are obtained from these traces by dividing the fluorescence intensities of acceptor 1 and 2 by the total fluorescence intensity, respectively (see sec. B.1). These PFs are shown in Fig. 11.1B and C, Lower, for acceptor 1 in black and acceptor 2 in blue. Fig. 11.1B shows a low acceptor 1 signal and sometimes a high acceptor 2 signal. Thus, this curve shows ATP binding in the N-terminally open state. Surprisingly, another type of curve also can be observed, which is shown in Fig. 11.1C; here, the acceptor 1 has high fluorescence with occasional decrease in fluorescence coincidental with a high acceptor 2 signal. This corresponds to binding of ATP in the N-terminally closed state. For further analysis, these PF values are plotted into two-dimensional diagrams as depicted in Fig. 11.1D . For the above-described Hsp90 system, four areas can be distinguished and assigned to the four states depicted in Fig. 11.1D. The first area (state 1) has a high relative intensity of acceptor 1 corresponding to the N-terminally closed state without nucleotide bound. The second area (state 2) with low acceptor 1 and high acceptor 2 intensity corresponds to the N-terminally closed state with nucleotide bound and is elongated because ATP has two optional binding sites (see also Fig. 11.5). The third area (state 3) with low acceptor 1 and low acceptor 2 intensity represents an open state without nucleotide bound. The fourth area (state 4) finally shows also a low intensity of acceptor 1 and intermediate intensity of acceptor 2, which corresponds to an open state with nucleotide bound.

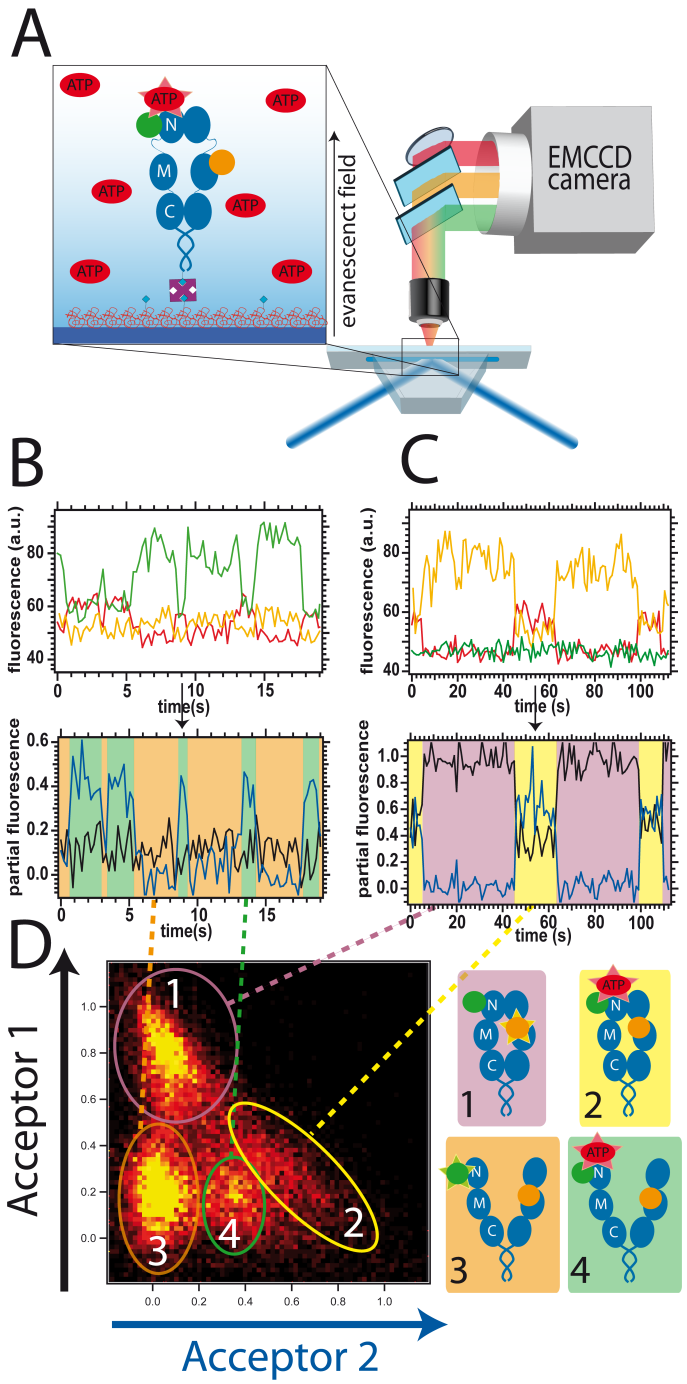

Figure 11.1.: Three color FRET setup and data analysis. (A) Hsp90 heterodimers, with the donor label (green) at position 61 of one monomer and the acceptor 1 label (orange) at position 385 of the other monomer, are fixed to the surface of a microfluidic chamber via biotin and streptavidin. ATP with the acceptor 2 label (red) at the gamma phosphate is dissolved in the buffer. The two major types of fluorescence traces are binding and unbinding in the N-terminally open (B) and closed (C) state. This leads to four states that can be separated in a two-dimensional partial intensity histogram (D).

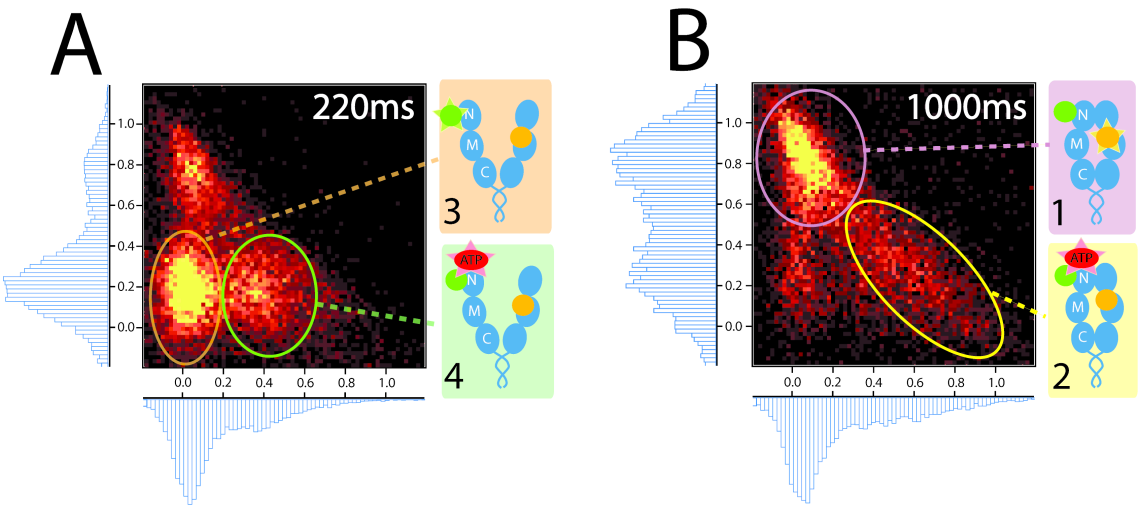

Figure 11.2.: Assignment of the different states by three-color FRET. (A) The three-color FRET histograms for ATP binding at 220-ms time resolution shows mainly the open Hsp90 with ATP bound (orange) and unbound (green). (B) At 1,000-ms time resolution (200-ms illumination every 1,000 ms), mainly the closed state with ATP bound can be observed (yellow) and unbound (purple). The states are assigned from the one-dimensional projections. The analysis of the underlying kinetics and alternating laser excitation confirm this assignment.

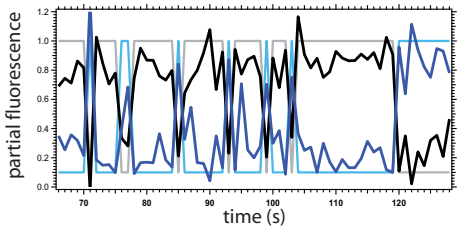

Figure 11.3.: Two PF intensities (black and blue) with the reconstructed curve from Hidden-Markov analysis (purple and light blue)

This assignment of the four states was confirmed by kinetic analysis and alternating laser excitation (ALEX) [71, 72] as detailed below. I probed the ATP binding at different time scales, namely 220 and 1,000 ms per data point, to overcome the limitations set by the finite lifetime of the fluorophores (Fig. 11.2) . At fast time scales, I mainly observe transitions between state 3 and state 4, which corresponds to binding of ATP in the open state of Hsp90. In contrast, the data measured at 1,000ms time resolution shows mainly transitions from state 1 to state 2 (namely, a binding of ATP in the N-terminally closed state). Therefore, the binding and unbinding in the closed state is slower than in the open state.Transitions in-between these types of traces are rare, but occasionally take place (see Fig. B.3 for an example). The rate constants (i.e., dwell times) are then extracted by HMM as for two color FRET [73]. This algorithm searches

underlying (hidden) states of a scattered signal and can easily be transferred to multidimensional data (see sec. 8.1.2.3 and Fig. 11.3). A measured example curve together with the reconstructed curve are shown in Fig. 11.3. The obtained dwell time distributions are plotted in cumulative histograms [74], which are corrected for bias caused by the different time resolutions (see sec. B.4 for details) and superimpose very well (Fig. 11.4A for ATP and Fig. 11.4B for ADP).

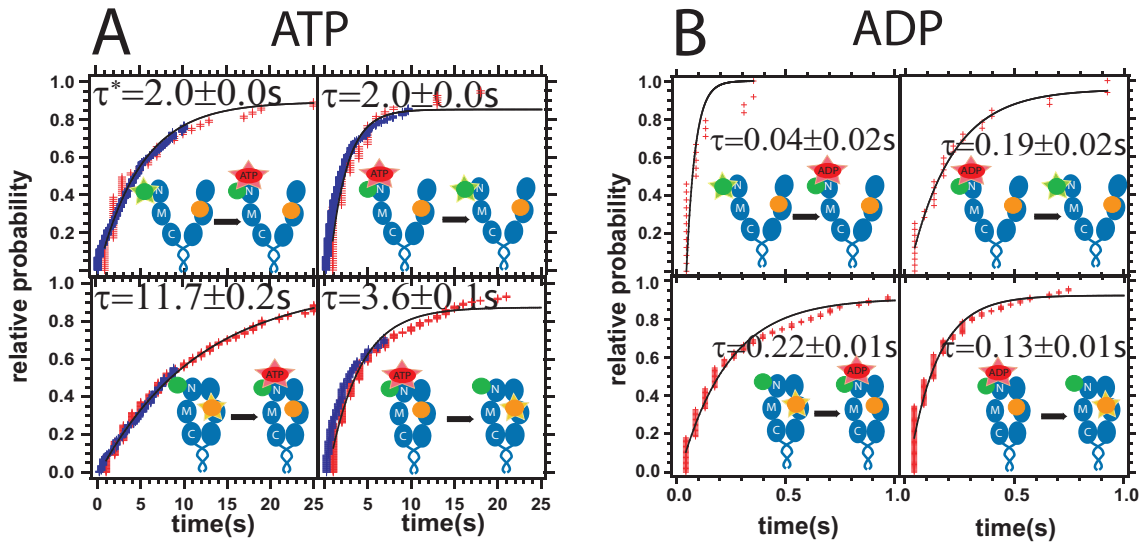

Figure 11.4.: Binding and release kinetics of ATP and ADP. (A) The binding of ATP was measured with a time resolution of 220 ms (blue) and 1,000 ms (red). The obtained dwell times were corrected for the bias caused by the different time resolutions and plotted as cumulative histograms (for details see sec. B.4); they superimpose very well. Binding and release are faster in the open state than in the closed state. The dwell time for the ATP free state (Upper Left) from the graph is 6 s, which results in a corrected dwell time of 2 s taking into account the fact that binding of ATP to the monomer not bearing the Atto488 dye does not result in a measurable signal (for details see sec. B.4). Binding and release of ADP (B) is more than 10 times faster than that of ATP, which resulted in a worse signal-to-noise ratio and therefore less good data (the rates are at the limit of the time resolution of my setups).

We find that the equilibrium dissociation constant K_d for ATP binding is little less than 1 µM for both the N-terminally open and closed states, whereas the kinetics (on- and off-rate constants) are different. After finding this unexpected ATP binding behavior, I repeated the described measurements with beta phosphate-labeled ADP . ADP binds in the open and closed states, but the binding kinetics is more than a

factor of 10 faster (Fig. 11.4 and example curves Fig. B.4). The fast off-rate constant for ADP points toward a short-lived ADP bound state *in vivo*.

11.3. The N-terminal ATP binding sites show strong negative cooperativity even in the N-terminal open state

Hsp90 is a homodimer; therefore, in principle, two identical ATP binding sites exist. On the other hand, dimerization might induce some asymmetry in the Hsp90 dimer [9]. Thus, the question arises if both binding sites can bind ATP independently or if there is some cooperativity. For the closed conformation, the answer is clear but surprising. Binding of a second ATP would result in an increase in the high acceptor 2 signal, which was never observed (>100 traces). Thus, only one ATP binds in the closed conformation. In the open state, the situation is more difficult. If an ATP binds to the monomer that does not have the donor but the acceptor 1 dye (orange), only little energy transfer from donor over acceptor 1 to acceptor 2 (ATP, red) would take place. Such a small shift of the PF can easily be overseen, because it is close to the noise level. To overcome this limitation I used alternating excitation of the donor (green) and acceptor 1 (orange) dyes and repeated the above measurements. Now, three PF intensities are obtained simultaneously: two upon donor excitation (which are the same as in Fig. 11.1 above) and one additional upon acceptor 1 excitation (showing the binding of ATP to the monomer labeled with Atto550 dye). Example curves for the ATP binding in the N-terminally closed and open states are shown in Fig. 11.5C and D and Fig. 11.5E, respectively. In Fig. 11.5C, both the acceptor 2 signal upon blue excitation (blue) and green excitation (red) increase because all three dyes are in close vicinity (i.e., Hsp90 is in the closed state during the ATP binding). In the open state of Hsp90, two types of curves are obtained: one showing ATP binding to the monomer with the Atto488 dye (Fig. 11.5E) and the other one binding to the monomer labeled with Atto550 (Fig. 11.5D). The three PF signals can be plotted in a 3D histogram. For simplification, the projections into 2D in various directions are shown and ATP binding in the closed (Fig. 11.5, Left column) and open (Fig. 11.5, Right column) state are separated.

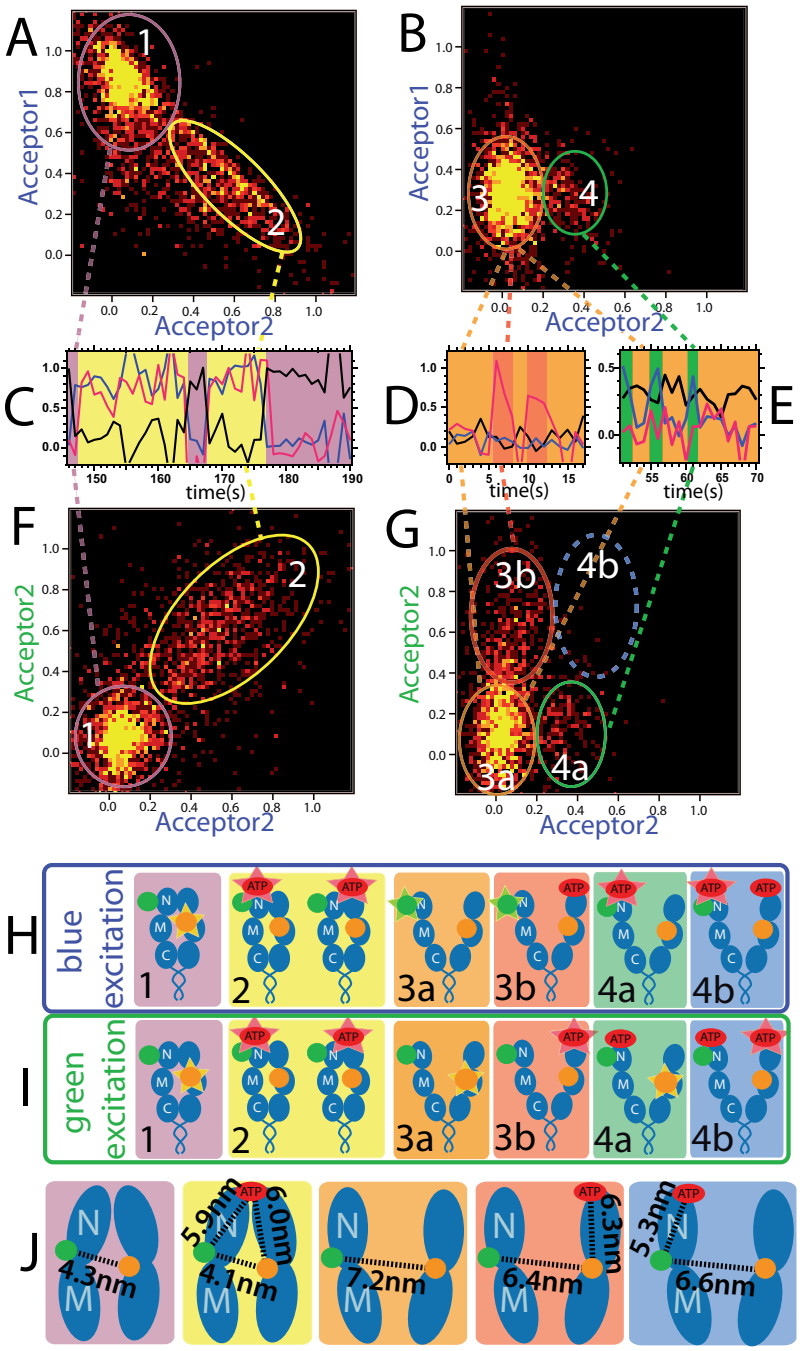

Figure 11.5.: Coordination of nucleotide binding and conformational changes. The donor and acceptor 1 dyes were alternatingly excited, which allows one to distinguish three FRET efficiencies. They can be plotted in three dimensions. Projections onto the acceptor 1–acceptor 2 (A and B) and the ALEX (acceptor 2 upon green excitation)–acceptor 2 plane (F and G) are shown. (C) Example curve for ATP binding to the N-terminally closed state (red is the acceptor 2 upon green excitation). (D and E) Example curves in the open state with ATP bound at the monomer with the green (D) and orange (E) dye, respectively. Schematics of the various states that can be distinguished upon blue (H) and green (I) excitation. (J) Calculated distances from the fluorescence intensities between the dyes.

Fig. 11.5A and B show projections onto the acceptor 1 and acceptor 2 plane. As expected, I observe the same areas, transitions, and states as in Fig. 11.1D, but now we have in addition the projection onto the ALEX (acceptor 2 upon green excitation) and acceptor 2 plane (Fig. 11.5F and G). Here, state 3 clearly separates into the two different states 3a and 3b, which could not be distinguished before without ALEX. They represent the N-terminal open state without ATP and with ATP bound to the monomer that bears the Acceptor 1 dye, respectively. On the other hand, state 4 should split into two different states (4a and 4b) if two ATPs could bind at the same time in the N-terminal open state (the center of area 4b is given by the vectorial sum of 3b and 4a, the cases where only one ATP is bound). If the two binding sites would bind ATP independently, two ATPs bound at the same time in around 6% of the time would be observed. These 6% are obtained by squaring the probability of having one ATP bound to a Hsp90 monomer (sec. B.3). This value is obtained from Hidden-Markov analysis. An error can therefore not directly be estimated, but 10% is definitely more than enough (in particular with the small errors of the fits in Fig. 11.4). The 6 % would translate into more than 100($\pm$10%) data points somewhere around the center of area 4b (for the ATP concentration of 200nM used here). From the more than 2,000 data points, only around 10 lie in the area 4b. These data points even lie at the edge of that area, which makes scattering from the other states quite likely and marks our estimate as an upper limit for the amount of double-bound ATP. It can therefore be concluded that only very rarely (or even never) two ATPs are bound at the same time in the open state (<1%) and that the N-terminal nucleotide binding sites thus show negative cooperativity. In other words, they have to communicate not only in the closed, but also in the open conformation. This in turn requires a communication through the whole protein via the C-terminal dimerization interface. Although my measurements show strong negative cooperativity, I have to mention that at higher ATP concentrations binding of two ATPs is not unlikely. The K_{d1} for the first ATP binding in the open state is around 0.2µM, whereas the K_{d2} for the binding of the second ATP is larger than 10 µM (the procedure is explained in sec. B.5). This K_{d2} has to be regarded as lower limit because the amount of data points in area 4b is an upper limit, as pointed out above.

11.4. The N-Terminus is likely more extended than given by the crystal structure

An analysis of the various fluorescence intensities allows a good estimate of the distances inbetween the dyes (this analysis is summarized in sec. B.2). From the above measurements, we have two independent measurements of the distance between donor and acceptor 1 in the closed and three independent measurements in the open state. The obtained mean distances are 4.2nm for the closed and 6.7nm for the open state, which fit well with the estimated distances from the crystal structure of 4.2nm for the closed and around 7.0nm for the open state (Protein Data Bank ID codes 2CGE and 2CG9) [3] (Fig. 11.5J) and suggest an uncertainty of around 0.5nm. Surprisingly, the four determined distances to the labeled ATP are around 6nm (Tab. B.1 and Fig. 11.5J), which is twice as much as expected (Fig. 11.6) and points toward a more extended N-terminus than given by the crystal structure. This holds true for the N-terminally open and closed states. A little larger distance could be explained by the linker between the dye and the ATP, but even if the hexane linker between dye and ATP were completely extended, this would only account for less than 1nm and not for the observed 3nm. Although still unexpected, this larger extension of the N-terminus of Hsp90 in solution is consistent with cryo-EM studies [75, 76].

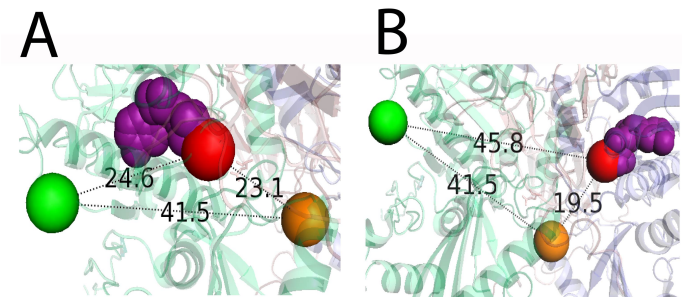

Figure 11.6.: Interdye distances according to the crystal structure in angstrom. According to the crystal structure, the distance between the ATP and the Atto488 dye on the Hsp90 is around 2.3 nm (A). The distance between the ATP and the Atto550 dye on the Hsp90 is around 4.6 nm (B). The obtained distances from the FRET measurements are between 5.3 and 6.3 nm. Thus, the N terminus is in solution much more extended than in its crystallized form.

11.5. yHsp90 does not have a successive conformational cycle but is thermally driven through a network of states

The three color single-molecule FRET setup has allowed observation of ATP and ADP binding and the underlying N-terminal conformational state of Hsp90 at the same time at the single-molecule level. Surprisingly, nucleotide binding does not cause an open-close transition of the Hsp90 N-terminus and N-terminally open or closed states are both able to bind nucleotides, although with different kinetics. Because all the transition rates of the N-terminal movement under various nucleotide conditions and the nucleotide binding under various conformational conditions have been directly measured (Tab. B.2), the whole mechanochemical cycle of Hsp90 can be reconstructed (Fig. 11.7A). Hsp90 in the absence of cochaperones and substrate proteins does not show a strict succession of states as previously assumed, but conformational transitions and nucleotide binding are driven by thermal fluctuations and therefore appear randomly. Because of this complexity, bulk measurements could not measure and assign the various rate constants to the different conformational states. They only show a mixture of all the rate constants and can therefore not accurately describe the mechanochemical cycle. In contrast, our single-molecule results can reproduce the bulk stopped-flow measurements as shown in Fig. 11.7B, without the need of any fit parameter (see sec. 6.4.2). Our data results in a K_d for ATP binding of little less than 1, both for the open and the closed states. Bulk experiments have not yet been able to measure K_d for ATP binding for the full length Hsp90, but for the isolated N-terminal domain. Interestingly, these values vary between 10µM [64] and more than 100 µM [14] and are therefore higher than for the full-length Hsp90. This hints toward the middle and C-terminal domains being essential for correct ATP binding as already supposed by Weikl et al. [21] . Furthermore, the fact that ATP binds with around the same affinity to the N-terminally open and closed conformations and thus stabilizes both conformations in the same extent explains why no shift of the N-terminal conformational equilibrium occurs upon ATP addition as shown recently [48] . Further, I find that the two ATP binding sites show negative cooperativity. This asymmetric behavior is quite surprising, but it explains several past results. Thus, only one monomer must be able to bind ATP to reach full wild-type ATPase activity, whereas the second monomer is only neces-

sary for cross-activation [9]. Moreover, recent studies show an asymmetric binding of cochaperones [77] . To facilitate this anticorrelated behavior between the two N-termini, a long-term communication throughout the whole protein is necessary; such a long-range communication was already observed within a single monomer (see chapter 10) and can now be extended to the dimer. Higher ATP concentrations are currently inaccessible with this type of single-molecule experiment; therefore, I cannot exclude that two ATPs bind at the same time at physiological ATP concentration. Nevertheless, there is no reason to believe that the anti-cooperativity disappears at higher ATP concentrations. What does the data tell us about the ATP hydrolysis? Previous studies introduced a long-lived (about 100 s) state prior to hydrolysis (also called waiting state) to get their models consistent with the slow ATPase rate. Such a state is not observed. Binding and release of ATP is much faster than the ATP hydrolysis rate; thus, ATP is bound and released several times before hydrolysis takes place. The slow ATPase rate can be explained by a high free energy barrier in between the ATP bound and hydrolyzed state. ATP hydrolysis itself is then an irreversible process, which is fast and specifically succeeded by ADP release (independent of the large conformational changes). This adds certain directionality to the - beside this - very stochastic Hsp90 dynamics. Because the hydrolysis rate is very slow compared to all other rates, Hsp90 in the absence of cochaperones and substrate proteins operates close to thermal equilibrium; occasional ATP hydrolysis only slightly shifts it out of equilibrium. The hydrolysis step itself happens in the closed state because N-terminal dimerization is necessary for ATP hydrolysis [14, 78].

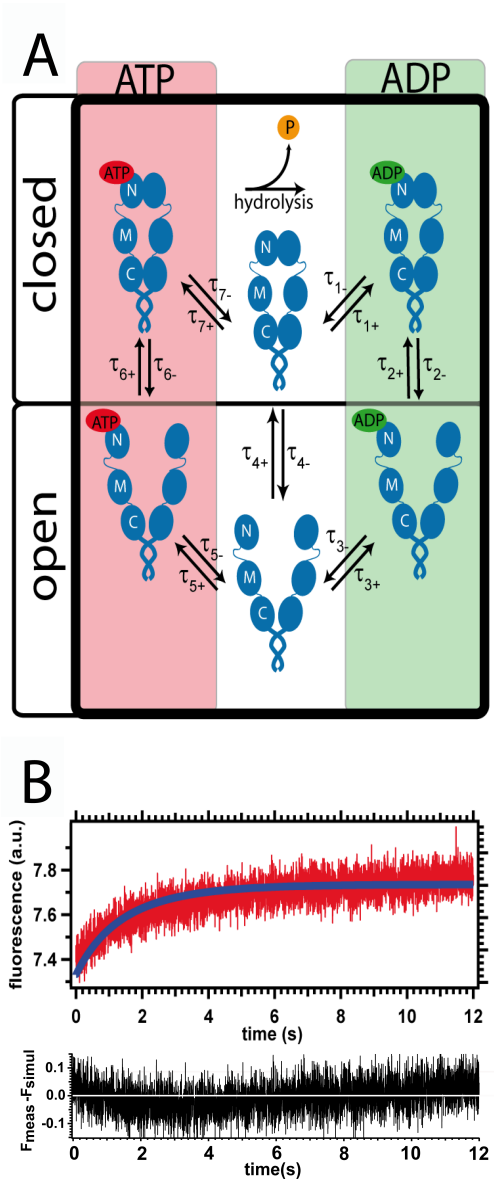

Figure 11.7.: Mechanochemical cycle of yHsp90. (A) Schematics for the mechanochemical cycle of Hsp90, where all rate constants τ_i are determined (Tab. B.2). Remarkably, yeast Hsp90 shows no stringent order of the different conformational and nucleotide states, but the transitions between the conformational states and nucleotide binding/unbinding are dominated by thermal fluctuations. The C-terminal coiled coil holds the C-terminus permanently closed, thus in the absence of the coiled coil additionally C-terminal dynamics take place. Fig. 12.1 takes also this dynamics into account. (B) Stopped-flow measurement of ATP binding (red curve) and simulation of the binding process using the rate constants obtained from the single-molecule measurements (blue curve). (Lower) The difference between the measured and the simulated curve (F_{meas} is measured fluorescence, and F_{simul} is the normalized simulated curve). As can be seen, the single-molecule rate constants reproduce the bulk stopped flow measurement very well considering that there is no fit parameter involved.

Putting my results together, one has to overcome the idea of yeast Hsp90 on its own showing a strongly directed conformational cycle, where one event is strictly followed by another event in a mechanochemical cycle. Instead, Hsp90 exists in a multitude of conformational states (Fig. 11.7), which are accessible with thermal fluctuations and might be regulated by cochaperones and substrate proteins. ATP binding plays a minor role for this regulation but might be essential for the processing of substrate proteins [79]. Such a largely stochastic picture of Hsp90 has far-reaching functional consequences. The thermally driven large conformational changes allow the Hsp90 dimer to switch between different functional states without the necessity to consume energy. This enables Hsp90 to offer a variety of different substrate binding and functional states and therefore adopt efficiently to different substrate requirements. Furthermore, it can be easily externally regulated by cochaperones or posttranslational modifications, because only little external energy is needed to shift the conformational equilibrium of the protein. I speculate that the occasional energy input by ATP hydrolysis is needed for the processing or release of cochaperone or substrate proteins.

12. Mechano-chemical cycle of bacterial Hsp90

Main parts of this chapter are published in [80].

12.1. Do all members of the Hsp90 family show the same mechanistics?

The data shown up to now have all been obtained from yeast Hsp90 (yHsp90). They show a very dynamic picture of yHsp90 with only little influence of nucleotide turnover. Anyway Hsp90 isoforms exist over a wide range of organisms. Thus the question arises if the findings of yHsp90 are true for all members of the very big Hsp90 family. As already pointed out Hsp90s are in general very homologue concerning its amino acid sequence [81], e.g. yeast Hsp90 and its bacterial homologue HtpG have homology of 36%, yeast and human Hsp90 have a homology of 61% (found by using EMBOSS Needle alignment tool). But is this homology also true for its mechanistics and function? Looking into the literature one has to doubt that. Electron microscopy, hydrogen exchange and bulk FRET measurements on the bacterial homologue HtpG let suggest that nucleotides have a big effect upon its structure [26, 82]. Thus solving the mechanism of the bacterial HtpG and compare it the eukayotic yeast Hsp90 would give a deep insight into the evolution of this protein family. To do this I repeated the experiments described for yeast Hsp90 with the bacterial homologue HtpG. The results show indeed large differences in the mechanistics of these two closely related proteins.

12.2. Nucleotides have a large impact upon the dynamics of HtpG

To investigate the conformational dynamics and the nucleotide dependence of HtpG the single molecule assay described for yHsp90 was used (sec. 8.1). Different HtpG cysteine mutants are used which have cysteines either in the N-Domain (61C), the middle domain (341C) or two cysteines within one monomer (61C, 341C) (Fig. 12.1, left); these positions are homologue to the positions 61 and 385 used in yHsp90. All the mutants have a C-terminal added coiled coil motif to keep the two monomers in close proximity [48, 49] and show wild type ATPase activity (Tab. C.1). The mutants with cysteine in different monomers are simultaneously labeled with Atto550 and Atto647N dyes and then biotinylated. The mutant with two cysteines in one monomer was also simultaneously labeled with these two dyes, then the labeled monomers were exchanged with biotinylated HtpG to get heterodimers (for detailed protocols see material and methods section). Exemplary FRET efficiency curves are shown in Fig. 12.1 (right). All the obtained FRET efficiencies for one experimental condition are collected and plotted in histograms as shown in Fig. 12.2. In those plots the different occurring conformational species can be well distinguished since the FRET signal is not averaged as in bulk measurements. All histograms in Fig. 12.2 have their main peaks at FRET efficiencies higher than 0.5, which means that HtpG stays mainly in a compact, closed state. This is a clear contrast to yHsp90, which stays more in the open state under natural nucleotide conditions [48].

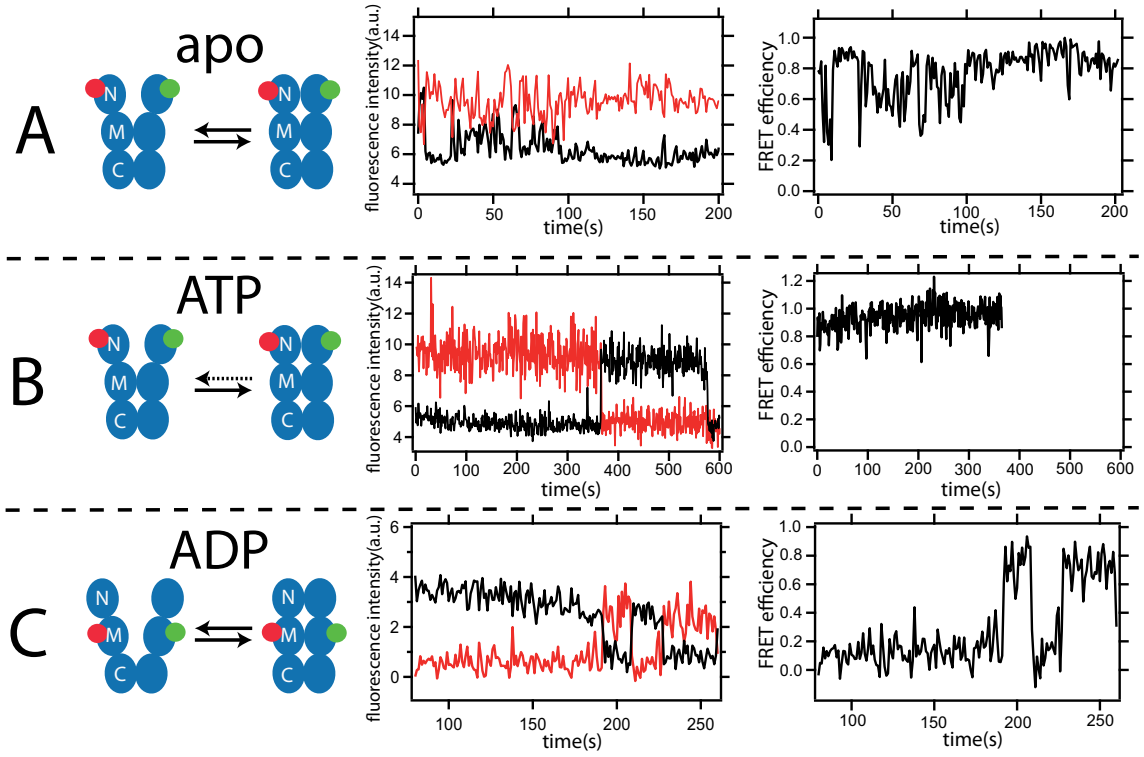

Figure 12.1.: Schematics of HtpG constructs and FRET example traces. The left side shows the position of the dyes and the conformational transitions investigated. In the middle column, the fluorescence raw data are shown (red, acceptor; black, donor), and on the right side, the obtained FRET efficiencies are depicted. (A) Without nucleotide, the N-terminal domain is wobbly without showing discrete state transitions. (B) With ATP, the N-terminal domain stays mainly in the closed state (here, for about 365s until the dye bleaches). FRET efficiencies after bleaching are not evaluated and therefore not shown. (C) With ADP, the M-domain shows quite slow transitions between a discrete open state and a closed state. See Fig. 12.2 for a full account of all combinations of nucleotide conditions and domains.

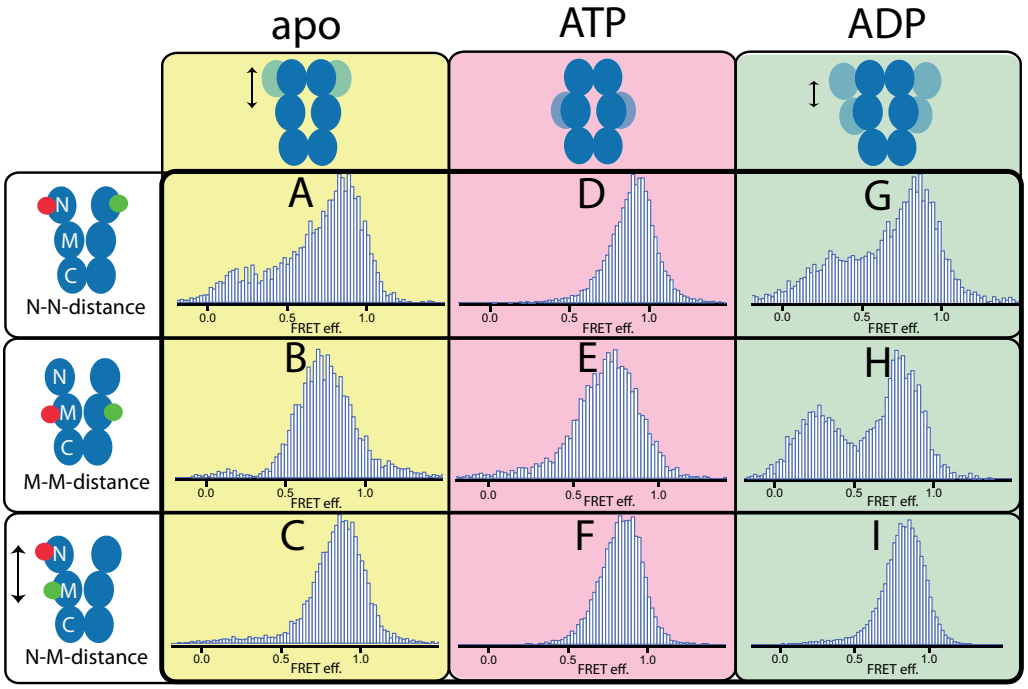

Figure 12.2.: Conformational changes of HtpG domains upon addition of nucleotides. Histograms of the FRET efficiencies for the various constructs and nucleotide conditions are depicted. The y-axes show relative numbers (normalized to an integral of 1), and the x-axes show the FRET efficiencies. (A–C) Without nucleotide, the N-domain is very flexible showing no discrete state transitions, whereas the middle domains are mainly closed. (D–F) With ATP, both dimers are quite close together and the monomers are very stiff, whereas with ADP (G–I), two clear states (one open and one closed) exist. The schemes on the upper row show the underlying conformational states. Dark blue is highly occupied and light blue is rarely occupied. The number of data points in each graph ranges from more than 4000 (N=32 molecules) (A) to almost 17,000 (N=98 molecules) (I).

In the absence of nucleotide, the N-terminal domain is more or less continuously moving (Fig. 12.1A), without staying in the otherwise defined open or closed state. This leads to FRET values over the whole range in the corresponding FRET histogram (Fig. 12.2A). In contrast, the middle domains are mainly closed with rare opening events (Fig. 12.2B). The dynamics between the N-terminal and the middle domain within one monomer (Fig. 12.2C) is less pronounced. It is mainly fixed (no large movement in between the domains), but nevertheless more flexible than with nucleotide (Fig. 12.2F,I), which can be seen from the larger width of the peak. Altogether, in the absence of nucleotide the N-domain shows large conformational

fluctuations, whereas the middle domain stays mainly in a closed state. In the presence of 2mM ATP, the situation changes considerably, the N- and M-domains are now in essence permanently closed (Fig. 12.1B, Fig. 12.2D) and the monomer chains become very rigid. This can be seen by the one sharp high FRET peak for the N-N domain distance (Fig. 12.2D) as well as for the N-M intra-monomer distance (Fig. 12.2F). Surprisingly, the middle domain shows a few opening events, which can be seen on the "tail" of lower FRET efficiencies in Fig. 12.2E (for an example curve see Fig. C.2). Thus a rare "O-like" form of HtpG exists in the presence of ATP. Altogether, ATP leads to a mainly closed conformation, with occasional flexibility in the middle domain. In the presence of 2mM ADP binding again conformational dynamics can be observed. In contrast to the situation without nucleotide, well defined conformational states can be found - mainly one open and one closed state. Rarely a third state with a FRET efficiency of around 0.5 can be observed (an example curve is shown in Fig. C.2). Furthermore conformational transitions between the two major populated states occur (Fig. 12.1C). These transitions are very slow for proteins: the dwell times are around 25s and even more . Thus only a very small amount of dwell times could be extracted and I have to restrict myself to a qualitative discussion of the kinetics in the presence of ADP. The energy barrier that separates those states has to be much larger than the thermal energy. In contrast to the situation in the absence of nucleotide, the conformational changes are not limited to the N-terminal domain but the N- and M- domain seem to move together. This can be seen by the fact, that the FRET histograms for both domains (Fig. 12.2G and H) show two states approximately equally distributed and also the obtained FRET time traces for both processes show long dwell times (Fig. 12.1C and Fig. C.3) . These data already allow to predict a reaction cycle for HtpG. In the nucleotide-free state random (thermally driven) movement of the N-domain occurs (there is no other energy source present), whereas the M-domain is mainly closed. After addition of ATP, HtpG is fixed into an overall closed and rigid state. In the presence of ADP (i.e. after hydrolysis) HtpG can slowly switch between defined open and closed states. On top of that, the FRET histograms allow to estimate the distances between the dyes. These values should only be taken as estimates since several factors impact the exact conversion from FRET efficiencies to distances - as already mentioned [83]. Nevertheless, relative distance changes are generally reliable and distances determined by FRET have been self-consistent and in good agreement with crystal structures in the past [3]. The obtained distances for HtpG are given

in Tab. C.2. The distance in between the dyes at the N-termini in the closed state is 4.9 nm without nucleotide and in the presence of ADP, whereas after ATP binding it is round 4.3 nm and thus more compact. Without nucleotide the FRET efficiency values reach down to something like 0.2 which corresponds to a distance of 8nm. An extremely extended structure as described recently [84] would result in zero FRET efficiency. If at all, such a widely open structure only rarely exists (Fig. 12.2A shows a few data points around zero FRET efficiency) and can therefore be neglected in the following. The closed state of the middle domain shows a distance of something like 5.5nm between the cysteines at position 341, while the cysteines at the C-terminal position 521 are about 5.2 nm separated.

12.3. HtpG is driven by a mechanical ratchet mechanism

How does ATP binding and hydrolysis drive these conformational changes? In general two major types are possible, either ATP binds to the open state of HtpG and forces it into the closed state or HtpG moves into the closed state by thermal fluctuation where ATP binds and fixes HtpG in its closed state. The first model is often referred to as power stroke, the second as mechanical ratchet. In order to gain more information about the underlying mechanisms of HtpG I performed three color FRET measurements with 1 µM labeled ATP, similar to those described for yHsp90 in chapter 11. The HtpG was labeled at position 61 with Atto488 on one monomer and with Atto550 on the other monomer. The ATP was labeled at the position via a C-6 linker with Atto647N. The labeled ATP is hydrolyzed by HtpG 61C with wild type activity (Fig. C.4). A schematic representation can be seen in Fig. 12.3C (right). These measurements show at the same time the conformational and nucleotide binding dynamics of HtpG . Furthermore they give the causal order of reaction steps. From the three fluorescence intensities (Fig. 12.3A) two partial efficiencies are obtained, which are represented in two dimensional FRET histograms (Fig. 12.3C). The fluorescence traces are selected by a threshold criterion in the Atto647N detection channel (which reflects ATP binding) and subsequent manual inspection.

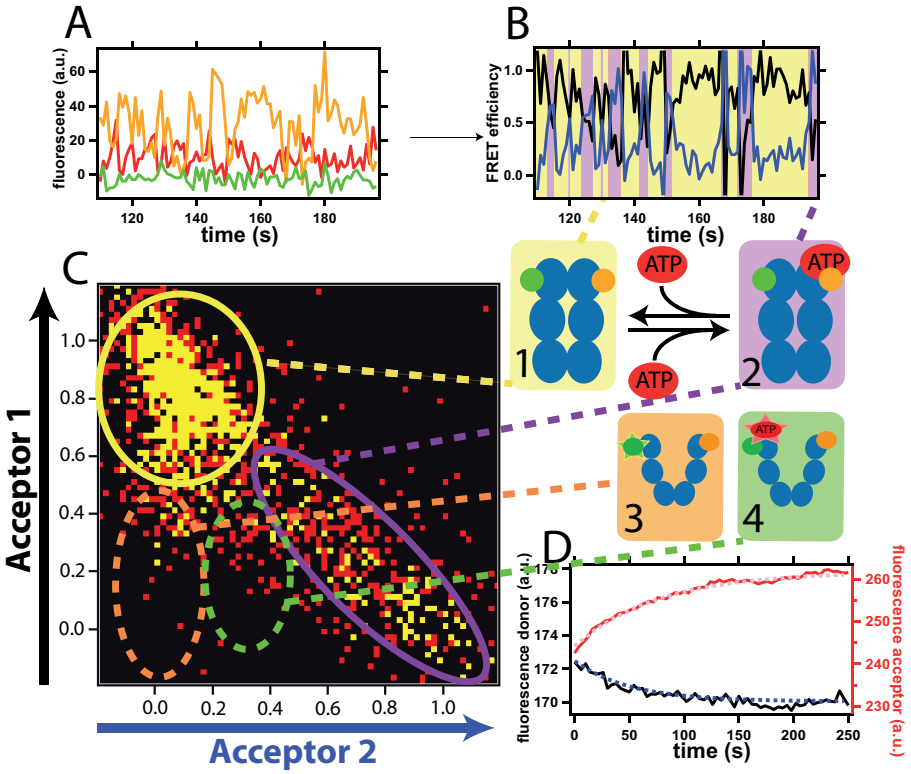

Figure 12.3.: Coordination between ATP binding and the open–close kinetics of HtpG. (A) Fluorescence signal versus time for a three-color FRET curve (green is Atto488 attached to one HtpG monomer at position 61C, orange is Atto550 attached to the other HtpG monomer at position 61C, and red is Atto647N attached to the ATP). The three fluorescence signals are converted into two partial fluorescence signals (B) by dividing the acceptor 1 (black) and the acceptor 2 (blue) signals by the total signal. Two types of binding curves can be observed, a fast binding and release dynamics (B) and a quite stable binding of ATP (Fig. C.7). The partial fluorescence intensities are plotted in 2D histograms (C) where the closed state without (1, yellow) and with (2, magenta) ATP bound can be separated (red square is one data point, and yellow is two or more data points for that pixel; the overall number of data points is 2000 from N=20 molecules). The green/brown broken circles indicate where the open state with/without ATP would occur (see chapter 11 and Fig. 11.1). The boxes with the Hsp90 schematics show the different possible states. The underlying colors also mark the position of every state in the 2D histogram (D) and in the example curve (B). (D) Bulk measurements of fluorescence labeled ATP (acceptor, red trace) binding to HtpG (donor, black trace). The broken lines are a global fit of the data with a time constant of 70±27s (the error was estimated from three independent measurements). This slow binding process occurs because HtpG has to move into the N-terminal closed state before ATP can bind.

The first finding is that more than a factor of 10 less HtpG dimers on the surface show ATP binding compared to yHsp90, which already hints towards not all conformational states being binding competent. Indeed only single molecule traces similar to the example Fig. 12.3A,B could be obtained. The high acceptor 1 signal (black) in between the binding events in Fig. 12.3B clearly shows that ATP binding (high acceptor 2 signal, blue) takes place only in the closed state . These curves result in two peaks in the 2D histograms for the closed state without (yellow) and with (cyan) ATP (Fig. 12.3C). The position and shape of the peaks is equal to those obtained for yHsp90 (see Fig. 11.1). Binding of ATP in the open state could never be observed (among >5000 observed molecules). The open states would occur at the bottom left of the 2D histogram. In the case of yHsp90 the open apo state was within the orange dashed circle and the open ATP bound state in the green dashed circle (Fig. 11.1). There is no significant number of data points for HtpG. Therefore, HtpG binds ATP only in the N-terminally closed state and has to convert into the closed binding competent state before ATP binding can take place. I cannot exclude occasional binding of ATP to the open state at very high ATP concentration, but this is irrelevant for the mechano-chemical cycle as the affinity is at least three orders of magnitude lower and therefore negligible compared to the binding in the N-terminal closed state. My data excludes models where ATP bound to the N-terminal open state forces HtpG into the closed state (see sec. 12.5 for more details). Thus the large conformational changes of HtpG are caused by a ratchet mechanism not a power stroke. Fig. 12.3D shows bulk measurements of the ATP binding with 1µM labeled HtpG and 10µM labeled ATP. The obtained curve shows an effective binding rate which is around 1/70s. To exclude artifacts caused by fluorophore physics, the measurements were repeated with unlabeled HtpG and labeled ATP, as well as with labeled HtpG and unlabeled ATP (same concentrations as above). Both controls did not lead to any signal change (Fig. C.5). The effective binding rate (≈1/70s) is far slower than ATP binding to the closed state itself (≈1/5s) as can be seen in Fig. 12.3 A,B. Thus ATP binding is - as predicted by my ratchet mechanism and discussed in detail below - limited by the transition into the closed binding competent state (with a rate of 1/70s).

12.4. The C-terminal dimerization site is not influenced by nucleotides

For yHsp90, I found a C-terminal opening and closing at the time scale of seconds beside the N-terminal conformational changes. The open-close equilibrium was regulated by nucleotide binding at the N-terminus, demonstrating a N-C-terminal communication in yHsp90. To check if similar effects can be found in HtpG I used a HtpG mutant without coiled coil and a cysteine in the C-terminal domain (521C) - this mutant also showed wild type ATPase rate (Tab. C.1). The HtpG mutant was labeled and encapsulated in lipid vesicles as described before for yHsp90 (sec. 5.1, sec. 7.2.2).

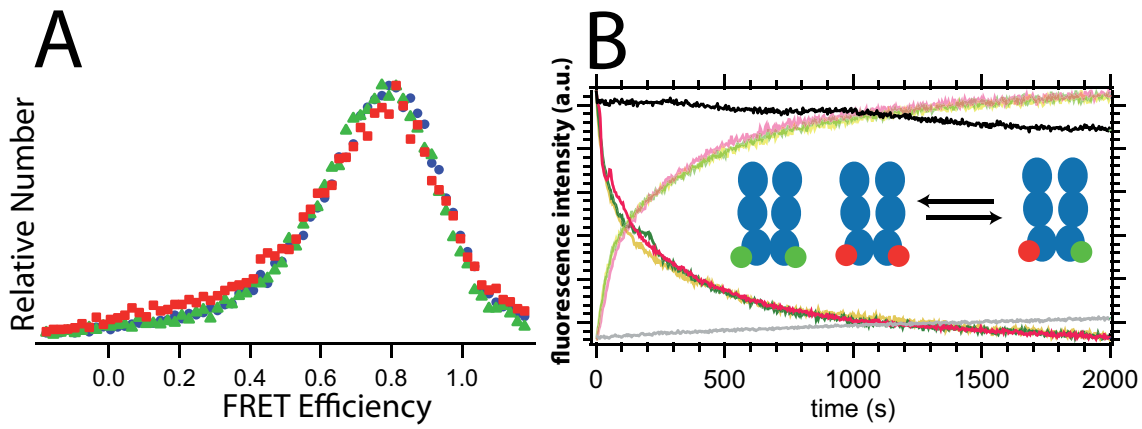

Figure 12.4.: Stability of the C-terminal dimerization for HtpG. (A) Single molecule data show that the C-terminal domain is mainly closed (high FRET efficiency around 0.8) with rare opening events. No significant effect of nucleotides can be seen. Blue circles, ADP (total of 22,000 data points); red squares, ATP (total of 13,000 data points); green triangles, no nucleotide (total of 10,000 data points). (B) Bulk measurements show no effect of natural nucleotides on monomer exchange (dark curves are donor signal and bright curves are acceptor signal; yellow is without nucleotide, red is with 2mM ADP, and green is with 2mM ATP). Therefore, the N-terminal conformation is not relevant for C-terminal dimerization stability. Only the unnatural nucleotide AMP-PNP (2mM) leads to a significant slowdown of the exchange rate (black).

A shows the FRET histograms for the C-terminal domain under various nucleotide conditions. The C-terminus is not affected by nucleotides and stays mainly in the closed state whereas the protein can be rarely found in the open state (some values can be seen at lower FRET efficiencies in Fig. 12.4). This is in contrast to the

situation in yHsp90 where rich C-terminal dynamics on the timescale of seconds was found. Moreover, in yHsp90 I found that the N- and C-terminal dynamics are anti-correlated resulting in a slow monomer exchange , namely with a time constant of around 1000s, despite opening rates at the N- and C-terminus in the range of a few seconds. To test if similar effects can be found for HtpG I performed monomer exchange experiments by mixing two differently labeled HtpG species and measured the FRET signal upon formation of heterodimers (Fig. 12.4B) as described (sec. 6.2). For HtpG the effective mean exchange time is around Fig. 12.4 (for details see supplemental text) and thus faster than in the case of yHsp90, although the C-terminal dimerization is stronger. I repeated the measurement with 10times lower concentration to exclude that the measurement is diffusion limited and indeed found the same result (Fig. C.6). Only the non-natural nucleotide AMP-PNP led to a strong slowdown of the exchange rate. In summary and in contrast to yHsp90, no effect of natural nucleotides could be found on the C-terminal dynamics. Furthermore, the N-terminal dimerization state (which is changed by nucleotides) does not influence the exchange rate, which means that even complete N-terminal closing (for example in the presence of ATP) does not alter the exchange rate. Thus no N-C communication of the type found in yHsp90 exists in HtpG.

12.5. Evolution of Hsp90: From mechanical ratchet to thermal fluctuations

As mentioned above, HtpG is driven by a ratchet mechanism, while yHsp90 is dominated by thermal fluctuations, which sheds a new light on the evolution of this important heat shock protein. Fig. 12.1 and Fig. 12.2 show that HtpG is very flexible (and occupies many states) in the N-domain without nucleotide and becomes rigidly closed upon binding of ATP. In the presence of ADP a very slow thermally driven transition between a well defined open and a closed state can be found. These results are consistent with HD exchange data, where high flexibility was observed in the nucleotide-free state and significant stabilization in the presence of ATP, especially in the N-domain [82]. The kinetics of the HtpG mechano-chemical cycle is further dissected with my three color FRET experiments (Fig. 12.3). A schematics of this cycle is depicted in Fig. 12.5A. and the corresponding energy landscapes is schematized in Fig. 12.5C and D. The apo HtpG (no nucleotide) has to reach the

closed state via thermal fluctuation (1→2) in order to be able to bind ATP (2→3). At physiological ATP concentration, the binding of ATP (2→3) is then much faster than the N-terminal opening (2→1) and HtpG therefore stays mainly in the closed state. Some of the ATP is then fixed and committed for hydrolysis (3→4). This step is then rate limiting for the steady state ATPase and the similarity of the time scales between the ATPase and the closing is coincidence. The amount of committed ATP was determined to be around 15 % from HD exchange data [82]. Such a committed state would require the occasional transition from weakly bound ATP to strongly bound ATP, which then awaits slow hydrolysis - indeed, I observe the occasional long bindings of ATP in my FRET assay (Fig. C.2 for an example). Finally, HtpG is left in the ADP-bound state (4, 5), where the N and M domains move together and thus a kind of hinge exists between the C and M domain. Indeed an increase of flexibility upon ADP binding could also be found by HD exchange [82]. In summary, the system proceeds in an ordinal cycle through the states 2, 3 and 4. The rate constants can here only be given as rough estimates since either no discrete transitions (apo state) or too few transitions (ADP state, ATP binding) could be observed for a quantitative analytics. Nevertheless, at least the order of magnitude of the temporal transitions can be given here. ATP binding in the open state with subsequent fast closure, altogether taking less than 100ms (the time resolution of my setup) can also be excluded. In this case I should observe single molecule traces where a closed state with bound ATP follows an ATP free open state, which I never observed. This cycle is in strong contrast to the situation in yHsp90, where nucleotides can bind in the open and closed state without directing large conformational changes. Thus, yHsp90 does not show an ordinal reaction cycle but the protein mainly diffuses through a network of states in random order (Fig. 12.5B). Another striking difference between HtpG and yHsp90 can be found in its different properties concerning the C-terminal domain. In HtpG the C-terminal domain is mainly closed and unaffected by nucleotide binding at the N-terminus, whereas in yHsp90 C-terminal dynamics was found that is influenced by nucleotide binding. Such dynamics require N-C communication in yHsp90 causing anti-correlated N and C-terminal movement. Consequently, yHsp90 dissociates very slowly ($\tau \approx 1000$s) despite the fact that N and C-terminal ends open frequently. HtpG dissociates considerably faster, even in the ATP bound (N-terminal closed) state. This suggests that the N-termini are not entangled in the natural cycle - only with AMP-PNP the dissociation is strongly reduced, pointing towards an entangled

state similar to the crystal structure of yHsp90 with AMP-PNP. In the Tab. C.2 I compare the obtained values for the distances in between various amino acids in view of the yHsp90 crystal structure in the presence of AMP-PNP and Sba1 [3]. The distance between the N-terminal cysteine in the yHsp90 crystal structure is 7.1 nm and thus bigger than the measured values for HtpG (4.3 nm). That means that the N-terminal domain seems to be differently oriented than in the yHsp90 crystal. In my opinion this can only be explained by some kind of N-terminal rotation compared to the yHsp90 crystal structure. On the other hand the distance for the middle domain at position 341C is 2.4 nm in the yHsp90 crystal and thus HtpG is more extended or also rotated in the middle domain. The C-terminal cysteines in yHsp90 have a distance of around 4.7 nm in good agreement with the measured values. Taken together the C-terminal orientation seems to be similar in HtpG and yHsp90, whereas the M and N-domain are differently oriented in HtpG compared to the AMP-PNP bound yHsp90. Comparison with HtpG structures from the Agard group are given in Tab. C.2.

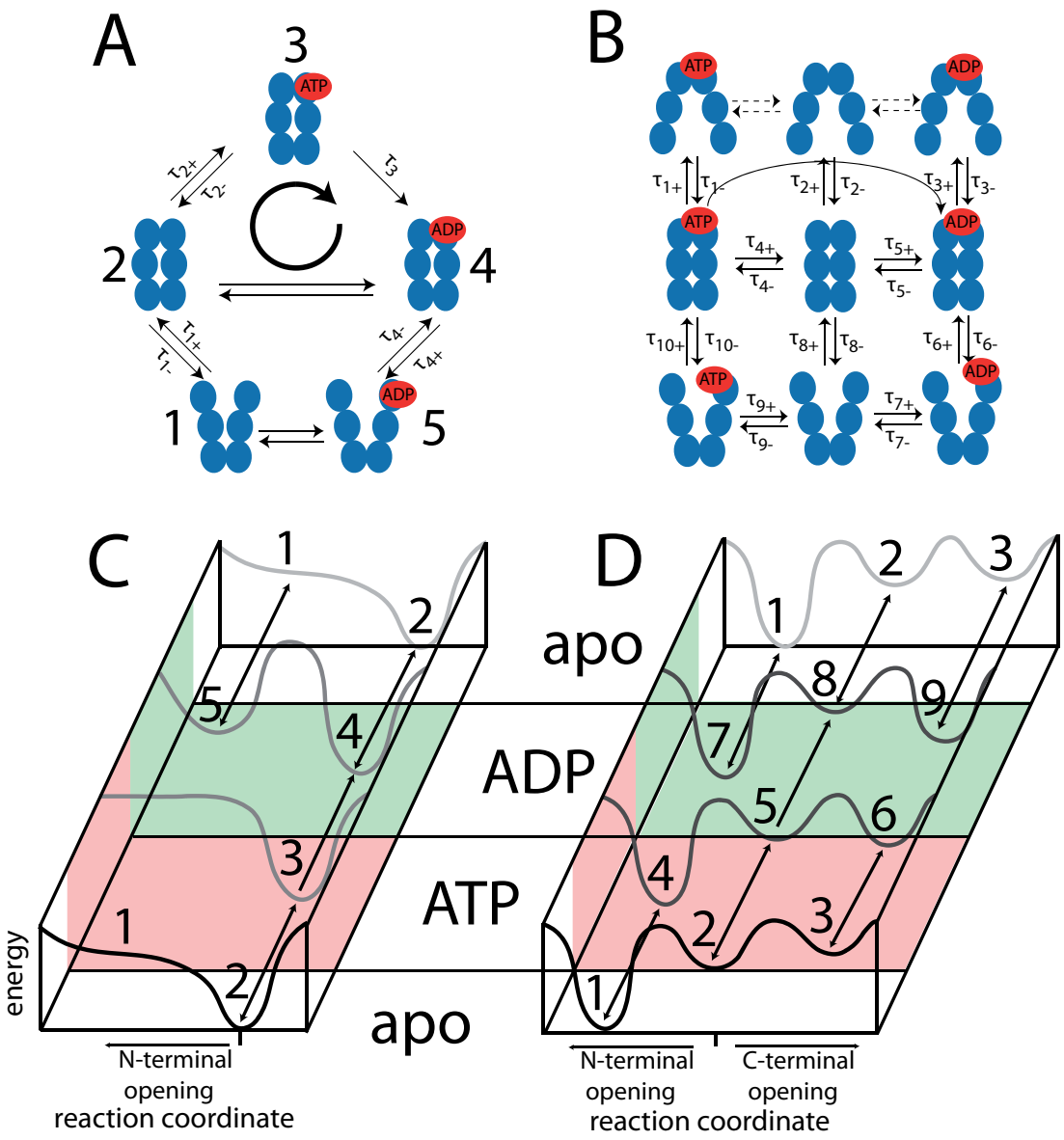

Figure 12.5.: Comparison and evolution of HtpG and yHsp90 reaction cycles. (A) ATP causes the closure of HtpG by a mechanical ratchet mechanism. ATP binds after N-domain closure and fixes this state (2→3). Thus, the system proceeds in ordinal succession through the states 2, 3, and 4. The C-terminal domains are mainly closed. (B) In contrast for yHsp90, no successive reaction cycle exists. The protein diffuses in random order through a network of states including N- and C-terminal opening and closing. Nucleotide turnover changes the energy landscape of HtpG significantly (C), whereas in yHsp90 only the C-terminus is affected by nucleotides (D). The rates are given in Tab. C.3.

What could be the advantage of the observed increased flexibility and only marginal

control by nucleotides for yHsp90 compared to HtpG? First, a flexible protein can adapt to different types of substrate with greater ease than a rigid one. This might be important since the amount of different proteins which have to be protected from aggregation upon heat shock are bigger for yeast Hsp90 compared to HtpG [85, 86, 87, 88]. Second, HtpG was recently shown to wrap around a substrate [86]. Such an "enclosing" of substrates could be much easier for the more flexible yHsp90. Third, more flexible chaperones (i.e. proteins with shallow energy barriers) can be much easier controlled by cochaperones. Since the different conformational states are separated by only shallow energy barriers also small binding energies are sufficient to significantly shift the conformational equilibrium. This might on the one hand explain why no cochaperones for HtpG are known whereas a large number of those proteins is known for yHsp90. On the other hand it also explains why also cochaperones with very little binding energies such as Aha1 or Sba1 (both have dissociation constants in the lower µM range [89, 90]) are able to control the conformation of yHsp90. What might in this context be the advantage of the more pronounced C-terminal dynamics in yHsp90 compared to HtpG? My data allows to speculate that the additional C-terminal opening in yHsp90 effectively increases the accessible surface of the protein, providing more possibilities for client binding. Furthermore it allows the substrate to enter from two sides the inner part of the protein, which is thought to be the client binding region. Thus C-terminal opening increases the modes of substrate binding and might allow processing a greater variety of clients. Finally, the anti-correlated movement in between the N- and C-terminus hinders yHsp90 from falling apart despite the high flexibility. This is very important, because monomers are not functional *in vivo* [49]. Thus this anti-correlation effectively increases the amount of dimer and thus the overall chaperoning efficiency in the cell. The remaining question why did the obvious evolution from a nucleotide regulated ordered mechanism towards a random fluctuating network of states takes place? Why had the controlled mechanism of HtpG to be replaced by the random fluctuation of yHsp90? As I already pointed out above the number as well as the size of the proteins in the cell increased from bacteria to yeast. Therefore a more effective chaperoning might be necessary. On the other hand also the cellular role of Hsp90 seems to have changed from bacteria to yeast. Thus a knock-out of HtpG is still viable but a knockout of yHsp90 is lethal. Also a lot of the known yHsp90 substrates are involved in cell regulation and signal transduction. Thus in eukaryotic cells Hsp90 gets a more important role in the cellular processes, which maybe

made an evolution towards a more sophisticated chaperone system necessary. In summary, I observe a clear change in protein mechanism between the prokaryotic HtpG and the eukaryotic yHsp90: yHsp90 has a higher N-terminal flexibility, a new C-terminal dynamics and an anti-correlation between N- and C-terminal dynamics to increase at the same time its potential to bind various substrate proteins and stay in its functional dimeric form. Although I do not know which evolutionary pressure lead to this type of change in the protein mechanism, my findings show that noisy systems, which have smaller energetic differences in between their conformational states can be favorable since they can adopt much better to changing tasks and show a greater functionality.

13. Molecular crowding changes the dynamics of yHsp90

Main parts of this chapter are published in [91].

13.1. Molecular crowding changes the yHsp90 kinetics, but not the equilibrium

The mechanochemical cycle of yHsp90 was measured *in vitro*, that means in buffer solution without any other proteins. Of course the situation in the living cell is massively different. Here a large number of proteins is diffusing in the cytosol which leads to an strong decrease in viscosity and slows down the diffusion of many proteins. In addition those proteins can unspecifically interact with each other. These effects are often summed up with the term "molecular crowding" [92, 93]. Thus the question arises if the dynamics of yHsp90 are different in the cell, that means under molecular crowding conditions. To simulate molecular crowding conditions the N-terminal dynamics of yHsp90 were observed in the presence of 0.5mg/mL bovine serum albumin (BSA). As described in chapter 11 the open/close transition rates decrease massively. But also the shape of the curves changes. The FRET plateaus become less stable and new "distance intermediates" can be found (Fig. 13.1). Moreover the transitions between N-terminally open and closed - which are normally much faster than the time resolution of the measurements - become slower and thus less distinct. Interestingly the open/closed equilibrium of yHsp90 does not change drastically. Thus molecular crowding primarily effects the kinetics not the equilibrium. After flushing out the BSA with pluronic F127 (BASF) fast and distinct transitions can be again measured (Fig. 13.1 D). Interestingly the ATPase rate is not influenced by BSA (Fig. B.5), which again shows that the ATP turnover is not strictly coupled to the open and closing movement of Hsp90. This effect of molecular crowding

underlines the flexibility of yHsp90. Already quite moderate changes in the environment lead to changes in yHsp90s dynamics as supposed by the high conformational flexibility of yHsp90 described in the last chapters.

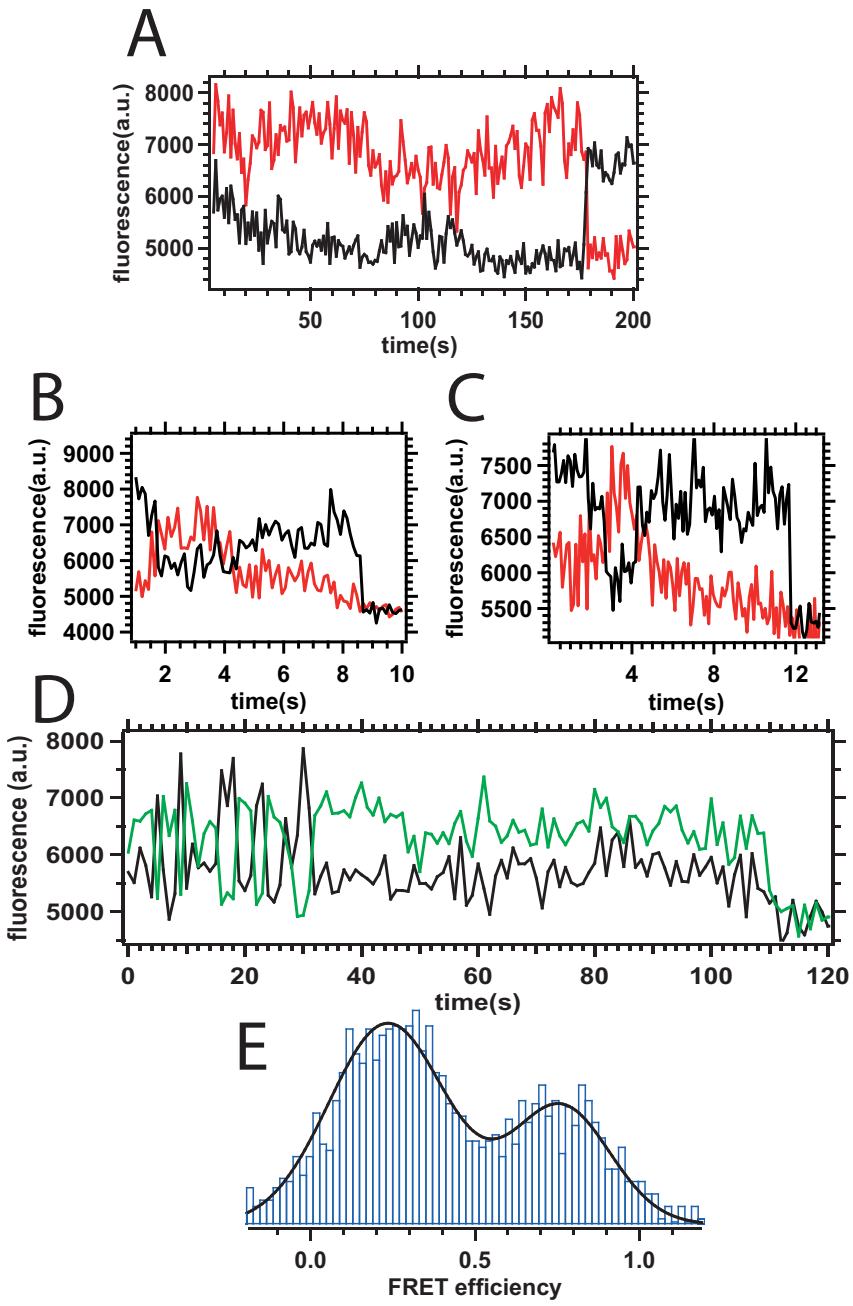

Figure 13.1.: Effect of BSA on the Hsp90 dynamics. (A–D) FRET curve of a Hsp90 heterodimer labeled with Atto550 at position 61 and Atto647N at position 385 with 0.5 mg/mL BSA. Addition of BSA leads to a slowdown of the open closing dynamics of the Hsp90 N-terminus.(A) shows a molecule that stays in the open state, but at around 100 s a half-closing of the dimer can be observed.(B) and (C) show smooth transitions in contrast to the sharp transitions obtained for ATP binding Fig. 11.1. Removal of the BSA with a 1% pluronic solution leads to a recovery of the original N-terminal transitions (D); here, the Hsp90 61C is labeled with Atto488 and the Hsp90 385C is labeled with Atto550. The addition of BSA has no significant effect upon the equilibrium FRET histograms (E) compared to the histograms obtained without BSA [48].

14. Sba1 stabilizes the ATP bound, N-terminally closed state of yHsp90

14.1. How do cochaperones change the Hsp90 mechanistics?

Single molecule two and three color FRET revealed drastic differences in the mechanochemical cycles of yHsp90 and HtpG. Whereas yHsp90 does not show a successive ATPase cycle, but is mainly diffusing through a network of states, driven by thermal fluctuations, HtpG shows a mechanical ratchet mechanism. Anyway there is another big difference between yHsp90 and HtpG. yHsp90 is known to bind several proteins that modify its function - so called cochaperones. This is not the case for HtpG. Often also cochaperone binding itself is influenced by the nucleotide state of Hsp90, leading to very complex dynamics [90, 36, 37, 40]. To observe those dynamics the simultaneous observation of Hsp90, ATP binding and cochaperone binding has to be done. This can be achieved by four color FRET. The setup for those measurements is described in sec. 8.1. One of those cochaperones is Sba1 which is known to bind to the N-terminal domain of yHsp90 and slows down the ATPase rate. Anyway it is not known to which state of yHsp90 Sba1 binds and how the binding of Sba1 is influencing the yHsp90 dynamics. Both questions were addressed here.

14.2. Sba1 stabilizes ATP bound, closed state of yHsp90

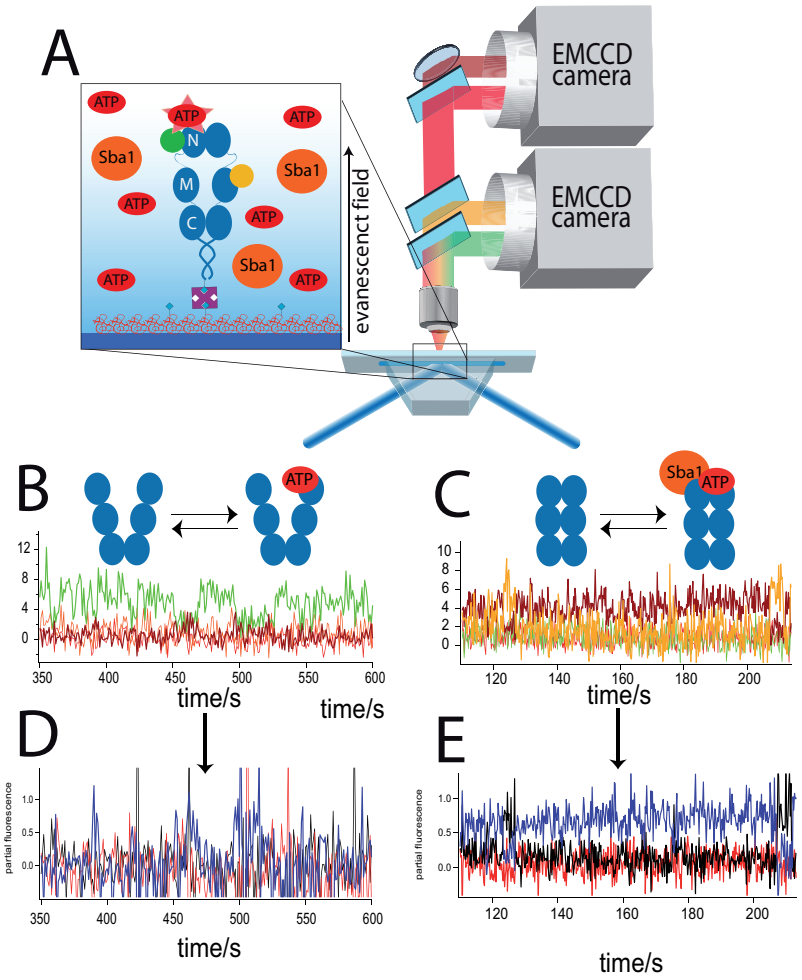

Figure 14.1.: (A) The Hsp90 heterodimers bearing Atto488 and Atto 550 were fixed to the surface and Sba1 labeled with Atto594 and ATP labeled with Atto647N at the gamma phosphate were flushed into the measurement chamber. A four color detection allows detection the signals of all involved dyes. Two types of curves could be found binding of ATP in the open state (B,D) and the closed state (C,E). The ATP bound dwell time in the closed state is massively prolonged by the presence of Sba1 (see also Fig. 14.2). In (B) and (C) the colors of the curves are corresponding to the color code for the different components in (A). In (D) and (E) the black curve shows PF_1 (Atto 550 signal divided by all others), the red curve shows PF_2 (Atto 594 signal divided by all others) and the blue curve shows PF_3 (Atto 647N signal divided by all others)

To investigate to which state of Hsp90 Sba1 binds a four color FRET assay was developed as depicted in Fig. 14.1. Hsp90 heterodimers with the dyes Atto488 (position 61) and Atto550 (position 385 of the other monomer) - analog to the measurements shown in chapter 11 - were fixed to the measurement chamber. Sba1 labeled at position 66 with an Atto594 dye and γATP bearing Atto647N were flushed into the measurement chamber with a concentration of 500nM for Sba1 and 200nM for γATP. It has to be mentioned here that the Sba1 was labeled via imine formation on the artificial amino acid p-acetylphenylalanine (as described in sec. 5.2.1) which lead to a DOL of only around 20%. Thus effectively only 100nM labeled Sba1 were in solution. The Atto488 dye was directly illuminated with the 473nm laser and all four fluorescence intensities observed over time and partial fluorescence intensities calculated analog to the three color measurements (Appendix B). Mainly two types of curves could be obtained shown in Fig. 14.1: Binding of the ATP to the open state of yHsp90 and to the closed state yHsp90. Interestingly no signal of Sba1 could be observed. Therefore immediately the question arises: Does Sba1 bind at all? Looking upon the example curve of ATP binding in the closed state one realizes that the binding times of ATP are much longer than in the absence of Sba1 (Fig. 11.1). To show this in more detail the data was plotted as histograms. Since the signal of the Sba1 attached Atto 594 dye stayed zero all the time this signal was omitted. It does no add information but only increases noise of the partial fluorescence intensities. The two remaining partial fluorescence signals were plotted in two dimensional histograms. This histograms are completely analogue to the ones obtained for the three color measurements and can be directly compared to them. They are shown in Fig. 14.2. Indeed it can be clearly seen that compared to the situation without Sba1 (Fig. 14.2A) the presence of Sba1 shifts the Hsp90 system to the ATP bound closed state (state 2 in Fig. 14.2B). Although Sba1 stabilizes the ATP binding in the closed state, still binding of ATP to the open state can be observe which means that the system is not completely shifted to the closed state (Fig. 14.2 D).

[H!]

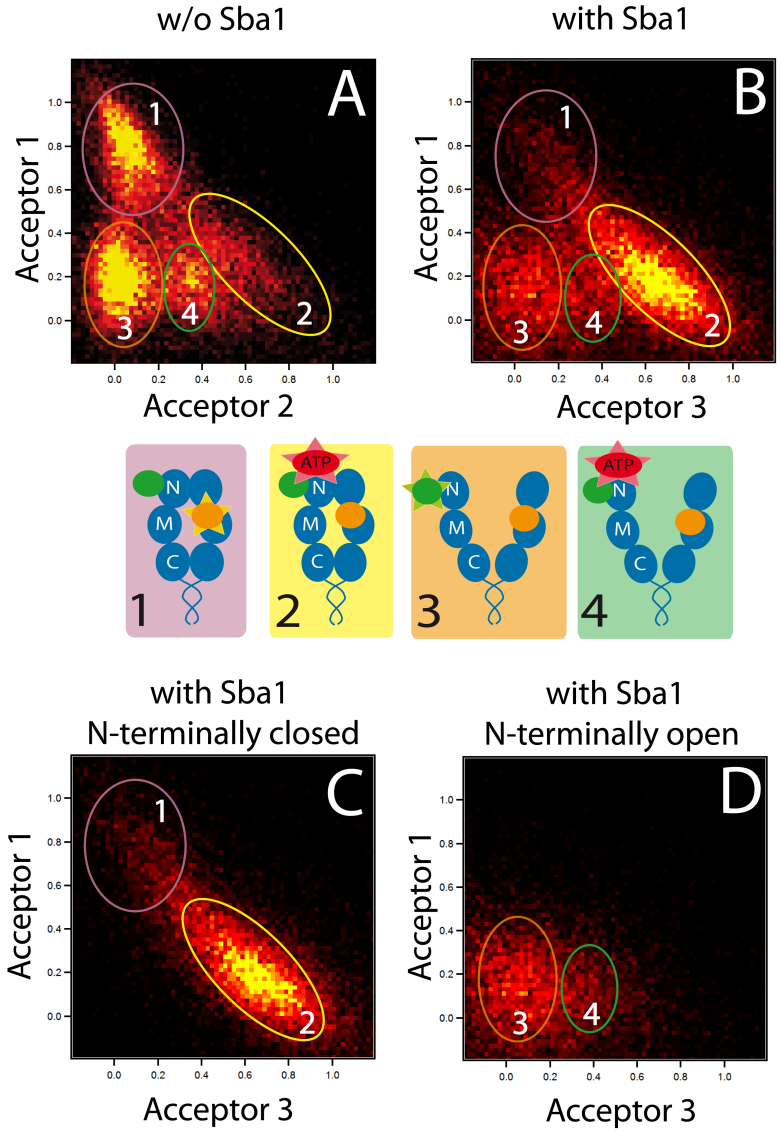

Figure 14.2.: (A) 2D Histogram from three color measurements without Sba1 as also shown in chapter 11. (B) In the presence of Sba1 a clear shift towards the closed ATP bound state (state 2) can be seen. (C) and (D) show the histograms for the closed and open curves separately obtained in the presence of Sba1.

Anyway comparing Fig. 14.2A and Fig. 14.2B it can be seen that in general the open states (3 and 4) are less pronounced in the presence of Sba1. Since the open curves are because of the pretty big fluorescence background (there are 100nM labeled Sba1 and 200nM labeled ATP freely floating in solution) sometimes difficult to be detected it might be the case that open curves are overseen and the open state are underestimated. But the observation that the yHsp90 is shifted to the more

closed state in the presence of Sba1 is also supported by bulk data. Thus increasing concentration of Sba1 in the presence of ATP-γS leads to successive closing of Hsp90 [94].

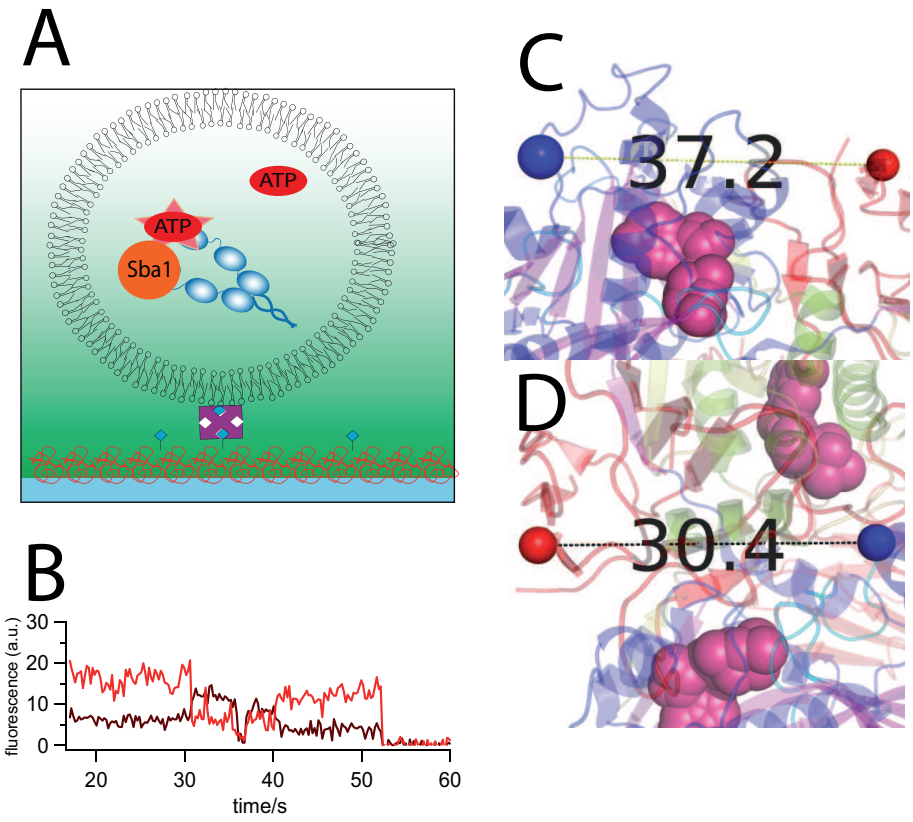

Figure 14.3.: (A) Encapsulation of labeled ATP and Sba1 in a vesicle with unlabeled Hsp90 and the excitation of the Sba1 dye shows energy transfer from Sba1 to ATP (B) and therefore binding of Sba1 and ATP at the same time. Anyway since the ATP is pretty soon hydrolyzed in the vesicle this measurements are not suited to produce good statistics, but good enough to confirm the simultaneous binding of ATP and Sba1. (C,D) Distances between the p23 66 pAcF (red sphere) and Hsp90 attached dyes (both blue spheres) at position 61C (C) and 385C (D)in angstrom. Both distances are smaller than the Förster distances for the corresponding dye pairs (5.7nm for Atto 488 and Atto 594 in (C) and 6.8nm for Atto 550 and Atto 594 in (D)).

Although a clear effect of Sba1 can be measured, the binding of Sba1 can not be observed directly. The Sba1 is labeled at position 66 which was chosen according the crystal structure (Fig. 14.3C and D). The distance between this position and the label position at the Hsp90 are 3.7nm between Sba1 66 p-AcF and Hsp90 61C and

3.0nm between Sba1 66 pAcF and Hsp90 385C; thus clearly FRET between Hsp90 and Sba1 should be detected, which is not the case. By repeating the measurement with label free ATP it could also be excluded that the energy transfer to the Atto647N at the γATP removes all the energy from the Atto 594 of the Sba1 and thus quenches this dye; also in this case no Sba1 signal could be detected. Moreover it was tried to measure FRET between Sba1 and γATP when both are bound to unlabeled Hsp90. Therefore labeled Sba1 and γATP together with Hsp90 were encapsulated in vesicles and the Atto594 was directly illuminated. Indeed a few curves showing FRET from Sba1 to ATP could be found (Fig. 14.3). Unfortunately the γATP is cleaved within a few minutes and thus this measurement can't be used for more than a proof of principle measurement. Anyway it clearly shows Sba1 binding to Hsp90. These findings can only be explained when the crystal structure is not representing the structure in free solution. This is also supported by the already explained finding that the N-terminus of Hsp90 is more extended than shown by the crystal structure.

Summing up it could be shown that Sba1 stabilizes the closed ATP bound state of yHsp90 and thus acts very specific upon the overall yHsp90 dynamics. This finding is consistent with the existing data about Sba1, that show that Sba1 binds efficiently only the ATP/AMP-PNP loaded yHsp90 [90]; also the yHsp90 crystal structure shows a closed ATP and Sba1 bound state. In contrast the quaternary structure of the yHsp90/Sba1 complex is not the one shown in the crystal structure, but obviously more expanded or rearranged in solution. Altogether the technical approach of four color FRET allowing to investigate simultaneously Hsp90 dynamics, nucleotide turnover and cochaperone binding offers a new way to understand Hsp90 dynamics and function in more detail.

A. Appendix A: C-terminal dynamics of yHsp90

A.1. Calculation of the Förster distance

The Förster distance in angstrom was calculated according to

$$R_0 = \left(9,780 \cdot \frac{Q_D \cdot \kappa^2}{n^4}\right)^{1/6} \tag{A.1}$$

with κ^2 as orientation factor set to 2/3 for freely rotating dyes, n the refractive index of water equal to 1.33, Q_D the quantum efficiency of the donor, which is given as $Q_D = \frac{\tau_m}{\tau_{rad}}$ with τ_m the measured lifetime in our system, and τ_rad the radiative lifetime of the dye. For our system Q was calculated with the assumption of a constant τ_{rad} according to $Q_D = \frac{\tau_m}{\tau_{lit}/Q_{lit}}$ with τ_m the measured fluorescence lifetime and τ_{lit} and Q_{lit} the lifetime and quantum efficiency given by AttoTec for these dyes. The resulting Förster distance for our system is then 5.1 nm. With this the inter dye distance is calculated as

$$R = \left(\frac{1 - E_{FRET}}{E_{FRET}}\right)^{1/6} \cdot R_0 \tag{A.2}$$

A.2. Supplementary figures and tables

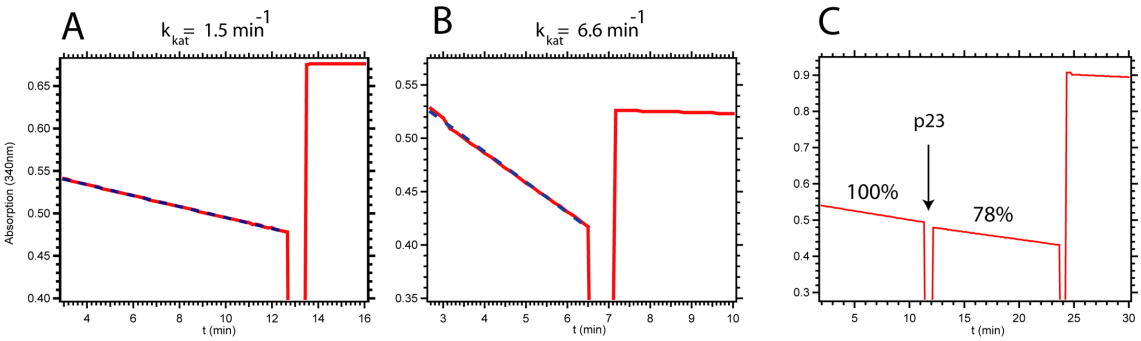

Figure A.1.: ATPase Assays. The 560C mutation does not influence the ATPase of any of the constructs within the uncertainty of the measurement. As an example we show in A the full-length 560C mutation with normal ATPase activity and inhibition by Radicicol [95] (after around 13 min) and in B the Coil-NMC Hsp90 560C mutant with a higher ATPase activity than the wild-type Hsp90 protein consistent with higher ATPase of Coil-NMC without the 560C mutation. Finally, Sba1 binding is not inhibited by the 560C mutation, which can be seen in C, where the typical ATPase inhibition after Sba1 addition to Δ8 (560C) can be observed. In the case of Coil-NMC and Δ8 (560C) the labeling process seems to lower the ATPase activity by a factor of 2. This is likely caused by aggregation during the labeling process because the same effect is seen upon the addition of pure DMSO. For the single-molecule experiments, aggregation and inactive protein is irrelevant because we select active single molecules. The ATPase assay was done with an ATP recovering assay as described in [96] . In short the produced ADP is recovered by pyruvate kinase in the presence of posphonenolpyruvate. The produced pyruvate is reduced to lactate by lactate dehydrogenase whereas NADH is oxidizied to NAD^+. The oxidation of NADH leads to a spectral shift and therefore to a change in the absorption at 340 nm with time. This can be observed in the photometer (DU 730, Beckman Coulter). The assay was done at 37 °C. The literature values for the ATPase activity of Hsp90 lie in the range of 0.5–1.5 min^{-1} [9, 18, 49]. Sba1 is known to bind to Hsp90 and inhibit the ATPase activity [36]. Radicicol is an ATP-mimicking inhibitor that specifically inhibits Hsp90 and thus can be used to estimate the background ATPase activity.

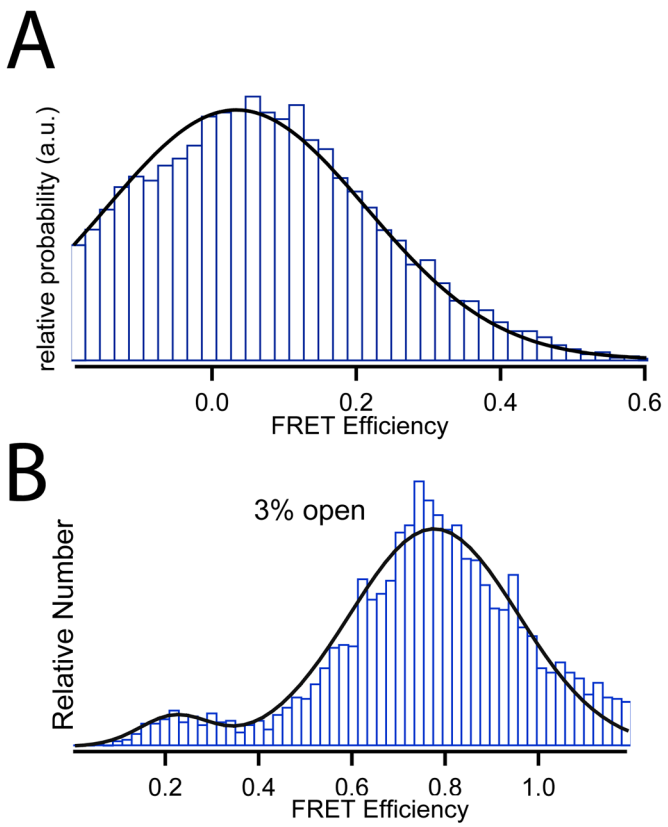

Figure A.2.: FRET efficiency histogram of non-interacting dyes and in the presence of Sti1. (A) Using heterodimers with one monomer labeled with ATTO 550 at position 61 (in the N terminus) and one monomer labeled with ATTO 647N at position 560 (in the C terminus) an average FRET efficiency of 0.03 was obtained. This shows that the FRET efficiency of 0.2 measured in our C-terminal dynamics experiments does not result from photon leakage of donor photons into the acceptor channel or from unspecific interaction between the proteins. (B) The described single-molecule FRET measurements of the C-terminal dimerization have been repeated for the full length Hsp90 in the presence of 1 µM Sti1 (in absence of nucleotide). In this case Hsp90 can be found mainly in the C-terminal closed state. This is consistent with the proposed function of Sti1, which likely binds to the C-terminal domains and opens the N-terminal domains.

Open					
	A_1	τ_1	A_2	τ_2	Chi^2
Δ8	-0,26±0,01	0,81±0,07	-0,75±0,01	5,77±0,16	0,07
Δ24	-0,41±0,01	1,21±0,05	-0,59±0,01	11,18±0,35	0,03
Δ8ATP	-0,28±0,01	1,31±0,09	-0,72±0,01	11,82±0,34	0,02
Coil-NMC	-0,37±0,02	0,15±0,02	-0,58±0,02	2,07±0,19	0,03
Closed					
	A_1	τ_1	A_2	τ_2	Chi^2
Δ8	-0,83±0,01	1,01±0,02	-0,22±0,01	8,42±0,8	0,04
Δ24	-0,66±0,02	0,98±0,03	-0,33±0,01	6,03±0,4	0,02
Δ8ATP	-0,61±0,02	0,49±0,02	-0,37±0,02	3,62±0,33	0,05
Coil-NMC	-0,59±0,03	0,20±0,01	-0,33±0,03	2,27±0,42	0,03

Open					
	A_1	τ_1	A_2	τ_2	Chi^2
No	-0,59±0,01	1,45±0,04	-0,43±0,01	10,40±0,61	0,06
ATP	-0,25±0,01	0,79±0,05	-0,72±0,01	5,46±0,15	0,05
ADP	-0,49±0,02	2,96±0,1	-0,48±0,02	12,78±0,6	0,02
γSATP	-0,47±0,03	1,23±0,05	-0,56±0,03	4,03±0,17	0,03
AMPPNP	-0,23±0,00	0,67±0,03	-0,75±0,00	6,14±0,07	0,03
Closed					
	A_1	τ_1	A_2	τ_2	Chi^2
No	-0,40±0,01	0,85±0,03	-0,60±0,01	8,16±0,2	0,06
ATP	-0,91±0,02	1,54±0,04	-0,20±0,04	20,64±10,5	0,12
ADP	-0,92±0,01	1,01±0,02	-0,16±0,01	10,60±2,62	0,09
γSATP	-0,91±0,15	1,72±0,04	-0,13±0,23	8,04±0,00	0,08
AMPPNP	-0,37±0,00	0,75±0,01	-0,62±0,00	7,37±0,09	0,02

Figure A.3.: The table shows amplitudes (A_i), decay times (τ_i in s), and chi-square values (Chi^2) for all measured mutants (upper part) and nucleotide conditions (No is no nucleotide) of wild-type yeast Hsp90 (lower part). The decay times for the open states correspond to the on-rate constants and the decay times for the closed states to the off-rate constants.

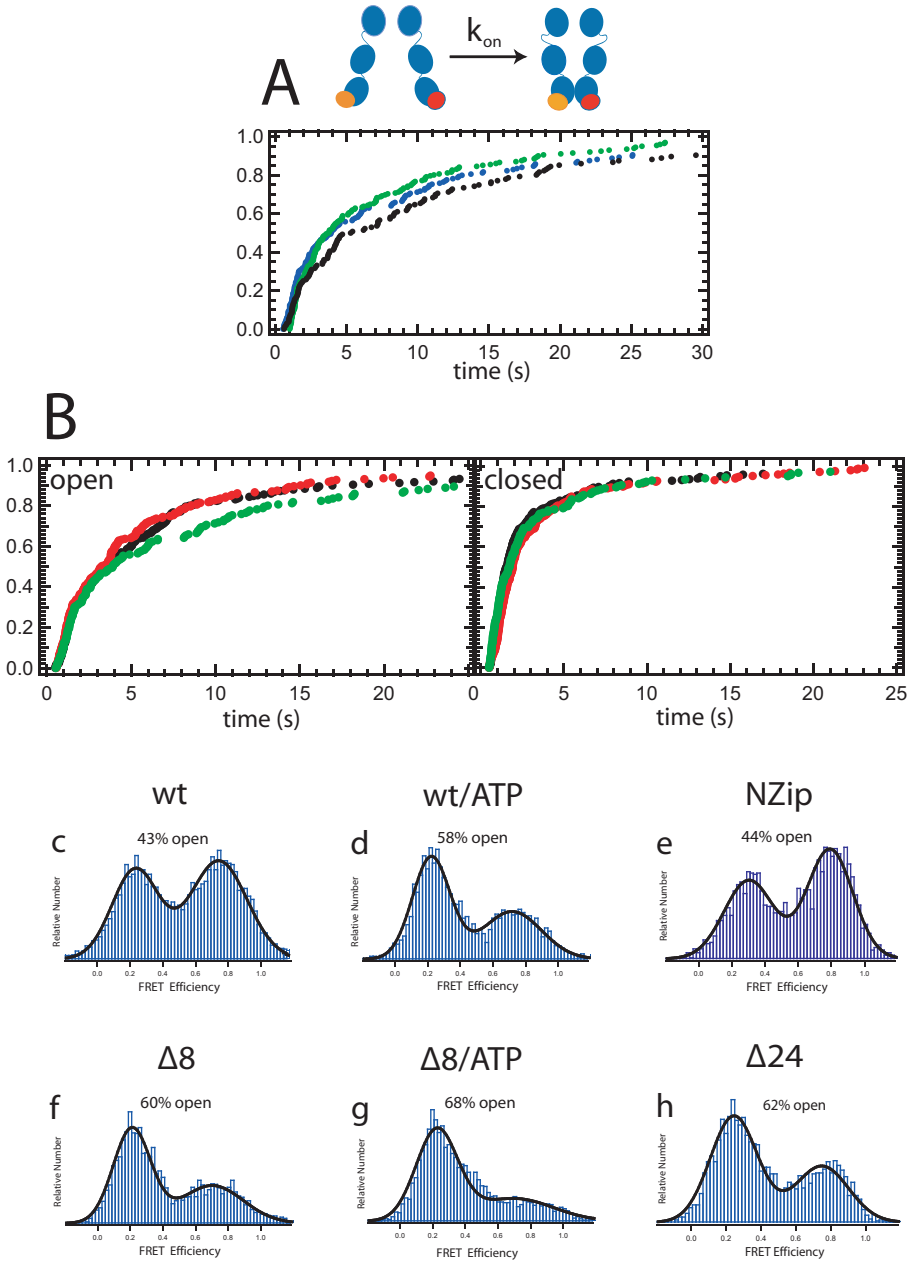

Figure A.4.: Effect of N-terminal mutations on C-terminal kinetics. (A) Dwell-time distributions for C-terminal open times (k_{on}) are similar for the Δ8 Hsp90 with ATP (N-terminally permanently closed, black), Δ24 Hsp90 (less stable N-terminal dimerization, blue), and wild-type Hsp90 (N-terminal open and closed equilibrium, green). (B) Comparison of full-length Hsp90 and the deletion constructs: Dwell-time distributions for Δ8 (black), Δ24 (green) in the absence of nucleotide and the full-length construct in the presence of ATP (red) are very similar. (c–f) C-terminal FRET efficiencies for the different N-terminal mutations. High FRET values correspond to the C-terminal closed state and low FRET values to the C-terminal open state.

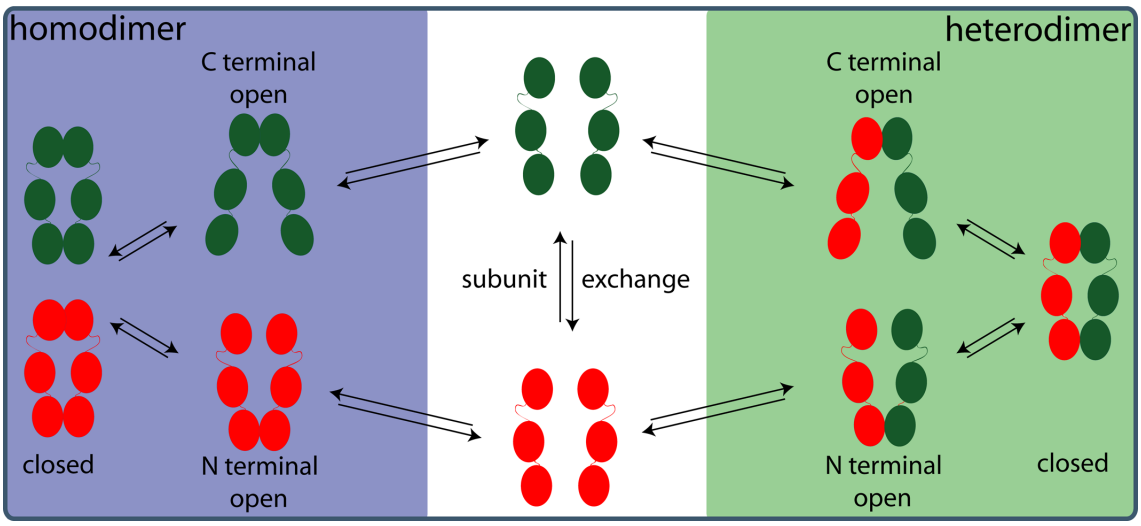

Figure A.5.: Reaction pathway scheme for the Hsp90 subunit exchange reaction. The N- and C-terminal openings are regarded as independent. The rates are obtained from Fig. A.3 and from Mickler et al. [48]. In all cases the slowest rates have been chosen.

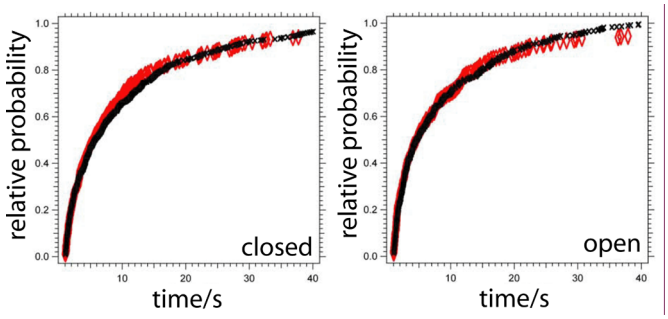

Figure A.6.: Comparison of N-N domain vs N-M domain movement. The dynamics of the N-terminal dynamics (red) is the same as can be observed for the N-M domain movement (black), both in the presence of 2 mM ATP. This shows that the N- and M- domains are quite rigidly linked and move as one unit during the N-terminal opening process. Furthermore, this means that no permanent middle domain interaction takes place and that our results therefore cannot be explained by a holiday junction-like movement.

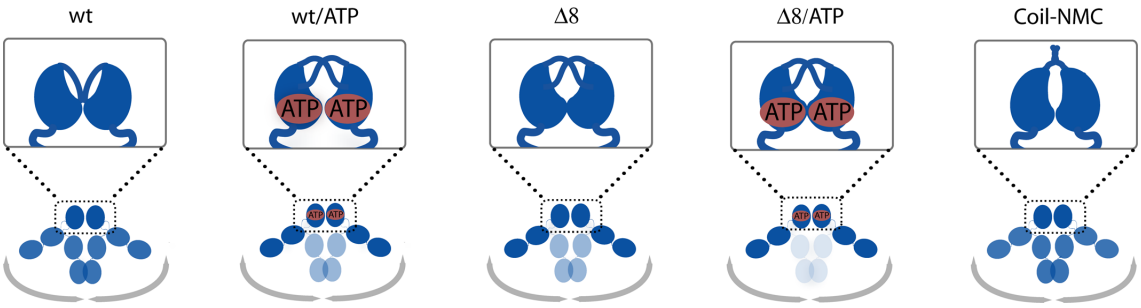

Figure A.7.: Scheme of the mechanochemical coupling. Structural model for the position of the N-terminal lid in the various mutants in the presence and absence of ATP. In addition, the occupancy of the C-terminal dimerization equilibrium is given: Dark blue represents high occupancy of the state and light blue represents low occupancy of the state. ATP binding (not hydrolysis) leads to a release of the N-terminal lid, which then can cross-activate the second Hsp90 monomer. In the Δ8 deletion mutant, this process is mimicked [48, 97]. So binding of ATP and deletion of the first 8 amino acids lead both to the same effect, namely, the unbinding of the N-terminal lid. This explains why Δ8 mutant and wild type with ATP also show similar C-terminal dynamics.

B. Appendix B: Three color FRET on yHsp90

B.1. Data evaluation

The three fluorescence colors were separated, filtered, and simultaneously recorded on an Andor DV887 (Andor Technology) camera . The movies were analyzed with a program based on Igor Pro 6.01 (WaveMetrics): First, the time traces of single fluorophores were extracted from the movie with a threshold criterion; then, the three colors were overlaid and the corrected partial fluorescence (PF) for each color calculated as

$$PF_1 = \frac{\gamma_1 \left(I_{A1} - \beta_1 I_D\right)}{I_D + \gamma_1 \left(I_{A1} - \beta_1 I_D\right) + \gamma_2 \left(I_{A2} - \beta_2 I_D\right)} \tag{B.1}$$

$$PF_2 = \frac{\gamma_2 \left(I_{A2} - \beta_2 I_D\right)}{I_D + \gamma_1 \left(I_{A1} - \beta_1 I_D\right) + \gamma_2 \left(I_{A2} - \beta_2 I_D\right)} \tag{B.2}$$

$$PF_D = \frac{I_D}{I_D + \gamma_1 \left(I_{A1} - \beta_1 I_D\right) + \gamma_2 \left(I_{A2} - \beta_2 I_D\right)} = 1 - \left(PF_1 + PF_2\right) \tag{B.3}$$

and

$$E_{ALEX}^{FRET} = \frac{\gamma_2 \left(I_{A2}^{532nm} - \beta_3 I_{A1}^{532nm}\right)}{\gamma_1 I_{A1}^{532nm} + \gamma_2 \left(I_{A2}^{532nm} - \beta_3 I_{A1}^{532nm}\right)} \tag{B.4}$$

$PF_{1/2}$ is the PF of acceptor 1 and 2, respectively. PF_D is the PF of the donor, I_D and $I_{A1}$and I_{A2} are the donor and acceptor intensities at excitation of the donor dye, and I_{A2}^{532nm} andI_{A1}^{532nm} are the intensities of acceptor 1 and 2 upon excitation of the acceptor 1 dye, respectively. E_{ALEX}^{FRET} is the PF of acceptor 2 upon direct excitation of acceptor 1. The cross-talk from the acceptor 1 to acceptor 2 channel upon excitation of the acceptor 1 was close to zero, and therefore we have β_3= 0 in the following. $\gamma_{1/2}$ are correction factors that take the different quantum efficiencies of the dyes and the different detection sensitivities of the setup for the three dyes into account. These gamma factors are given as

$$\gamma_{1/2} = \frac{\delta I_D}{\delta I_{A1/2}} = \frac{\epsilon_D Q_D}{\varepsilon_{A1/2} Q_{A1/2}} \tag{B.5}$$

$\delta I_{A1/2}$ and δI_d are changes of acceptor and donor intensities upon acceptor bleaching, ϵ_D and $\epsilon_{A1/2}$ are the detector efficiencies for each dye, and Q_D and $Q_{A1/2}$ are the quantum efficiencies of each dye. The $\gamma_{1/2}$ factor here is the inverse of the $\gamma_{1/2}$ factor introduced in sec. 8.1.2.1. The γ factor was measured for many curves, and its values are close to $\gamma_{1/2} = 0.7$; therefore, these values have been used to correct all FRET curves. The betas correct for the leakage of photons from the donor into the two acceptor channels. They are estimated by dividing the intensity measured in the acceptor 1 and acceptor 2 channels by the donor intensity in the presence of only donor dye upon excitation with the 473-nm laser:

$$\beta_{1/2} = \left.\frac{I_{A1/2}}{I_D}\right|_{473nm} \tag{B.6}$$

$\beta_1$is around 0.126, and β_2 is around 0.024 in our system. At the used intensities, no cross-excitation of the dyes (e.g., direct excitation of the Atto550 with the 473-nm laser or excitation of the Atto647N with the 532-nm laser) could be detected; therefore, such cross-excitation is neglected in the following. The photostability of the Atto 647N and Atto 550 dyes under the used conditions has been demonstrated in the past [48]. Blinking of the Atto 488 can be excluded because blinking of this dye would result in a donor signal going down to zero, which has not been observed here. The obtained two FRET efficiencies (every single data point) are then accumulated

into a two-dimensional histogram as shown in Fig. 11.1. Because the sum of all PFs is equal to one, the data points can only be found below the line from x,y=1,0 to x,y=0,1. To obtain the transition kinetics, Hidden-Markov modeling was used. In detail, I used the Viterbi algorithm as described above (sec. 8.1.2.3). The rates for the transitions were then determined from these reconstructed FRET traces.We accumulated all dwell times for a certain state and plotted the integrated dwell times in histograms as shown in Fig. 11.4. The normalized histograms are fitted with exponentials. The amplitude information (which is lost upon normalization) is not needed in the following as explained below. Importantly, the obtained "effective" decay times ($1/k_{eff}$) are not exactly the inverse of the rate constant k of one state to another, because the obtained effective rate constant k_{eff} is the sum of all rate constants depopulating the starting state; for four states this can be up to three rate constants k_i. In general, the probability of having left a state until time t is

$$p(t) = A\left(1 - \exp\left(-k_{eff}t\right)\right) = \frac{k}{k_{eff}}\left(1 - \exp\left(-k_{eff}t\right)\right) \tag{B.7}$$

From this equation, the rate constant for a certain decay can be obtained by

$$k = Ak_{eff} \tag{B.8}$$

Fortunately, the binding and unbinding rates of the nucleotides are at least one order of magnitude faster than the conformational changes. Therefore, there is only one dominant pathway for the depopulation of every state and A becomes close to one, which directly allows extracting the rate constants. The kinetics can then be fitted with a monoexponential function. Nucleotide binding itself is in general a second-order process described by

$$\frac{\partial N_{ab}}{\partial t} = -kN_aN_b \tag{B.9}$$

N_a and N_b are the concentration of ATP and heat shock protein 90 (Hsp90), respectively. N_{ab} is the concentration of the ATP bound complex. Because the nucleotide concentration is 200 nM and therefore much higher than the protein concentration

(less than 1 nM), it can be regarded as constant and B.9 simplifies to a pseudo first-order reaction:

$$\frac{\partial N_{ab}}{\partial t} = -kN_aN_b = -k_{eff}N_b \tag{B.10}$$

B.2. Distance estimation from multicolor FRET data

For two-dye systems, the distance between the two dyes can be estimated by

$$d = R_o\sqrt[6]{\frac{1}{\tau_D k_{FRET}}} \tag{B.11}$$

R_0 is the Förster distance, τ_D is the fluorescence lifetime in the absence of acceptor dye, and k_{FRET} is the rate of energy transfer between the dyes (see alsosec. 8.1.2.2). In the case of multicolor FRET, the single FRET efficiencies (e.g., the efficiency of the energy transfer from one dye to another one) cannot directly be measured, because the signal results from the sum of all energy transfers [98, 99]. The rate constants therefore have to be recovered as follows. The fluorescence intensity (photons over time) of the donor is given by

$$I_d = Q_d N_d \tag{B.12}$$

N_d is the number of absorbed photons per time and Q_d is the effective quantum efficiency in the presence of FRET of the donor:

$$Q_d = \frac{k_{rad}}{k_{rad} + k_{non-rad} + \sum_i k^i_{FRET}} \tag{B.13}$$

k_{rad} is the radiation rate of the donor, $k_{non-rad}$ is the non-radiative depopulation, and k^i_{FRET} is the FRET rate from the donor to the i-th acceptor. For the first

acceptor (upon donor excitation), we have, accordingly,

$$I_{A1} = Q_{a1} N_{a1} = Q_{a1} \frac{k_{FRET}^{d\to a1}}{\sum_j k_{d\to}^j} N_d \tag{B.14}$$

$k_{FRET}^{d\to a1}$ is the FRET rate from donor to acceptor 1, and $\sum_j k_{d\to}^j$ are all rates that depopulate the excited state of the donor. FRET from acceptor 1 back to the donor is very small (because of the very small overlap of the spectra) and can therefore be neglected. For the second acceptor (upon donor excitation), we have, accordingly,

$$I_{A2} = Q_{a2} N_{a2} = Q_{a2} \left(\frac{k_{FRET}^{d\to a2}}{\sum_j k_{d\to}^j} N_d + \frac{k_{FRET}^{a1\to a2}}{\sum_j k_{a1\to}^j} N_{a1} \right) \tag{B.15}$$

Inserting B.14, we get

$$I_{A2} = Q_{a2} \left(\frac{k_{FRET}^{d\to a2}}{\sum_j k_{d\to}^j} + \frac{k_{FRET}^{a1\to a2}}{\sum_j k_{a1\to}^j} \frac{k_{FRET}^{d\to a1}}{\sum_j k_{d\to}^j} \right) N_d \tag{B.16}$$

The first term in the bracket corresponds to direct transfer from donor to acceptor 2 and the second term corresponds to transfer from acceptor 1 to acceptor 2. From these formulas, the expressions for PF (compare Eqs. B.1, B.2 and B.4) can be derived as follows:

$$PF_1 = \frac{I_{A1}}{I_D + I_{A1} + I_{A2}} = \frac{Q_{a1} \frac{k_{FRET}^{d\to a1}}{\sum_j k_{d\to}^j}}{Q_d + Q_{a1} \frac{k_{FRET}^{d\to a1}}{\sum_j k_{d\to}^j} + Q_{a2} \left(\frac{k_{FRET}^{d\to a2}}{\sum_j k_{d\to}^j} + \frac{k_{FRET}^{a1\to a2}}{\sum_j k_{a1\to}^j} \frac{k_{FRET}^{d\to a1}}{\sum_j k_{d\to}^j} \right)} \tag{B.17}$$

$$PF_2 = \frac{I_{A2}}{I_D + I_{A1} + I_{A2}} = \frac{Q_{a2}\left(\frac{k_{FRET}^{d\to a2}}{\sum_j k_{d\to}^j} + \frac{k_{FRET}^{a1\to a2}}{\sum_j k_{a1\to}^j}\frac{k_{FRET}^{d\to a1}}{\sum_j k_{d\to}^j}\right)}{Q_d + Q_{a1}\frac{k_{FRET}^{d\to a1}}{\sum_j k_{d\to}^j} + Q_{a2}\left(\frac{k_{FRET}^{d\to a2}}{\sum_j k_{d\to}^j} + \frac{k_{FRET}^{a1\to a2}}{\sum_j k_{a1\to}^j}\frac{k_{FRET}^{d\to a1}}{\sum_j k_{d\to}^j}\right)} \quad \text{(B.18)}$$

and

$$E_{ALEX}^{FRET} = \frac{\gamma_2 I_{A2}^{532nm}}{\gamma_1 I_{A1}^{532nm} + \gamma_2 I_{A2}^{532nm}} \quad \text{(B.19)}$$

The measured intensity I^{mea} is not equal to the emitted intensity I from Eqs.B.17, B.18 and B.19, because it has to be corrected for the efficiencies of the detection channels ϵ_i (note: the γ factor is ϵ_i times the quantum efficiency Q, and I^{mea} should already be corrected for cross-talk as shown in Eqs.B.1-B.4 but not corrected for the γ factors):

$$I_i^{mea} = \varepsilon_i I_i \to I_i = \frac{1}{\varepsilon_i} I_i^{mea} \quad \text{(B.20)}$$

The following ratios of ϵ_i can be expressed in terms of the γ factors and quantum efficiencies $Q_i^{nf}$of the dye in the absence of FRET (which are given by the provider of the dyes):

$$\frac{\varepsilon_d}{\varepsilon_{a1}} = \gamma_1 \frac{Q_{a1}^{nf}}{Q_d^{nf}} \quad \text{(B.21)}$$

$$\frac{\varepsilon_d}{\varepsilon_{a2}} = \gamma_2 \frac{Q_{a2}^{nf}}{Q_d^{nf}} \quad \text{(B.22)}$$

The PF can then be written as

$$PF_1 = \frac{\gamma_1 I_{a1}^{mea} \frac{Q_{a1}^{nf}}{Q_d^{nf}}}{\gamma_1 I_{a1}^{mea} \frac{Q_{a1}^{nf}}{Q_d^{nf}} + \gamma_2 I_{a2}^{mea} \frac{Q_{a2}^{nf}}{Q_d^{nf}} + I_d^{mea}} \tag{B.23}$$

$$PF_2 = \frac{\gamma_2 I_{a2}^{mea} \frac{Q_{a2}^{nf}}{Q_d^{nf}}}{\gamma_1 I_{a1}^{mea} \frac{Q_{a1}^{nf}}{Q_d^{nf}} + \gamma_2 I_{a2}^{mea} \frac{Q_{a2}^{nf}}{Q_d^{nf}} + I_d^{mea}} \tag{B.24}$$

Because the quantum efficiencies of the used dyes are similar, we can set them equal, which simplifies Eqs.B.23 and B.24 to

$$PF_1 = \frac{\gamma_1 I_{a1}^{mea}}{\gamma_1 I_{a1}^{mea} + \gamma_2 I_{a2}^{mea} + I_d^{mea}} \tag{B.25}$$

$$PF_2 = \frac{\gamma_2 I_{a2}^{mea}}{\gamma_1 I_{a1}^{mea} + \gamma_2 I_{a2}^{mea} + I_d^{mea}} \tag{B.26}$$

These are the values plotted in the histograms shown in Fig. 11.1 and Fig. 12.3 and the values given in Eqs. B.1 and B.2, if the crosstalk correction is taken into account. This can be done in an analogue way for Eq. B.19 (acceptor 2 signal upon acceptor 1 excitation). We can now substitute $\sum_j k_{d/a1/a2\rightarrow}^j = \frac{k_{d/a1/a2_{rad}}}{Q_{d/a1/a2}}$ in Eqs. B.17 and B.18 and get

$$PF_1 = \frac{Q_{a1} \frac{k_{FRET}^{d\rightarrow a1} Q_D}{k_{rad}^d}}{Q_d + Q_{a1} \frac{k_{FRET}^{d\rightarrow a1} Q_D}{k_{rad}^d} + Q_{a2} \left(\frac{k_{FRET}^{d\rightarrow a2} Q_D}{k_{rad}^d} + \frac{k_{FRET}^{a1\rightarrow a2} Q_{a1}}{k_{rad}^{a1}} \frac{k_{FRET}^{d\rightarrow a1} Q_D}{k_{rad}^d} \right)} \tag{B.27}$$

and

$$PF_2 = \frac{Q_{a2}\left(\frac{k_{FRET}^{d\to a2}Q_D}{k_{rad}^d} + \frac{k_{FRET}^{a1\to a2}Q_{a1}}{k_{rad}^{a1}}\frac{k_{FRET}^{d\to a1}Q_D}{k_{rad}^d}\right)}{Q_d + Q_{a1}\frac{k_{FRET}^{d\to a1}Q_D}{k_{rad}^d} + Q_{a2}\left(\frac{k_{FRET}^{d\to a2}Q_D}{k_{rad}^d} + \frac{k_{FRET}^{a1\to a2}Q_{a1}}{k_{rad}^{a1}}\frac{k_{FRET}^{d\to a1}Q_D}{k_{rad}^d}\right)} \tag{B.28}$$

Reformulation of Eq. B.13 utilizing Q^{nf} (the quantum efficiency in the absence of FRET) yields

$$\frac{1}{Q} = \frac{k_{rad} + k_{non-rad}}{k_{rad}} + \frac{\sum_i k_{FRET}^j}{k_{rad}} = \frac{1}{Q^{nf}} + \frac{\sum_i k_{FRET}^j}{k_{rad}} \tag{B.29}$$

and we get, therefore,

$$Q_d = \frac{1}{\frac{1}{Q_d^{nf}} + \frac{k_{FRET}^{d\to a1}}{k_{rad}^d} + \frac{k_{FRET}^{d\to a2}}{k_{rad}^d}} \tag{B.30}$$

and

$$Q_{a1} = \frac{1}{\frac{1}{Q_{a1}^{nf}} + \frac{k_{FRET}^{a1\to a2}}{k_{rad}^{a1}}} \tag{B.31}$$

Because no FRET processes depopulate acceptor 2, $Q_{a2} = Q_{a2}^{nf}$ and, therefore,

$$\begin{aligned} PF_1 = {} & (k_{FRET}^{d\to a1}k_{rad}^{a1}Q_{a1}^{nf})/k_{rad}^d k_{rad}^{a1} + k_{rad}^d k_{FRET}^{a1\to a2}Q_{a1}^{nf} + Q_{a1}^{nf}k_{rad}^{a1}k_{FRET}^{d\to a1} \\ & + Q_{a2}^{nf}k_{FRET}^{d\to a2}k_{rad}^{a1} + Q_{a2}^{nf}k_{FRET}^{d\to a2}k_{FRET}^{a1\to a2}Q_{a1}^{nf} + Q_{a2}^{nf}k_{FRET}^{a1\to a2}Q_{a1}^{nf}k_{FRET}^{d\to a1} \end{aligned} \tag{B.32}$$

$$\begin{aligned} PF_2 = {} & (k_{FRET}^{d\to a2}k_{rad}^{a1} + k_{FRET}^{d\to a2}k_{FRET}^{a1\to a2}Q_{a1}^{nf} + k_{FRET}^{a1\to a2}Q_{a1}^{nf}k_{FRET}^{d\to a1})Q_{a2}^{nf}/ \\ & k_{rad}^d k_{rad}^{a1} + k_{rad}^d k_{FRET}^{a1\to a2}Q_{a1}^{nf} + Q_{a1}^{nf}k_{rad}^{a1}k_{FRET}^{d\to a1} + Q_{a2}^{nf}k_{FRET}^{d\to a2}k_{rad}^{a1} \\ & + Q_{a2}^{nf}k_{FRET}^{d\to a2}k_{FRET}^{a1\to a2}Q_{a1}^{nf} + Q_{a2}^{nf}k_{FRET}^{a1\to a2}Q_{a1}^{nf}k_{FRET}^{d\to a1} \end{aligned} \tag{B.33}$$

The ALEX-FRET signal allows the direct estimation of the FRET efficiency between acceptor 1 and acceptor 2:

$$E_{ALEX}^{FRET} = \frac{\gamma_2 I_{A2}^{532nm}}{\gamma_1 I_{A1}^{532nm} + \gamma_2 I_{A2}^{532nm}} = \frac{k_{FRET}^{a1\to a2}}{k_{FRET}^{a1\to a2} + \frac{1}{\tau_{a1}}} \tag{B.34}$$

where τ_{a1} is the fluorescence decay time of acceptor 1 (radiative and non-radiative). The equation system consisting of Eqs.B.32 -B.34 can now be solved for the FRET rates, which are needed to determine the distances inbetween the fluorophores according to Eq. B.11. The results are

$$k_{FRET}^{d\to a1} = -\frac{PF_1 k_{rad}^{d}(k_{rad}^{a1}\tau_d E_{ALEX}^{FRET} - k_{rad}^{a1}\tau_d - E_{ALEX}^{FRET}Q_{a1}^{nf})}{Q_{a1}^{nf} k_{rad}^{a1}\tau_d(PF_2 E_{ALEX}^{FRET} - PF_2 + PF_1 E_{ALEX}^{FRET} - PF_1 - E_{ALEX}^{FRET} + 1)} \tag{B.35}$$

$$k_{FRET}^{d\to a2} = -\frac{\left(PF_2 k_{rad}^{a1}\tau_d E_{ALEX}^{FRET} - PF_2 k_{rad}^{a1}\tau_d + PF_1 E_{ALEX}^{FRET}Q_{a1}^{nf}\right) k_{rad}^{d}}{Q_{a2}^{nf} k_{rad}^{a1}\tau_d(PF_2 E_{ALEX}^{FRET} - PF_2 + PF_1 E_{ALEX}^{FRET} - PF_1 - E_{ALEX}^{FRET} + 1)} \tag{B.36}$$

and

$$k_{FRET}^{a1\to a2} = \frac{E_{ALEX}^{FRET}}{(E_{ALEX}^{FRET} - 1)\tau_d} \tag{B.37}$$

Eqs.B.35-B.37 depend only on PF_1,PF_2 and E_{ALEX}^{FRET} , which can be directly read from the maxima in Fig. 11.5), and on parameters given by the provider of the dyes (Atto-Tec). This general treatment is not limited to a three-color case but can be extended to any number of dyes. The values for the quantum efficiencies Q and fluorescence decay times k_{rad} are given by the supplier (Atto-Tec). A summary of the maxima of PF_1,PF_2 and E_{ALEX}^{FRET} and the corresponding distances is given in Fig. 11.6. Because there is some uncertainty in the used values for the quantum efficiency, radiative lifetime, and the κ factor , the values of the distances should

be only taken as rough estimates. Nevertheless, we can estimate an uncertainty, because every distance has been measured independently at least two times, which results in an uncertainty between 0.5 and 1 nm. The values for the distance between donor and acceptor 1 in open and closed conformation are in good agreement with the distances obtained from the crystal structure. I measured the distance between the C_α atoms in the structures (Protein Data Bank ID codes 2CGE and 2CG9) with Pymol 0.99rc6 (DeLano Scientific) and obtained values of about 7.0 nm in the open state and 4.2 nm in the closed state. In contrast, the distance to the bound ATP is in all cases more than 5 nm. In the crystal structure, this distance is between 2 and 4 nm (Fig. 11.6). To exclude a quenching upon binding of ATP to labeled Hsp90, the spectra of labeled Hsp90 was measured before and after adding Hsp90 61C labeled with Atto488 or Hsp90 385C labeled with Atto550, respectively. No decrease of the fluorescence larger than the expected effect caused by dilution was observed (e.g., no contact quenching occurs). If the binding of labeled ATP would change the properties of the donor or acceptor 1 dye, this would also result in a shift of the donor or acceptor 1 distance, which cannot be observed.

B.3. Estimation of the probability of having two ATPs bound to the Hsp90 dimer

The measured mean dwell time for the Hsp90 dimer in the open state with ATP bound to the monomer bearing the Atto488 dye is τ= 2 s. The measured mean dwell time of finding the Hsp90 dimer without ATP or with ATP at the monomer bearing the Atto550 dye τ= 6 s. Thus, the probability of having ATP bound to one monomer is 25% ($\frac{2s}{2s+6s}$), and assuming independent binding the probability of finding Hsp90 with two ATPs bound is 6% (the square of the probability of binding to one monomer).

B.4. Correction of the mean dwell time for Hsp90 without bound ATP

Because the Atto488 dye is only attached to one monomer, binding of labeled ATP to the other monomer is not recognized. Therefore, the measured dwell time τ_{mo}

for the open ATP free state is a mixture of the ATP free open state and Hsp90 with ATP bound to the monomer not having the Atto488. In my measurement, I obtained for τ_{mu}= 6 s and for the mean dwell time of ATP bound to the monomer with Atto488 τ_b= 2 s. The mean dwell time for the open ATP free state of Hsp90 τ_u can be obtained as follows. Alternating laser excitation showed that the state with two ATPs bound at the same time is at least extremely rare and can be neglected in the following estimate. Thus, only Hsp90 without ATP and Hsp90 with ATP bound to the monomer with Atto488 (1) or to the other monomer (2) exist. They are connected as follows:

$$Hsp90 \bullet ATP_1 \underset{\tau_o}{\overset{\tau_b}{\rightleftharpoons}} Hsp90 \underset{\tau_b}{\overset{\tau_o}{\rightleftharpoons}} Hsp90 \bullet ATP_2 \tag{B.38}$$

Having observed ATP release, the system is in the ATP free state and again binds ATP at the monomer with the Atto488 after τ_{mu}= 6 s, which means it returns to state Hsp90 • ATP_1. The rates of binding ATP to one or the other monomer are the same, if both binding sites are empty. Thus, starting in ATP free Hsp90 the probability of returning into the state Hsp90 • ATP_1 is 0.5 but with twofold rate because two processes with the same rate are depopulating the ATP free state. The fraction that binds ATP at the other monomer Hsp90 • ATP_2 has to react back to the ATP free state where again 0.5 probability exists that it reacts to Hsp90 • ATP_1. This consideration leads to the mathematical row:

$$\tau_{mu} = \sum_{N=1}^{\infty} 0.5^N \left(N\tau_u + (N-1)\,\tau_b\right) \tag{B.39}$$

For $N \to \infty$, this sum converges to

$$\tau_{mu} = \tau_u + 2\tau_b \tag{B.40}$$

and thus

$$\tau_u = 2s \tag{B.41}$$

Solving the underlying differential equations leads to the same result (not shown here).

B.5. Estimation of the dissociation constant for a second ATP binding

The K_d of the first ATP bound to one monomer of Hsp90 can be expressed as

$$K_{d1} = \frac{c_n \, c_{ATP}}{c_{m1} + c_{m2} + c_2} \tag{B.42}$$

c_{m2} is the concentration of Hsp90 having ATP bound to monomer 2, and c_n is the concentration of Hsp90 having no ATP bound at all. c_{m1} is the concentration of Hsp90 with ATP bound to monomer 1, c_2 is the concentration of Hsp90 with two ATPs bound, and c_{ATP} is the concentration of free ATP, which is equal to the initial ATP concentration because its concentration is much higher than that for Hsp90. We showed that the concentration of two ATPs bound at the same time is very small compared to the other concentration, therefore K_d becomes

$$K_{d1} = \frac{c_n \, c_{ATP}}{c_{m1} + c_{m2} + c_2} = \frac{p_n \, c_{ATP}}{p_{m1} + p_{m2}} \tag{B.43}$$

The probability of finding Hsp90 with one ATP bound is 25%, and thus the probability of finding Hsp90 without ATP is 50% at an ATP concentration of 200 nM. The K_{d1} is therefore 0.2 µM, as also obtained from the rates and detailed in the main text. The K_{d2} of the binding of a second ATP can be expressed as

$$K_{d2} = \frac{(c_{m1} + c_{m2}) \; c_{ATP}}{c_2} = \frac{(p_{m1} + p_{m2}) \; c_{ATP}}{p_2} \tag{B.44}$$

The probability of finding Hsp90 with one ATP bound p_{m1} is again 25%. The probability of finding a twofold bound Hsp90 p_2 is less than 1%; therefore, K_{d2}= 10 µM. It has to be mentioned that this is an estimate for a lower limit; very likely

the real K_{d2} is much higher (because the amount of Hsp90 with two ATPs bound is overestimated from the data in the main text).

B.6. Correction of the bias caused by different measurement time resolutions

A FRET event (e.g., a dwell time of a specific state) can only be observed when the dwell time is longer than the inverse sampling rate and shorter than the length of the fluorescence trace before one dye bleaches. Thus, the measured traces at different time resolutions have different weighting of the data. In order to overcome this bias, the measured FRET distributions have to be correctly weighted as follows. The probability of observing an event with the dwell time T is given by

$$p_m(T) = p_o(T)p(T^C)p(T, T^C) \tag{B.45}$$

where $p_m(T)$ is the probability that the dwell time with the length T can be measured (e.g., observed), $p_o(T)$ is the probability that the dwell time T_E occurs (independent if it is observed or not), $p(T)$ is the probability that the curve has at least the length of the dwell time, and $p(T, T^C)$ is the probability that the event with the time T can be fully observed within the curves, having at least the length of the dwell time (i.e., that the transitions into a certain state and out of this state both lie within the measured fluorescence trace). Thus, the probability of the real occurrence of the dwell time T_E can be easily estimated by:

$$p_o(T) = \frac{p_m(T)}{p(T^C)p(T, T^C)} \tag{B.46}$$

The probability distribution $p(T^C)$ can be obtained from a histogram of the length of all curves used for the analysis as follows. Let $p_i(T_i + \Delta T)$ be the probability of finding a curve with the length T (it is quite useful to set ΔT to the binning time of the measurement), which is represented in an ordinary histogram of the length of

all traces T^C ; then, $p(T^C)$ is given as

$$p(T^C) = \sum_{T_i=T^C}^{0} p_i(T_i + \Delta T) \tag{B.47}$$

Thus, $p(T^C)$ is approaching one for short T^C as expected. Note that usually extremely short traces are not used for analysis; thus $p(T^C)$ will reach 1 before T^C is zero. The probability $p(T, T^C)$ can be obtained as follows. For one trace of length T^C, the probability of fully observing an event with the length T (i.e., the probability $p(T, T^C)$ that both transitions into the certain state and out of the state lie within the interval T^C) is just given by the number of possibilities to place the event with the length T in the curve in a way that both transitions are inside the interval T^C divided by the number of possibilities to have at least one transition of the event inside the interval T^C :

$$p(T, T^C) = \frac{(T^C - T - 2)}{(T^C + T - 2)} \tag{B.48}$$

In order to correct the bias, the probability that the event with the length T can be observed within the measured curves of length T^C or longer has to be calculated. This is just given by the weighted sum of Eq. B.46 from T^C, to infinity:

$$p(T, T^C) = \frac{\sum_{T^C}^{\infty} p_i(T^C + \Delta T)(T^C - T - 2)}{\sum_{T^C}^{\infty} p_i(T^C + \Delta T)(T^C + T - 2)} \tag{B.49}$$

Because the data is automatically binned because of the fixed measuring frequency, we can use a sum (over the bins) instead of the integral (over time). With Eqs. B.49 and B.46 and the histograms of the curve lengths and the dwell times, the corrected dwell times can be calculated. Note that for long dwell times T, which also means long curves T^C, the error of this correction becomes bigger because only few dwell times T and curves T^C exist in that region. This correction has been applied to the standard histograms, and then the values were integrated to obtain the cumulative histograms shown in Fig. 11.4.

B.7. Supplementary figures and tables

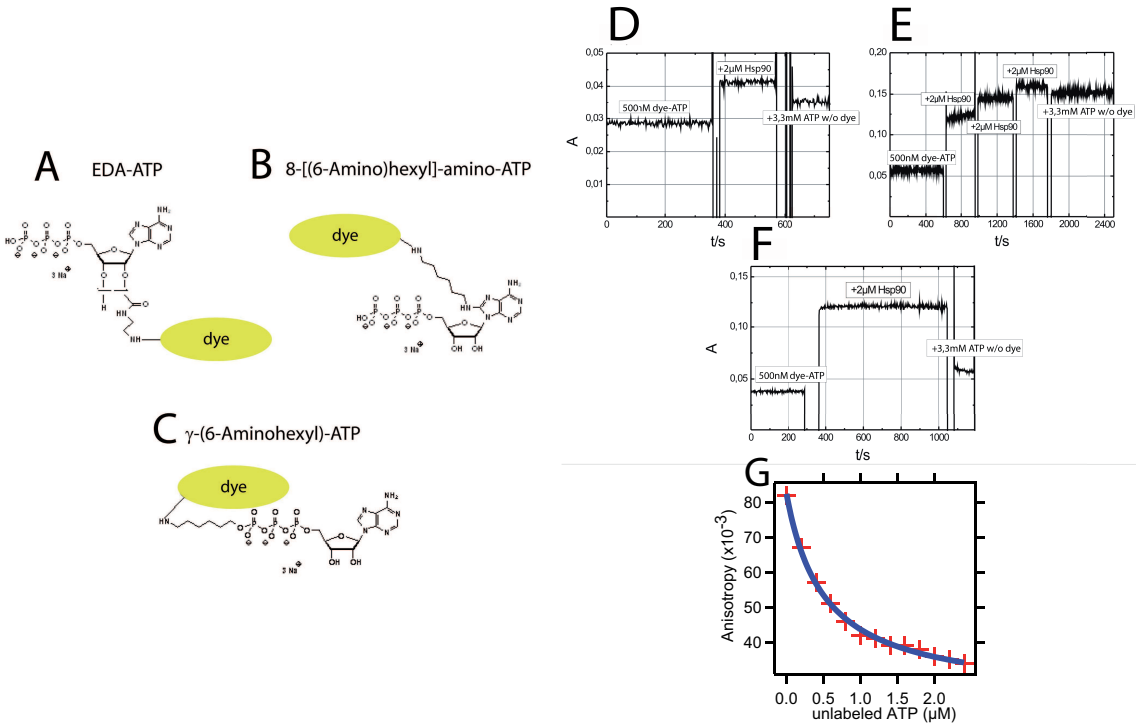

Figure B.1.: Measurement of the binding of labeled ATPs by fluorescence anisotropy. Three different types of labeled ATPs (A–C) have been tested for Hsp90 binding by fluorescence anisotropy (D–F). The fluorescence anisotropy measurements were done with a Jasco Spectrofluorimeter with additional polarization filters as described (sec. 6.5). All measurements were done in 40 mM Hepes, 150 mM KCl, 10 mM MgCl2, pH 7,5 at 30 °C. After measuring the anisotropy of the labeled free ATP, Hsp90 was added. Binding should increase the anisotropy, because the rotational diffusion is slowed down. Finally, an excess of unlabeled ATP should again reduce the anisotropy, because it outcompetes the labeled ATP. This behavior could only be observed for the gamma-labeled ATP (F), which was used for all further studies. (G) To make sure that the labeled ATP binds into the native ATP binding pocket, an outcompete assay has been done. Anisotropy was measured in a solution with 0.5 µM gamma-labeled ATP and 1 µM Hsp90. Upon the addition of native ATP the labeled ATP is outcompeted and the anisotropy drops. Fitting the obtained data (red) with a hyperbolic function (blue) shows that at 0.5 µM native ATP the half maximal anisotropy value is reached, which means that native and labeled ATP bind with the same affinity into the same binding pocket.

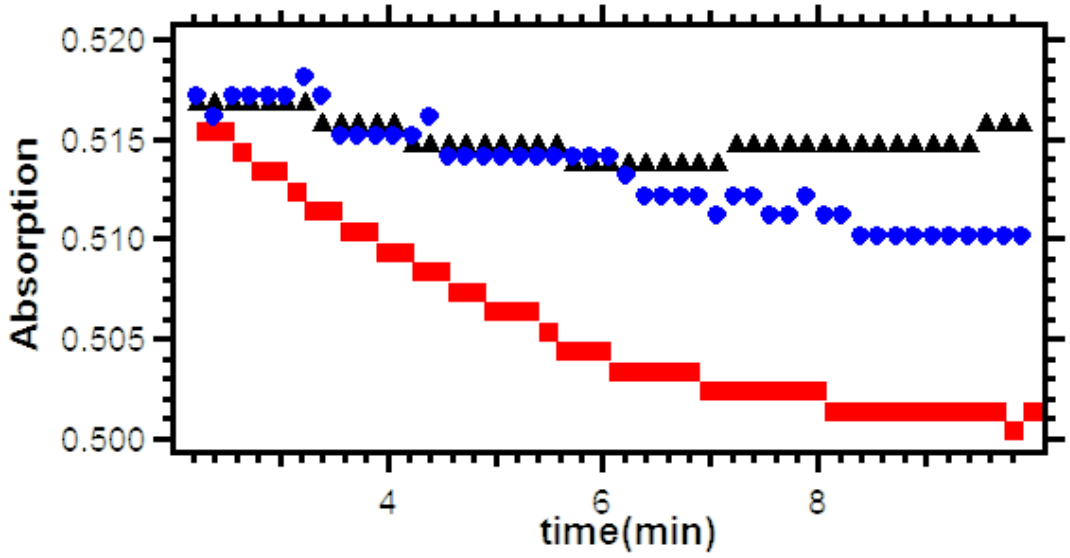

Figure B.2.: ATPase measurements with labeled ATP. The red curve shows the hydrolysis of labeled ATP incubated with wtHsp90. The ATP turnover decreases with time, which is caused by the hydrolysis of ATP and therefore increasing amount of ADP. The blue curve shows the same measurement in the presence of Radicicol (a competitive ATPase inhibitor) as a measure for background activity. As a control, the black curve shows the ATPase measurement with Δ24 Hsp90 (a mutant that cannot hydrolyze ATP). To obtain the ATPase rate for labeled ATP, the red curve was fitted in the range between 0 and 4 min with a linear fit, and the background activity of the blue curve was subtracted. The obtained ATPase rate is around $0.7 min^{-1}$, which is equal to the wild-type ATPase rate, which is between 0.5 and $1 min^{-1}$ [64]. ATPase measurements with the γ-labeled ATP were done as described in sec. 6.1.

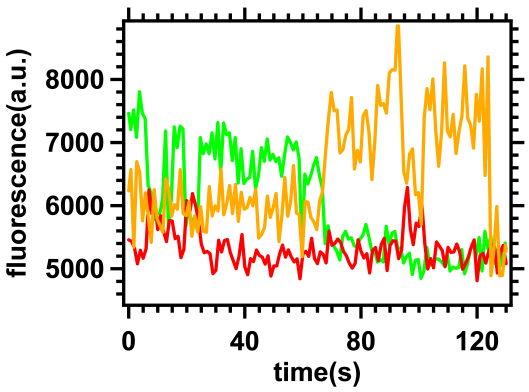

Figure B.3.: N-terminal dynamics during ATP binding. A) Hsp90 starts in the open state (high donor signal, green) without ATP bound. At around 10 and 20 s, two ATP binding events are observed (high acceptor 2, red). Then, at around 65 s, Hsp90 closes (high acceptor 1 signal, orange). Finally, ATP binds to the closed state at around 100 s (high acceptor 2, red). Those transitions are very rarely observed because BSA is added that slows down N-terminal dynamics.

	N-terminally closed		N-terminally open		
Distance	State 1	State 2	State 3a	State 3b	State 4a
D-A1	4.3 nm	4.1 nm	7.2 nm	6.4 nm	6.6 nm
D-A2	—	5.9 nm	—	—	5.3 nm
A1-A2	—	6.0 nm	—	6.3 nm	—

Table B.1.: The inter-dye distances calculated from the single-molecule fluorescence as shown above. A dash indicates either a state where no ATP is bound (state 1, state 3a) or negligible energy transfer.

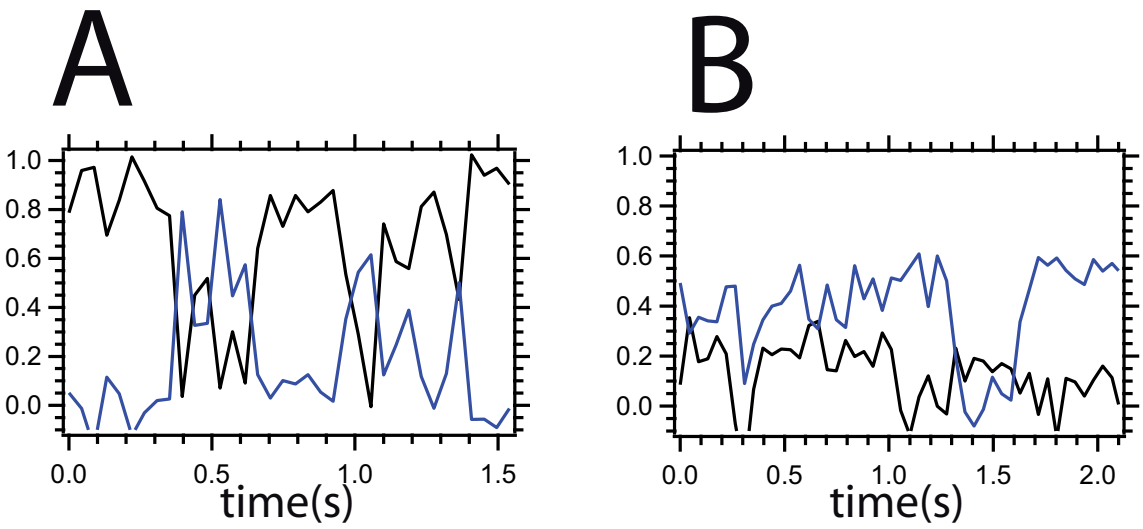

Figure B.4.: Exemplary trace for ADP binding to the open state at around 1.3 s. Measurements were done with a time resolution of 44 ms and an integration time of 40 ms. This is at the limit of our camera; therefore, the signal-to-noise ratio is not as good as for ATP.

τ_{1+} 0.22 s	τ_{2+} ~4 s	τ_{3+} 0.04 s	τ_{4+} ~4 s	τ_{5+} 2 s	τ_{6+} ~4 s	τ_{7+} 11.6 s
τ_{1-} 0.13 s	τ_{2-} ~4 s	τ_{3-} 0.19 s	τ_{4-} ~4 s	τ_{5-} 2 s	τ_{6-} ~4 s	τ_{7-} 3.6 s

Table B.2.: The dwell times for the nucleotide binding and unbinding and N-terminal opening and closing as shown in Fig. 11.7 (main text). The values are for 200 nM ATP and ADP, respectively.

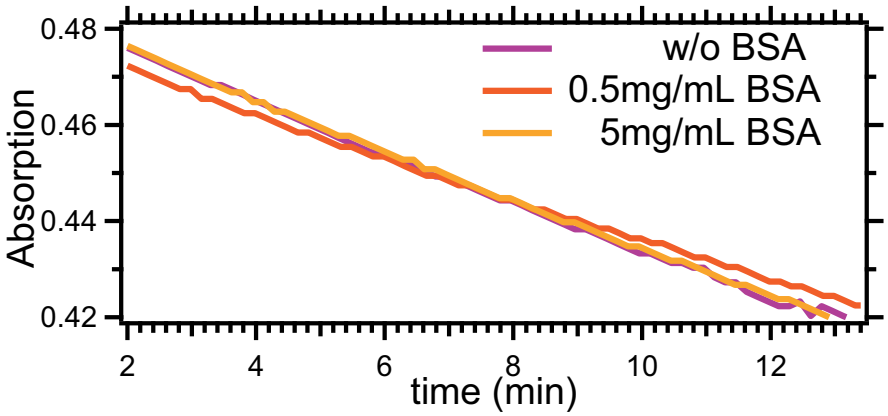

w/o BSA	0.5mg/mL BSA	5mg/mL BSA
0.87 min^{-1}	0.72min^{-1}	0.97min^{-1}

Figure B.5.: ATPase activity in the presence of BSA. We measured the ATP turnover in the presence of 0, 0.5, and 5 mg/mL BSA (Upper). The obtained k_{kat} values (after background correction) are given in the table (Lower)—they are all in the range of literature values. The ATPase assay was done as described above (sec. 6.1). The single-molecule measurements in the main text were done with 0.5 mg/mL BSA.

C. Appendix C: Mechanochemical-cycle of HtpG

C.1. Supplementary figures and tables

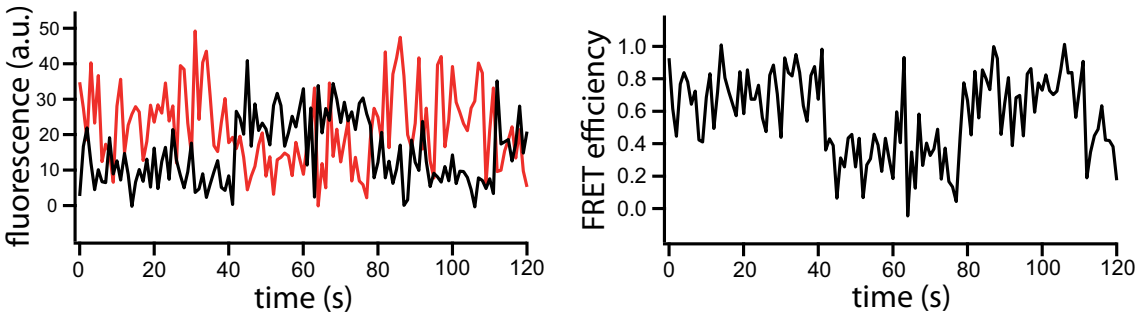

Figure C.1.: Example for a fluorescence (left) and FRET efficiency (right) trace of the 341C mutant in the presence of ATP to demonstrate two of the rare opening events (between 40s and 65s). Most obtained curves do not show such opening events.

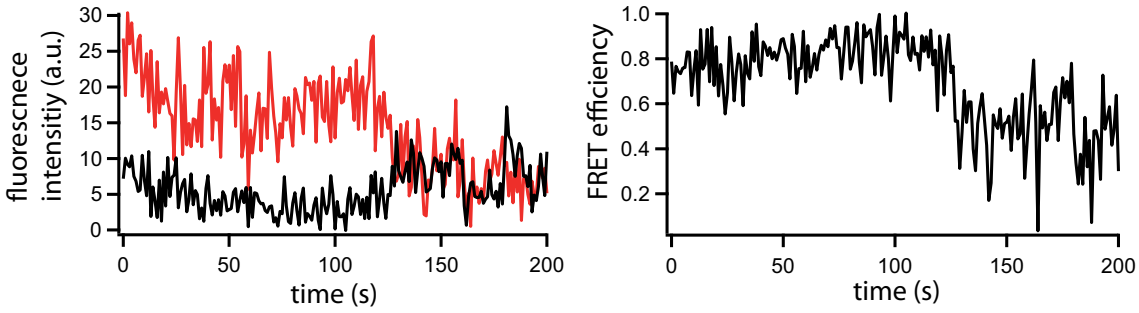

Figure C.2.: Example for a fluorescence (left) and FRET efficiency (right) trace showing the rare occurrence of FRET values around 0.5 (after 125s) for the 61C mutant in the presence of ADP. The decrease of both fluorescence intensities at the beginning of the curve is caused by continuous bleaching of the background. As can be seen this effect does not influence the FRET efficiency.

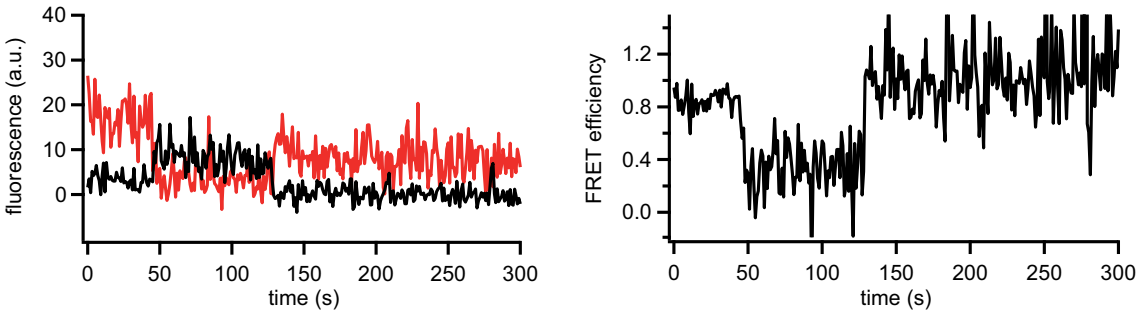

Figure C.3.: Example for a fluorescence (left) and FRET efficiency (right) trace for the 61C mutant in the presence of ADP. These curves show similar behavior to the curves of the 341C mutants in the presence of ADP (Fig. 12.1C, main text), namely opening and closing on the timescale of tens of seconds in between two defined states.

Mutant	k_{cat}
HtpG 61C C-Zip	0.46 min^{-1}
HtpG 341C C-Zip	0.67 min^{-1}
HtpG 61C 341C C-Zip	0.50 min -1
HtpG 521C	0.72 min^{-1}

Table C.1.: ATPase activity of different mutants at 30°C. All mutants show a k_{cat} of around 0.5 min^{-1}, which is equal to the wild type activity within the error of the measurement.

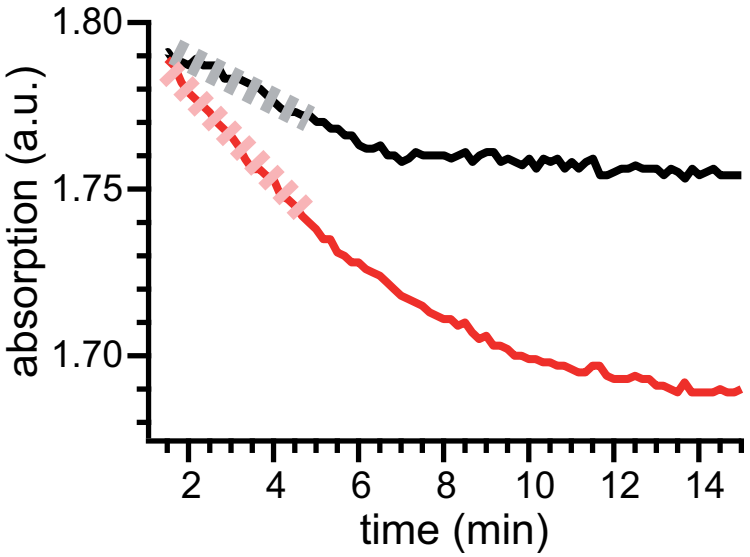

Figure C.4.: Hydrolysis of ATP labeled at the γ-position with Atto 647N via a C6-linker. The red curve shows the hydrolysis of ATP by 2μM HtpG 61C whereas the black curve shows background ATPase after the inhibition of HtpG with radicicol. The initial slopes were fitted, from the difference of the slopes the k_{kat} of the ATPase could be calculated with 0.68 min^{-1} which is equal to the wild type ATPase rate within the error of the measurement.

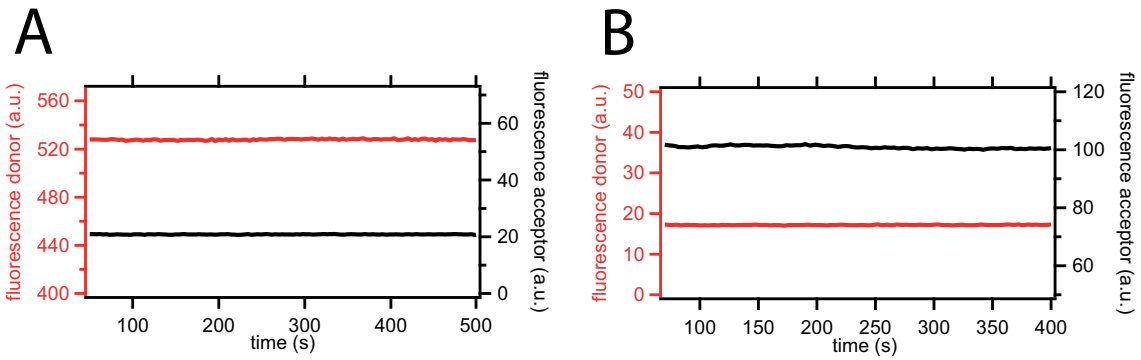

Figure C.5.: (A) 10μM ATP mixed at t=0 with 1μM labeled HtpG (C61, Atto550). (B) 1μM unlabeled HtpG (C61) mixed at t=0 with 10μM labeled ATP (γATP, Atto 647N).

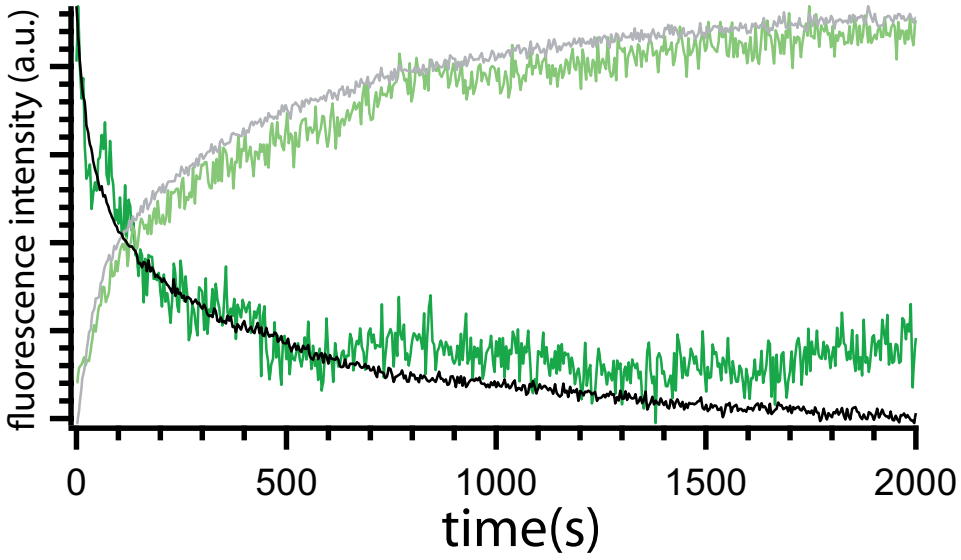

Figure C.6.: Monomer exchange at a concentration of 250 nM for each monomer (black/grey) and 25 nM for each monomer (green). The exchange curves superimpose within the uncertainty of the measurement and therefore show that no significant concentration dependence exists and thus that the reaction is not diffusion limited.

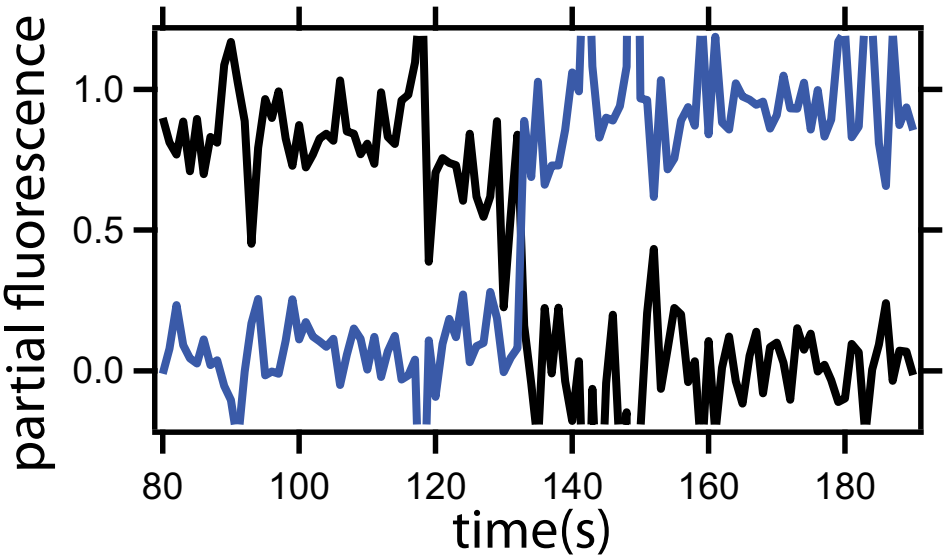

Figure C.7.: Example trace for long time ATP binding. ATP binds at around 135s and stays until bleaching of the dye occurs.

	apo	ATP	ADP	yHsp90 AMPPNP	2IOQ (apo)	2IOP (ADP)	SAX structure at high pH
61-61	4.9 nm	4.3 nm	4.9 nm hf 7.0 nm lf	7.1 nm	10.9 nm	6.3 nm	13.8nm
341-341	5.5 nm	5.6 nm	5.3 nm hf 7.7 nm lf	2.4 nm	6.2 nm	3.7 nm	7.8nm
2xc	4.7 nm	4.9 nm	5.0 nm	3.9 nm	3.3 nm	2.2 nm	3.9 nm
521	5.2 nm	5.2 nm	5.1 nm	4.7 nm	4.8 nm	5.0 nm	4.3 nm

Table C.2.: Calculated distances between dyes at the two N-domains (61-61), M-domains (341-341), within one monomer (2xc) and in the C-domains (521) derived from the FRET histograms (Fig. 12.2, main text) with a Förster radius of 6.5 nm. The distances are given in the apo, ATP and ADP state and for comparison the measured distances from the yHsp90:AMP-PNP crystal structure, as well as the suggested crystal structures for HtpG:ADP (2IOP) and the suggested structure of apo HtpG (2IOQ) are given. Finally, a solution SAXS based modeled structure of HtpG at high pH from the Agard group is given. lf: low FRET peak. hf: high FRET peak.

yHsp90									
τ_{1+}	τ_{2+}	τ_{3+}	τ_{4+}	τ_{5+}	τ_{6+}	τ_{7+}	τ_{8+}	τ_{9+}	τ_{10+}
≈1s	≈2s	≈1s	3.6s	$2.6\text{x}10^{-8}$ Ms	≈3s	$8\text{x}10^{-9}$ Ms	≈3s	2s	≈3s
τ_{1-}	τ_{2-}	τ_{3-}	τ_{4-}	τ_{5-}	τ_{6-}	τ_{7-}	τ_{8-}	τ_{9-}	τ_{10-}
≈2s	≈2s	≈3s	$2.3\text{x}10^{-6}$ Ms	0.22s	≈3s	0.19s	≈3s	$8\text{x}10^{-7}$ Ms	≈3s

HtpG			
τ_{1+}	τ_{2+}	τ_3	τ_{4+}
≥1s	$>10^{-6}$ Ms	100s	>10s
τ_{1-}	τ_{2-}		τ_{4-}
>1s	≥1s		>10s

Table C.3.: Mean dwell times of yHsp90 and HtpG according to Fig. 12.5, main text. They were obtained from the originally double exponential curves by multiplying the values at half maximum with ln2 (to make these times comparable to the times given for HtpG, this also explaines the small differences to Tab. B.2, where the half maximum times are given). The values for HtpG are only estimates for the lower limit, because the kinetic processes are usually too slow to obtain full dwell time distributions. Therefore these values represent the fastest transitions that could be found for a certain process. τ_3 is the mean hydrolysis time (from bulk experiments). Ms is mol per liter times second (second order binding reaction).

mutant/dye	61C Atto550	341C Atto550	521C Atto 550
anisotropy	0,19	0,18	0,17

Table C.4.: Anisotropy values for the utilized dye positions. The anisotropies are all below 0.2 and thus the dyes can be regarded as freely rotating [57]. The anisotropy values were only measured for the Atto 550 dye since free rotation of one dye is sufficient to assume a κ^2 of 2/3 in a FRET assay.

Bibliography

[1] Morano KA, Grant CM, Moye-Rowley WS. The response to heat shock and oxidative stress in Saccharomyces cerevisiae. Genetics; 190(4):1157–95.

[2] Hartl FU, Hayer-Hartl M. Molecular chaperones in the cytosol: from nascent chain to folded protein. Science. 2002; 295(5561):1852–8.

[3] Ali MM, Roe SM, Vaughan CK, Meyer P, Panaretou B, Piper PW, et al. Crystal structure of an Hsp90-nucleotide-p23/Sba1 closed chaperone complex. Nature. 2006; 440(7087):1013–7.

[4] Welch WJ, Feramisco JR. Purification of the major mammalian heat shock proteins. J Biol Chem. 1982; 257(24):14949–59.

[5] Lai BT, Chin NW, Stanek AE, Keh W, Lanks KW. Quantitation and intracellular localization of the 85K heat shock protein by using monoclonal and polyclonal antibodies. Mol Cell Biol. 1984; 4(12):2802–10.

[6] Eletto D, Dersh D, Argon Y. GRP94 in ER quality control and stress responses. Semin Cell Dev Biol; 21(5):479–85.

[7] Kang BH. TRAP1 regulation of mitochondrial life or death decision in cancer cells and mitochondria-targeted TRAP1 inhibitors. BMB Rep; 45(1):1–6.

[8] Maruya M, Sameshima M, Nemoto T, Yahara I. Monomer arrangement in HSP90 dimer as determined by decoration with N and C-terminal region specific antibodies. J Mol Biol. 1999; 285(3):903–7.

[9] Richter K, Muschler P, Hainzl O, Buchner J. Coordinated ATP hydrolysis by the Hsp90 dimer. Journal of Biological Chemistry. 2001; 276(36):33689–33696.

[10] Prodromou C, Roe SM, O'Brien R, Ladbury JE, Piper PW, Pearl LH. Identification and structural characterization of the ATP/ADP-binding site in the Hsp90 molecular chaperone. Cell. 1997; 90(1):65–75.

[11] Scheibel T, Neuhofen S, Weikl T, Mayr C, Reinstein J, Vogel PD, et al. ATP-binding properties of human Hsp90. Journal of Biological Chemistry. 1997; 272(30):18608–18613.

[12] Wegele H, Muschler P, Bunck M, Reinstein J, Buchner J. Dissection of the contribution of individual domains to the ATPase mechanism of Hsp90. Journal of Biological Chemistry. 2003; 278(41):39303–39310.

[13] Weikl T, Muschler P, Richter K, Veit T, Reinstein J, Buchner J. C-terminal regions of Hsp90 are important for trapping the nucleotide during the ATPase cycle. J Mol Biol. 2000; 303(4):583–92.

[14] Prodromou C, Panaretou B, Chohan S, Siligardi G, O'Brien R, Ladbury JE, et al. The ATPase cycle of Hsp90 drives a molecular 'clamp' via transient dimerization of the N-terminal domains. EMBO J. 2000; 19(16):4383–92.

[15] Bracher A, Hartl FU. Hsp90 structure: when two ends meet. Nat Struct Mol Biol. 2006; 13(6):478–80.

[16] Pearl LH, Prodromou C. Structure and mechanism of the Hsp90 molecular chaperone machinery. Annu Rev Biochem. 2006; 75:271–94.

[17] Chadli A, Bouhouche I, Sullivan W, Stensgard B, McMahon N, Catelli MG, et al. Dimerization and N-terminal domain proximity underlie the function of the molecular chaperone heat shock protein 90. Proc Natl Acad Sci U S A. 2000; 97(23):12524–9.

[18] Panaretou B, Prodromou C, Roe SM, O'Brien R, Ladbury JE, Piper PW, et al. ATP binding and hydrolysis are essential to the function of the Hsp90 molecular chaperone in vivo. EMBO J. 1998; 17(16):4829–36.

[19] Obermann WM, Sondermann H, Russo AA, Pavletich NP, Hartl FU. In vivo function of Hsp90 is dependent on ATP binding and ATP hydrolysis. J Cell Biol. 1998; 143(4):901–10.

[20] Nathan DF, Lindquist S. Mutational analysis of Hsp90 function: interactions with a steroid receptor and a protein kinase. Mol Cell Biol. 1995; 15(7):3917–25.

[21] Weikl T, Muschler P, Richter K, Veit T, Reinstein J, Buchner J. C-terminal regions of Hsp90 are important for trapping the nucleotide during the ATPase cycle. Journal of Molecular Biology. 2000; 303(4):583–592.

[22] Wigley DB, Davies GJ, Dodson EJ, Maxwell A, Dodson G. Crystal structure of an N-terminal fragment of the DNA gyrase B protein. Nature. 1991; 351(6328):624–9.

[23] Bilwes AM, Alex LA, Crane BR, Simon MI. Structure of CheA, a signal-transducing histidine kinase. Cell. 1999; 96(1):131–41.

[24] Ban C, Yang W. Crystal structure and ATPase activity of MutL: implications for DNA repair and mutagenesis. Cell. 1998; 95(4):541–52.

[25] Neckers L, Workman P. Hsp90 Molecular Chaperone Inhibitors: Are We There Yet? Clinical Cancer Research; 18(1):64–76.

[26] Shiau AK, Harris SF, Southworth DR, Agard DA. Structural analysis of E-coli hsp90 reveals dramatic nucleotide-dependent conformational rearrangements. Cell. 2006; 127(2):329–340.

[27] Prodromou C, Panaretou B, Chohan S, Siligardi G, O'Brien R, Ladbury JE, et al. The ATPase cycle of Hsp90 drives a molecular 'clamp' via transient dimerization of the N-terminal domains. EMBO J. 2000; 19(16):4383–92.

[28] Hessling M, Richter K, Buchner J. Dissection of the ATP-induced conformational cycle of the molecular chaperone Hsp90. Nature Structural & Molecular Biology. 2009; 16(3):287–293.

[29] Richter K, Moser S, Hagn F, Friedrich R, Hainzl O, Heller M, et al. Intrinsic inhibition of the Hsp90 ATPase activity. J Biol Chem. 2006; 281(16):11301–11.

[30] Xu W, Mollapour M, Prodromou C, Wang S, Scroggins BT, Palchick Z, et al. Dynamic Tyrosine Phosphorylation Modulates Cycling of the HSP90-P50(CDC37)-AHA1 Chaperone Machine. Mol Cell; 47(3):434–43.

[31] Soroka J, Wandinger SK, Mausbacher N, Schreiber T, Richter K, Daub H, et al. Conformational switching of the molecular chaperone Hsp90 via regulated phosphorylation. Mol Cell; 45(4):517–28.

[32] Quanz M, Herbette A, Sayarath M, de Koning L, Dubois T, Sun JS, et al. Heat shock protein 90alpha (Hsp90alpha) is phosphorylated in response to DNA damage and accumulates in repair foci. J Biol Chem; 287(12):8803–15.

[33] Scroggins BT, Robzyk K, Wang D, Marcu MG, Tsutsumi S, Beebe K, et al. An acetylation site in the middle domain of Hsp90 regulates chaperone function. Mol Cell. 2007; 25(1):151–9.

[34] Martinez-Ruiz A, Villanueva L, Gonzalez de Orduna C, Lopez-Ferrer D, Higueras MA, Tarin C, et al. S-nitrosylation of Hsp90 promotes the inhibition of its ATPase and endothelial nitric oxide synthase regulatory activities. Proc Natl Acad Sci U S A. 2005; 102(24):8525–30.

[35] Retzlaff M, Stahl M, Eberl HC, Lagleder S, Beck J, Kessler H, et al. Hsp90 is regulated by a switch point in the C-terminal domain. EMBO Rep. 2009;.

[36] Felts SJ, Toft DO. p23, a simple protein with complex activities. Cell Stress Chaperones. 2003; 8(2):108–13.

[37] Young JC, Hartl FU. Polypeptide release by Hsp90 involves ATP hydrolysis and is enhanced by the co-chaperone p23. EMBO J. 2000; 19(21):5930–40.

[38] Lee CT, Graf C, Mayer FJ, Richter SM, Mayer MP. Dynamics of the regulation of Hsp90 by the co-chaperone Sti1. EMBO J; 31(6):1518–1528.

[39] Richter K, Muschler P, Hainzl O, Reinstein J, Buchner J. Sti1 is a non-competitive inhibitor of the Hsp90 ATPase - Binding prevents the N-terminal dimerization reaction during the ATPase cycle. Journal of Biological Chemistry. 2003; 278(12):10328–10333.

[40] Sun L, Prince T, Manjarrez JR, Scroggins BT, Matts RL. Characterization of the interaction of Aha1 with components of the Hsp90 chaperone machine and client proteins. Biochimica et Biophysica Acta (BBA) - Molecular Cell Research; 1823(6):1092–1101.

[41] Wandinger SK, Richter K, Buchner J. The Hsp90 chaperone machinery. Journal of Biological Chemistry. 2008; 283(27):18473–18477.

[42] Richter K, Buchner J. Hsp90: Chaperoning signal transduction. Journal of Cellular Physiology. 2001; 188(3):281–290.

[43] Trepel J, Mollapour M, Giaccone G, Neckers L. Targeting the dynamic HSP90 complex in cancer. Nat Rev Cancer; 10(8):537–549.

[44] Lu X, Xiao L, Wang L, Ruden DM. Hsp90 inhibitors and drug resistance in cancer: The potential benefits of combination therapies of Hsp90 inhibitors and other anti-cancer drugs. Biochemical Pharmacology; 83(8):995–1004.

[45] Ha T, Enderle T, Ogletree DF, Chemla DS, Selvin PR, Weiss S. Probing the interaction between two single molecules: Fluorescence resonance energy transfer between a single donor and a single acceptor. Proceedings of the National Academy of Sciences of the United States of America. 1996; 93(13):6264–6268.

[46] Atkins P. Atkins' Physical Chemistry. Oxford University Press 2009.

[47] Bornschlogl T, Rief M. Single Molecule Unzipping of Coiled Coils: Sequence Resolved Stability Profiles. Physical Review Letters. 2006; 96(11):118102–4.

[48] Mickler M, Hessling M, Ratzke C, Buchner J, Hugel T. The large conformational changes of Hsp90 are only weakly coupled to ATP hydrolysis. Nat Struct Mol Biol. 2009; 16(3):281–6.

[49] Wayne N, Bolon DN. Dimerization of Hsp90 is required for in vivo function. Design and analysis of monomers and dimers. J Biol Chem. 2007; 282(48):35386–95.

[50] Wayne N, Lai Y, Pullen L, Bolon DN. Modular control of cross-oligomerization: analysis of superstabilized Hsp90 homodimers in vivo. J Biol Chem; 285(1):234–41.

[51] Xie J, Schultz PG. An expanding genetic code. Methods. 2005; 36(3):227–38.

[52] Xie J, Schultz PG. A chemical toolkit for proteins–an expanded genetic code. Nat Rev Mol Cell Biol. 2006; 7(10):775–82.

[53] Young TS, Ahmad I, Yin JA, Schultz PG. An Enhanced System for Unnatural Amino Acid Mutagenesis in E. coli. Journal of Molecular Biology; 395(2):361–374.

[54] Young TS, Schultz PG. Beyond the canonical 20 amino acids: expanding the genetic lexicon. J Biol Chem; 285(15):11039–44.

[55] Brustad EM, Lemke EA, Schultz PG, Deniz AA. A general and efficient method for the site-specific dual-labeling of proteins for single molecule fluorescence resonance energy transfer. J Am Chem Soc. 2008; 130(52):17664–5.

[56] Milles S, Tyagi S, Banterle N, Koehler C, VanDelinder V, Plass T, et al. Click strategies for single-molecule protein fluorescence. J Am Chem Soc; 134(11):5187–95.

[57] Ha T. Single-molecule fluorescence resonance energy transfer. Methods. 2001; 25(1):78–86.

[58] Foerster T. Zwischenmolekulare Energiewanderung und Fluoreszenz. Annalen der Physik. 1948; Band 2.

[59] Ratzke C, Mickler M, Hellenkamp B, Buchner J, Hugel T. Dynamics of heat shock protein 90 C-terminal dimerization is an important part of its conformational cycle. Proc Natl Acad Sci U S A; 107(37):16101–6.

[60] Cisse I, Okumus B, Joo C, Ha T. Fueling protein DNA interactions inside porous nanocontainers. Proc Natl Acad Sci U S A. 2007; 104(31):12646–50.

[61] Rhoades E, Cohen M, Schuler B, Haran G. Two-state folding observed in individual protein molecules. J Am Chem Soc. 2004; 126(45):14686–7.

[62] Richter K, Buchner J. Hsp90: Twist and fold. Cell. 2006; 127(2):251–253.

[63] Graf C, Stankiewicz M, Nikolay R, Mayer MP. Insights into the conformational dynamics of the E3 ubiquitin ligase CHIP in complex with chaperones and E2 enzymes. Biochemistry; 49(10):2121–9.

[64] Richter K, Reinstein J, Buchner J. N-terminal residues regulate the catalytic efficiency of the Hsp90 ATPase cycle. Journal of Biological Chemistry. 2002; 277(47):44905–44910.

[65] Morra G, Verkhivker G, Colombo G. Modeling signal propagation mechanisms and ligand-based conformational dynamics of the Hsp90 molecular chaperone full-length dimer. PLoS Comput Biol. 2009; 5(3):e1000323.

[66] Owen BA, Sullivan WP, Felts SJ, Toft DO. Regulation of heat shock protein 90 ATPase activity by sequences in the carboxyl terminus. J Biol Chem. 2002; 277(9):7086–91.

[67] Phillips JJ, Yao ZP, Zhang W, McLaughlin S, Laue ED, Robinson CV, et al. Conformational dynamics of the molecular chaperone Hsp90 in complexes with a co-chaperone and anticancer drugs. J Mol Biol. 2007; 372(5):1189–203.

[68] Tsutsumi S, Mollapour M, Graf C, Lee CT, Scroggins BT, Xu W, et al. Hsp90 charged-linker truncation reverses the functional consequences of weakened hydrophobic contacts in the N domain. Nat Struct Mol Biol. 2009;.

[69] Hainzl O, Lapina MC, Buchner J, Richter K. The charged linker region is an important regulator of Hsp90 function. J Biol Chem. 2009; 284(34):22559–67.

[70] Ratzke C, Berkemeier F, Hugel T. Heat shock protein 90's mechanochemical cycle is dominated by thermal fluctuations. Proc Natl Acad Sci U S A; 109(1):161–6.

[71] Kapanidis AN, Lee NK, Laurence TA, Doose S, Margeat E, Weiss S. Fluorescence-aided molecule sorting: analysis of structure and interactions by alternating-laser excitation of single molecules. Proc Natl Acad Sci U S A. 2004; 101(24):8936–41.

[72] Lee NK, Kapanidis AN, Wang Y, Michalet X, Mukhopadhyay J, Ebright RH, et al. Accurate FRET measurements within single diffusing biomolecules using alternating-laser excitation. Biophys J. 2005; 88(4):2939–53.

[73] McKinney SA, Joo C, Ha T. Analysis of single-molecule FRET trajectories using hidden Markov modeling. Biophys J. 2006; 91(5):1941–51.

[74] Gebhardt JC, Clemen AE, Jaud J, Rief M. Myosin-V is a mechanical ratchet. Proc Natl Acad Sci U S A. 2006; 103(23):8680–5.

[75] Bron P, Giudice E, Rolland JP, Buey RM, Barbier P, Diaz JF, et al. Apo-Hsp90 coexists in two open conformational states in solution. Biol Cell. 2008; 100(7):413–25.

[76] Southworth DR, Agard DA. Client-loading conformation of the Hsp90 molecular chaperone revealed in the cryo-EM structure of the human Hsp90:Hop complex.

[77] Li J, Richter K, Buchner J. Mixed Hsp90-cochaperone complexes are important for the progression of the reaction cycle. Nat Struct Mol Biol; 18(1):61–6.

[78] Pullen L, Bolon DN. Enforced N-domain proximity stimulates HSP90 ATPase activity and is compatible with function in vivo. J Biol Chem. 2011;.

[79] Walerych D, Gutkowska M, Klejman MP, Wawrzynow B, Tracz Z, Wiech M, et al.. ATP binding to Hsp90 is sufficient for effective chaperoning of p53 protein.

[80] Ratzke C, Nguyen MN, Mayer MP, Hugel T. From a Ratchet Mechanism to Random Fluctuations Evolution of Hsp90's Mechanochemical Cycle. J Mol Biol; 423(3):462–71.

[81] Chen B, Zhong DB, Monteiro A. Comparative genomics and evolution of the HSP90 family of genes across all kingdoms of organisms. Bmc Genomics. 2006; 7:19.

[82] Graf C, Stankiewicz M, Kramer G, Mayer MP. Spatially and kinetically resolved changes in the conformational dynamics of the Hsp90 chaperone machine. EMBO J. 2009; 28(5):602–13.

[83] Lakowicz JR. Principles of Fluorescence Spectroscopy. Springer 2006.

[84] Krukenberg KA, Forster F, Rice LM, Sali A, Agard DA. Multiple conformations of E. coli Hsp90 in solution: insights into the conformational dynamics of Hsp90. Structure. 2008; 16(5):755–65.

[85] Mewes HW, Albermann K, Bahr M, Frishman D, Gleissner A, Hani J, et al. Overview of the yeast genome. Nature. 1997; 387(6632 Suppl):7–65.

[86] Street TO, Lavery LA, Agard DA. Substrate binding drives large-scale conformational changes in the Hsp90 molecular chaperone. Mol Cell; 42(1):96–105.

[87] Blattner FR, Plunkett r G, Bloch CA, Perna NT, Burland V, Riley M, et al. The complete genome sequence of Escherichia coli K-12. Science. 1997; 277(5331):1453–62.

[88] Netzer WJ, Hartl FU. Recombination of protein domains facilitated by co-translational folding in eukaryotes. Nature. 1997; 388(6640):343–9.

[89] Lotz GP, Lin H, Harst A, Obermann WM. Aha1 binds to the middle domain of Hsp90, contributes to client protein activation, and stimulates the ATPase activity of the molecular chaperone. J Biol Chem. 2003; 278(19):17228–35.

[90] Richter K, Walter S, Buchner J. The Co-chaperone Sba1 connects the ATPase reaction of Hsp90 to the progression of the chaperone cycle. Journal of Molecular Biology. 2004; 342(5):1403–1413.

[91] Ratzke C, Berkemeier F, Hugel T. Heat shock protein 90's mechanochemical cycle is dominated by thermal fluctuations. Proc Natl Acad Sci U S A; 109(1):161–6.

[92] Dix JA, Verkman AS. Crowding effects on diffusion in solutions and cells. Annu Rev Biophys. 2008; 37:247–63.

[93] Ellis RJ. Macromolecular crowding: obvious but underappreciated. Trends in Biochemical Sciences. 2001; 26(10):597 – 604.

[94] Hessling M. Mechanism of the Molecular Chaperone Hsp90. Doctoral Thesis. 2009;.

[95] Schulte TW, Akinaga S, Soga S, Sullivan W, Stensgard B, Toft D, et al.. Antibiotic radicicol binds to the N-terminal domain of Hsp90 and shares important biologic activities with geldanamycin 1998.

[96] Ali JA, Jackson AP, Howells AJ, Maxwell A. The 43-kilodalton N-terminal fragment of the DNA gyrase B protein hydrolyzes ATP and binds coumarin drugs 1993.

[97] Richter K, Moser S, Hagn F, Friedrich R, Hainzl O, Heller M, et al. Intrinsic inhibition of the Hsp90 ATPase activity. Journal of Biological Chemistry. 2006; 281(16):11301–11311.

[98] Lee J, Lee S, Ragunathan K, Joo C, Ha T, Hohng S. Single-molecule four-color FRET. Angew Chem Int Ed Engl. 2010; 49(51):9922–5.

[99] Lee NK, Kapanidis AN, Koh HR, Korlann Y, Ho SO, Kim Y, et al. Three-color alternating-laser excitation of single molecules: monitoring multiple interactions and distances. Biophys J. 2007; 92(1):303–12.

Declaration

Hiermit erkläre ich, Christoph Ratzke, dass ich die vorliegende Arbeit selbständig verfasst und keine anderen als die angegebenen Quellen und Hilfsmittel verwendet habe. Die Arbeit wurde bisher keiner Prüfungskommission vorgelegt. Teile dieser Arbeit wurden in wissenschaftlichen Journalen veröffentlicht.

.....

Christoph Ratzke

Garching, den .....